

NANOPETROPHYSICS CHARACTERIZATION OF THE MANCOS SHALE FORMATION
IN THE SAN JUAN BASIN OF NORTHWESTERN NEW MEXICO, U.S.A.

by:

Richard Kalteyer

Presented to the Faculty of the Graduate School of
The University of Texas at Arlington in Partial Fulfillment
of the Requirements
for the Degree of
MASTER OF SCIENCE IN GEOLOGY
THE UNIVERSITY OF TEXAS AT ARLINGTON

December 2017

Copyright © by Richard Kalteyer 2017

All Rights Reserved



Acknowledgements

First and foremost, I would like to thank my supervisor, Qinhong Hu. His guidance and help along the way have allowed me to reach my full potential as a graduate student. A special thanks also goes out to my committee members, Dr. John Wickham and Bill Moulton. I am grateful for their time, expertise, and support throughout the process. I would also like to thank the graduate and PhD students participating in Dr. Hu's research group at the University of Texas at Arlington for their assistance in the lab.

I would also like to thank the New Mexico Bureau of Geology (NMBGR) in Socorro, NM for giving me the opportunity to conduct my research. The geologic data and core samples they provided is greatly appreciated. A special thanks also goes to Annabelle Lopez at the NMBGR. Without her help, none of this would have been possible.

Finally, I would like to thank my friends and family for their unwavering support over the past several years. It is impossible for me to describe how much your patience and words of encouragement have meant to me.

November 16, 2017

Abstract

Nanopetrophysics Characterization of the Mancos Shale Formation in the San Juan Basin of Northwestern New Mexico

Richard Kalteyer, MS

The University of Texas at Arlington, 2017

Supervising Professor: Qinhong Hu:

The Mancos Shale of the San Juan Basin is no stranger to the drilling of oil and gas, but traditional exploration within the region has predominately been limited to the use of conventional vertical wells. Due to the recent advances in drilling and completion technologies, a large focus of oil and gas exploration has shifted towards the development of unconventional reservoirs. Because of these significant breakthroughs, it comes as no surprise that an increased interest in further developing the Mancos Shale has taken place. However, like most unconventional plays, low porosity and extremely low permeability characterize the Mancos Shale. These characteristics typically result in large production declines of oil and natural gas in the first couple years of production, sometimes up to 90% (Hughes, 2014). One of these issues involves the hindrance in diffusive hydrocarbon transport from the rock matrix to the fracture network (Hu and Ewing, 2014). In order to improve the production of hydrocarbons in these tight reservoirs, it is important to first understand the petrophysical properties of the reservoir itself so that an assessment can be made on the quality of the reservoir.

This study will provide a better glimpse on the nano-petrophysical properties of pore structure and fluid-rock interactions that implicate hydrocarbon production in tight reservoirs. A suite of tests are performed on core samples from three wells within the Tocito Marine Bar play

and the Offshore Mancos Shale play in order to address the relationship between pore structure and the flow and migration of hydrocarbons within the rock matrix. Some of the tests include mercury intrusion porosimetry (MICP), low-pressure gas physisorption, wettability/contact angle, and fluid imbibition. Various attributes of the core samples including TOC, XRD and pyrolysis data are also used to supplement test results to further evaluate reservoir quality.

Results obtained from XRD indicate the Tocito Marine Bar samples are siliceous in nature, compared to the more calcareous Offshore Mancos Shale samples. Tocito Marine Bar samples are found at shallower depths, and were therefore found to be less mature than samples from the deeper, Offshore Mancos Shale play. Contact angle measurements demonstrate that all samples are oil-wet, as n-decane spread readily on to the surface. Imbibition tests show good connectivity within the inner pore network with respect to n-decane. Porosity and permeability from various testing methods including MICP, core plugs, and low-pressure gas physisorption show that the Mancos Shale is an organic-rich rock with low porosity and low permeability. The Tocito Marine Bar samples display the largest porosity of tested samples ranging from 1.77 to 7.14%, compared to the 1.15% Offshore Mancos sample. Total porosity is influenced primarily by inter-clay platelet pores, organic matter-hosted pores, intragranular pores, and intergranular pores. Porosity and permeability was found to be consistent with results obtained from previous studies, further validating our testing methods.

Table of Contents

Acknowledgements	ii
Abstract	iii
List of Illustrations	vii
List of Tables	ix
Chapter 1 Introduction	1
Chapter 2 Geologic Background.....	2
2-1 Geologic Setting	2
2-2 Stratigraphy	4
2-3 Oil and Gas Production of the Mancos Shale	11
Chapter 3 Methods	13
3-1 Sample Acquisition and Information.....	13
3-2 Sample Preparation	14
3-3 XRD	19
3-4 Pyrolysis	20
3-5 Wettability/Contact Angle Methods	21
3-6 Imbibition	23
3-7 Low-Pressure Gas Physisorption.....	26
3-8 MICP	28
3-9 Production Data	29
Chapter 4 Results	30
4-1 XRD	30
4-2 Pyrolysis	34
4-3 Core Plug	39
4-4 Wettability/Contact Angle	40
4-5 Imbibition	43
4-6 Low Pressure Gas Physisorption Results	49
4-7 MICP	54
4-8 Production Data	60
Chapter 5 Discussion	61
5-1 Mineralogy.....	61
5-2 Wetting Characteristics and Spontaneous Imbibition	63
5-3 Porosity and Permeability.....	65
5-4 Pore Size Distribution.....	67

Chapter 6 Conclusion and Recommendations	72
6-1 Conclusions	72
6-2 Recommendations	73
Appendix	74
Appendix A	74
Appendix B	77
Appendix C	78
References	97
Biographical Information	104

List of Illustrations

Figure 2-1 Index map identifying structural features of the San Juan Basin. Bisti, Cha Cha, and Armenta oil fields are also highlighted. Arrows indicate dip direction.....	4
Figure 2-2 Stratigraphic cross section of Zuni Basin and San Juan Basin through New Mexico and Colorado.....	6
Figure 2-3 Interpreted stratigraphic column of Mancos/Gallup play displaying the subdivisions of the Mancos Shale. Most production comes from the Mancos C interval, commonly referred to by the industry as the Gallup Sandstone.....	7
Figure 2-4 Ternary plot of lithology from shale plays in the United States.....	9
Figure 2-5 Niobrara outcrop locations in the western U.S.....	10
Figure 2-6 Types of plays identified within the Mancos/Gallup reservoirs in the San Juan Basin. The barrier bar play types display a NW-SE trend. Sample locations are displayed as well.....	11
Figure 3-1 Core samples: whole sample and zoomed face of cubes.....	17
Figure 3-2 Example of core plugs taken parallel and perpendicular to lamination.....	18
Figure 3-3: XRD instrument at Shimadzu Center at the University of Texas at Arlington.....	20
Figure 3-4 Contact angles produced by wetting and non-wetting fluids.....	22
Figure 3-5: Model of apparatus used for imbibition tests.....	25
Figure 3-6: Quantachrome Autosorb iQ3-MP gas sorption instrument used at CUG.....	27
Figure 4-1 XRD results showing numerical weight percentage of individual minerals as well as minerals grouped by “type”.....	31
Figure 4-2 Mineralogy averages from samples located in Tocito Marine Bar Play plotted on Schlumberger’s sCore classification ternary diagram.....	33
Figure 4-3 Mineralogy averages from samples located in Offshore Mancos Play plotted on Schlumberger’s sCore classification ternary diagram. Well “S2” includes SZ5293-U.....	34
Figure 4-4 T_{\max} vs. HI displays kerogen type of Tocito Marine Bar and Offshore Mancos plays.....	38
Figure 4-5 SZ5293-U Contact angle results.....	41
Figure 4-6 OA5137-M Contact angle results.....	42

Figure 4-7 JW4892-L Contact angle results.....	42
Figure 4-8 JW4892-L DI water imbibition results.....	46
Figure 4-9 OA5137-M DI water imbibition results.....	46
Figure 4-10 SZ5293-U DI water imbibition results.....	47
Figure 4-11 JW4892-L n-decane imbibition results.....	47
Figure 4-12 OA5137-M n-decane imbibition results.....	48
Figure 4-13 SZ5293-U n-decane imbibition results.....	48
Figure 4-14 Nitrogen Sorption Isotherm of JW4892-L.....	49
Figure 4-15 Nitrogen Sorption Isotherm of OA5137-M.....	50
Figure 4-16 Nitrogen Sorption Isotherm of SZ5293-U.....	50
Figure 4-17 Graphical representation of pore size distribution obtained from nitrogen physisorption tests using DFT method.....	51
Figure 4-18 Cumulative and incremental pore volume of JW4892-L displayed.....	53
Figure 4-19 Cumulative and incremental pore volume of OA5137-M displayed.....	54
Figure 4-20 Cumulative and incremental pore volume of SZ5293-U displayed.....	54
Figure 4-21 Example of inflection points picked for sample OA5137-M.....	58
Figure 4-22 Pore size distribution obtained from MICP of Tocito samples, JW4892-L and OA5137-M.....	59
Figure 4-23 Intrusion and extrusion curves obtained from MICP tests of Tocito Marine Bar samples.....	60
Figure 5-1 Modified from “Nature and Distribution of Niobrara Lithologies in the Cretaceous Western Interior Seaway (Longman, Luneau, Landon 1998).....	63
Figure 5-2 Relationship between porosity and TOC in samples.....	70
Figure 5-3 Relationship between maturity and depth of samples.....	71
Figure 5-4 Relationship between porosity and depth of samples.....	71

List of Tables

Table 1 Reservoir data from the oil fields of selected core samples.....	2
Table 2 Well name and associated Sample ID of core samples used for study.....	14
Table 3: Table displaying an average of mineralogic data obtained by Mineral Lab. Tocito Marine Bar (yellow) and Offshore Mancos (blue).....	32
Table 4 Pyrolysis data obtained by UTA. Tocito Marine Bar (yellow) and Offshore Mancos (blue).....	35
Table 5 Table displays helium porosity and permeability results of core samples.....	40
Table 6 Contact angle data at 30 seconds for DI Water, API brine, and 20% IPA. At 30 seconds, n-decane contact angles fall below the detection limit of instrument.....	43
Table 7 Connectivity slopes obtained from imbibition tests of DI water and n-decane.....	45
Table 8 Pore size distribution using DFT method.....	51
Table 9 Pore size distribution (%) of pore widths (nm) obtained from nitrogen gas physisorption using BJH method on adsorption and desorption results.....	52
Table 10 Results obtained through MICP of Tocito samples, JW4892-L and OA5137-M.....	56
Table 11 Porosity results obtained from various methods including MICP and helium pycnometry, as well as helium porosity conducted by Guodong et al. (2015).....	57
Table 12 Pore size distribution percentages by pore width ranges.....	59
Table 13 Production data of selected wells (Drilling Info, 2017). Blue is Offshore Mancos Play and Yellow is Tocito Marine Bar Play.....	61
Table 14 Porosity measurement from different methods.....	66
Table 15 Permeability measurements from different methods.....	67

Table 16 Porosity and illite percentage compared to inter-clay platelet pore percentages for both MICP (2.8-5 nm) and nitrogen physisorption DFT method (0.5-5 nm).....	72
--	----

Chapter 1 Introduction

The San Juan Basin of northwestern New Mexico has a long history of oil and gas production, beginning in the early 1920's with its first conventional natural gas well. Production has historically come from conventional sandstones, naturally fractured shales, as well as recently discovered coal bed methane (CBM) reservoirs. In 2010, the region was listed by the U.S. Energy Information Administration to have the 2nd largest proven reserves of natural gas, with over 1.3 trillion cubic feet (TCF) produced in 2009. A recently conducted survey has suggested the basin contains up to 66 TCF natural gas, making it one of the largest natural gas fields in the United States (NGI, 2017). However, recent exploitation of natural gas in the Marcellus Shale has driven down the price of the commodity forcing operators in the San Juan Basin to sell their assets or focus their attention towards the oil-rich Mancos Shale, where prices are more economical. Industry experts have estimated the oil window within the Mancos Shale to contain approximately 60 billion barrels of oil, 10% of which are thought recoverable (Robinson-Avila, 2013).

A significant portion of oil and gas production comes from numerous small oil fields in the northwestern portion of the basin, primarily in Rio Arriba and San Juan counties. Core samples used for purposes of this study were obtained from three of these oil fields. Mancos/Gallup reservoirs are lithologically heterogeneous, but predominantly consist of interbedded sand, silt, and shale. Considered a hybrid shale-oil resource system, the Mancos Shale is composed of organic-rich mudstones with juxtaposed organic-lean facies (Jarvie, 2012). Most Gallup/Mancos production occurs in the northwest-southeast trending Tocito Sandstone Lenticle of the Mancos Shale and has proven to be productive due to well-developed stratigraphic

traps. The play has produced over 920 BCF natural gas and 173 MMBO from over 3,800 wells (Just et al., 2013).

The Bisti field, one of the largest Tocito Gallup fields, has an estimated ultimate recovery of 51,000 MBO. Tocito bar-like bodies are typically 50 feet thick or less (Huffman, 1987) and are encased in the Upper Cretaceous marine Mancos Shale, the primary source rock of the region. Containing roughly 1-3% TOC, the Mancos produces a sweet, low-sulfur, paraffin-base oil (Huffman, 1987) (Table 1). Other production in the basin has been found to come from naturally fractured Mancos reservoirs located along the southeast and northwest flanks of the basin. As is custom with hybrid shales, the source rock itself may contribute to production and can make up a component of oil in place (OIP) (Jarvie, 2012). Once thought as only a source rock and seal for conventional oil and gas reservoirs, the Mancos Shale now has the potential to serve as one of the San Juan Basin's largest unconventional reservoirs.

Table 1 Reservoir data from the oil fields of selected core samples (Sabins, 1983; Matheny and Matheny, 1983; Sperandio, 1983)

Field	Trap	Producing Formation	Porosity	Permeability	Water Saturation	Oil Gravity
Bisti	Stratigraphic	"Gallup"	15	25	25	39°
Cha Cha	Stratigraphic	"Gallup"	13.5	57	25	41°
Armenta	Fractured Resservoir	"Gallup"	1 to 4	≤ 0.4	unknown	40°

Chapter 2 Geologic Background

2-1 Geologic Setting

The San Juan Basin is an asymmetric structural basin that spans approximately 140 miles wide and 200 miles long across most of northwestern New Mexico and southwestern Colorado, encompassing roughly 12,000 square miles (Craig, 1971). The basin is bounded by the

Defiance Uplift to the west, the Four Corners Platform to the northwest, the San Juan Uplift to the north, the Gallina-Archuleta Arch to the northeast, the Nacimiento Uplift to the east, and the Zuni Uplift to the south. The structural boundaries of the San Juan Basin are categorized as various monoclines, domal uplifts, and low platforms. Late Paleozoic tectonism as well as Mesozoic uplift and deformation affected the region, but it was not until the Late Cretaceous and early Tertiary where primary structural components of the San Juan Basin formed (Figure 2-1).

In the Late Cretaceous, the San Juan Basin was located on the western margin of the Western Interior Seaway. During this time, there was an episodic interplay between shallow water sediments to the northeast, and low-relief clastic sediments to the southwest (Molenaar, 1977). Along with the influx of sediment from transgressive and regressive events, an overall rise in sea level and basin subsidence contributed to the deposition of approximately 6,500 feet of sediment. Following the deposition of the Mancos Shale and other Late Cretaceous sediments, Laramide compressional forces influenced the shape of what is now considered the present day San Juan Basin.

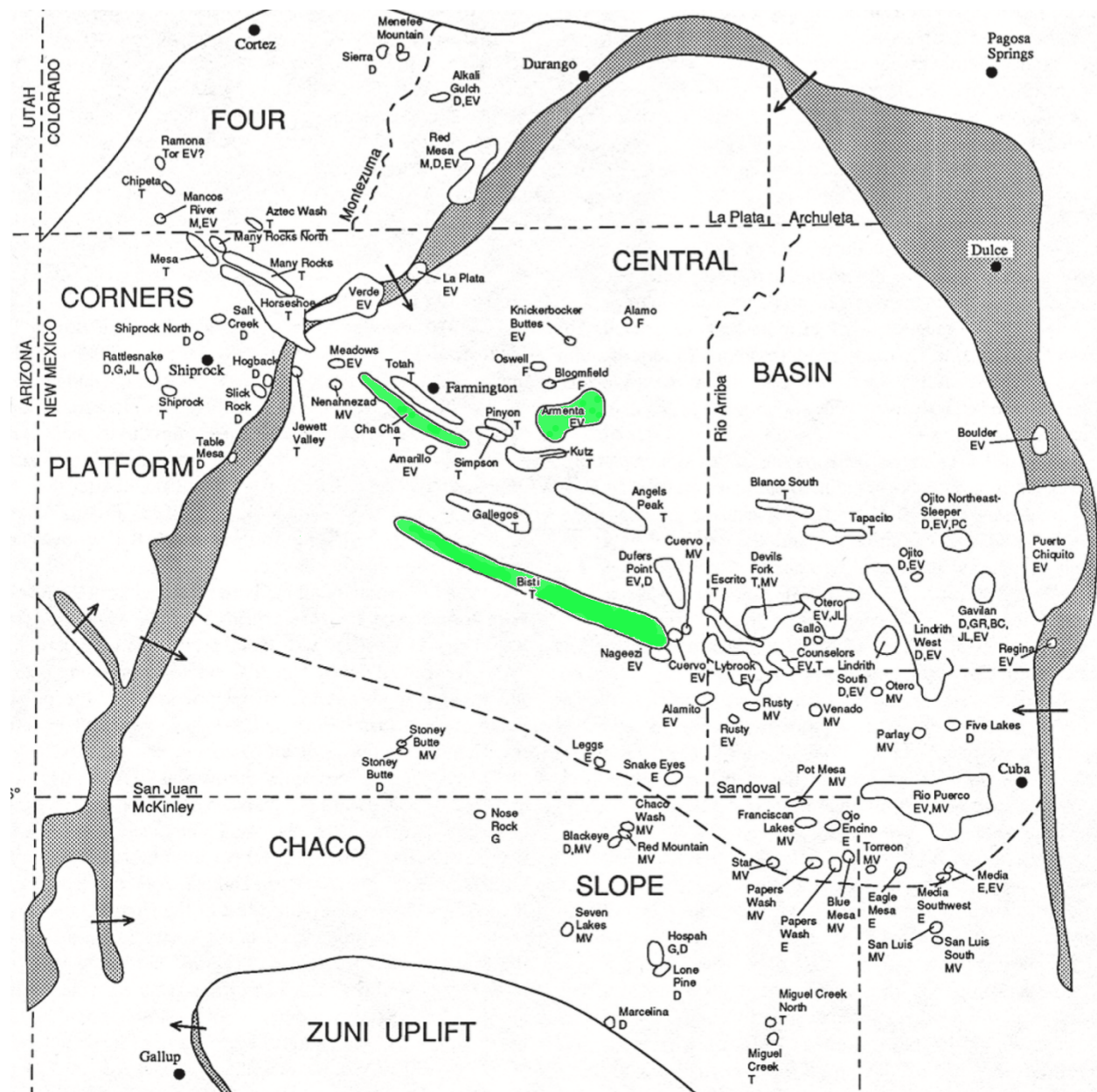


Figure 2-1 Index map identifying structural features of the San Juan Basin. Bisti, Cha Cha, and Armenta oil fields are also highlighted in green. Arrows indicate dip direction (modified from Fassett, 2010).

2-2 Stratigraphy

Although there are many formations in the San Juan Basin, some of which contribute to oil and gas production, the stratigraphic description of the Mancos/Gallup play will be addressed

for purposes of this study. The Mancos Shale is separated into two formations, the Upper Mancos Shale and the Lower Mancos Shale. The Upper Mancos Shale is overlain by the Point Lookout Sandstone and the Lower Mancos Shale rests on top of the transgressive Dakota Sandstone (Figure 2-2). In some regions of the San Juan Basin, the Upper Mancos Shale lies unconformably on top of the Lower Mancos Shale. In other portions of the basin, the Gallup sandstone lies between the Upper and Lower Mancos formations. Both the Upper and Lower Mancos Shale formations have traditionally been recognized as a source rock and seal for most intertonguing sandstone reservoirs throughout the basin.

The Upper Mancos Shale consists of grey to dark-grey, organic rich shale with interbedded siltstones and sandstones. However, discrepancy occurs among stratal units in the lowermost portion of the Upper Mancos Shale. Current completion reports and scout cards coin most Upper Mancos tops as “Gallup” tops. Prior to Dane’s work (Dane, 1960), the unconformity between the Upper and Lower Mancos Shale was not recognized. Subsequently, it was thought that Tocito marine- bar sand bodies in the lowermost part of the Upper Mancos Shale were stratigraphically equivalent to the “true” Gallup sandstone. It wasn’t until Dane’s (1960) work, that the unconformity was recognized, ultimately revealing that the Tocito sands were younger than the true Gallup sands. Because of this inconsistency, most if not all reservoirs are assigned the term “Gallup” (Budd, 1957; Silver, 1957). In reality, these reservoirs should be identified as Upper Mancos (Broadhead, 2015). To further simplify the issue, Broadhead (2015) separated the Upper Mancos Shale into three discrete units: Mancos A, Mancos B, and Mancos C (Figure 2-3).

These units were distinguished by their unique well logging response of gamma ray and resistivity.

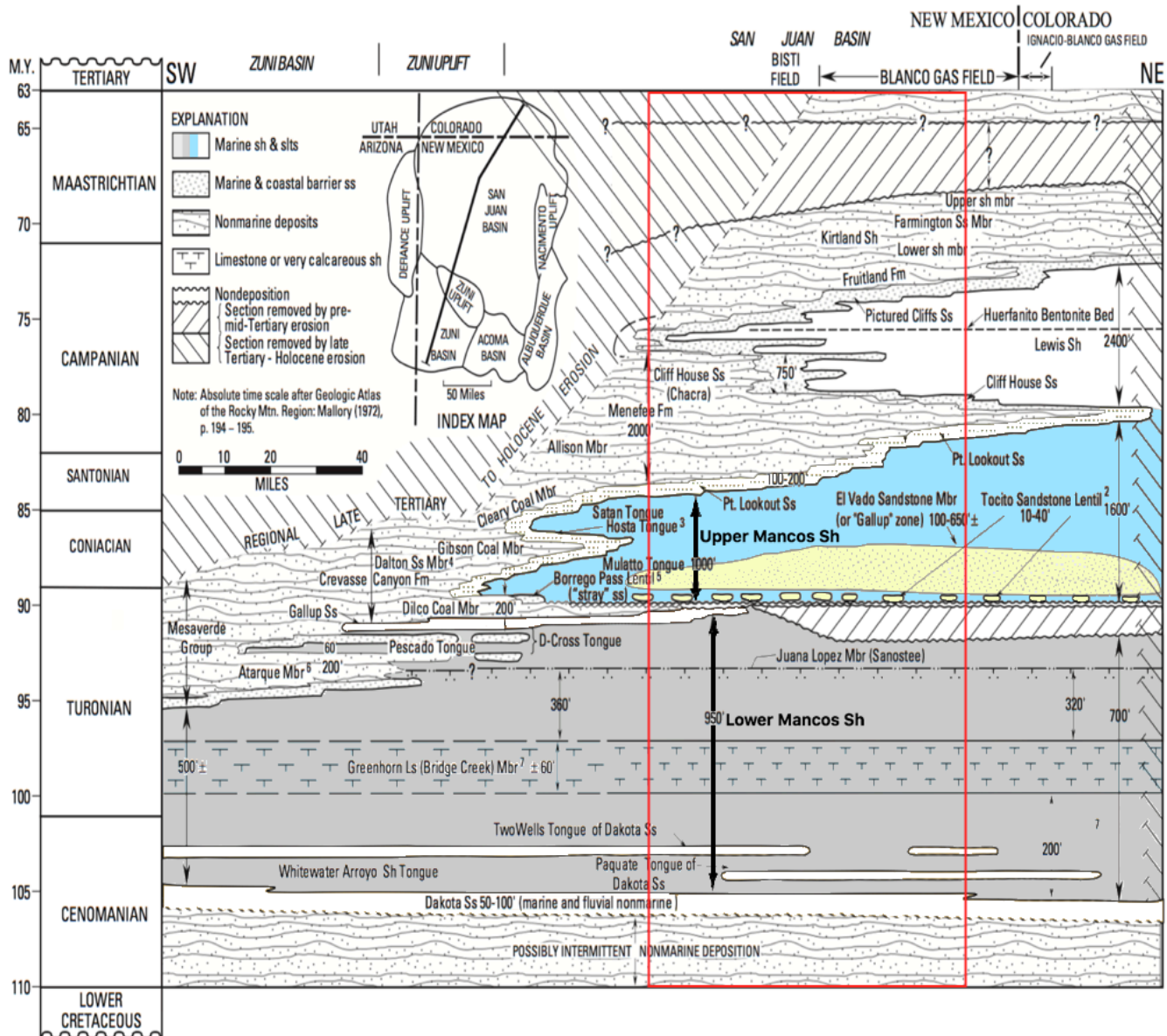


Figure 2-2 Stratigraphical cross section of Zuni Basin and San Juan Basin through New Mexico and Colorado: Upper Mancos Shale (baby blue), Tocito Sandstone Lentil and El Vado Sandstone (yellow), and Lower Mancos Shale (grey). Red box identifies relative location in cross sectional view where our samples were obtained (modified from Ridgley et al., 2013).

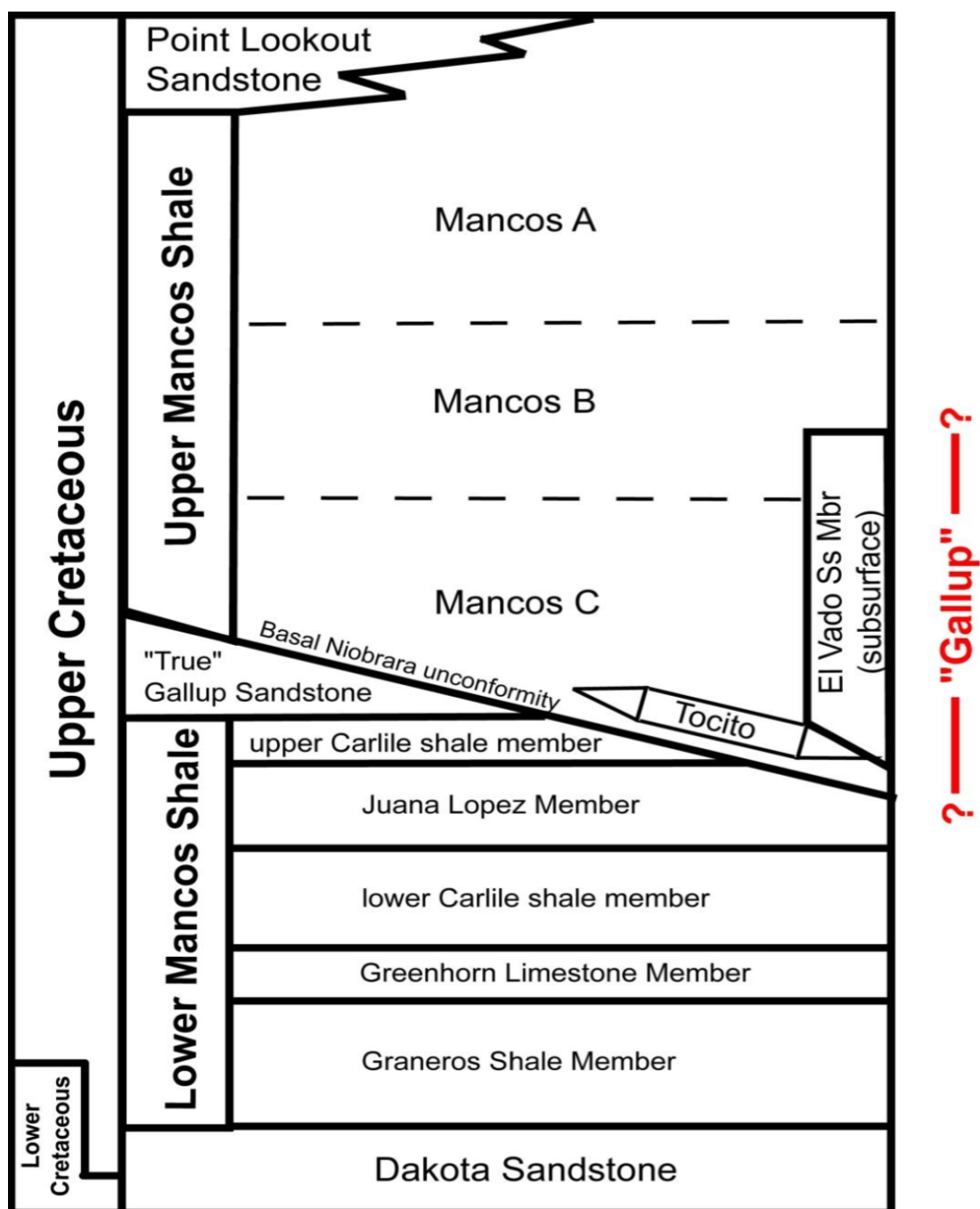


Figure 2-3 Interpreted stratigraphical column of Mancos/Gallup play displaying the subdivisions of the Mancos Shale. Most production comes from the Mancos C interval (lower portion of Upper Mancos Shale), commonly referred to by the industry as the Gallup Sandstone (Broadhead, 2015).

The majority of traditional productive reservoirs in the basin have come from intervals in the controversially identified “Gallup” formation. Within this formation, most production comes from the Tocito Lentil and El Vado Sandstone members. The Tocito Lentil is thought to be located in the lower portion of the Mancos C and contributes to most oil production. The El Vado Sandstone lies just above the lower portion of the Mancos C and consists of interbedded sandstone, siltstone, and organic-rich marine shales. Previous work on the El Vado Sandstone by Fassett and Jentgen (1978) have identified the formation to be most likely located within the lowermost portion of the Mancos B and middle and upper portions of the Mancos C. The Mancos A interval is primarily located on the southern flank of the basin and has reasonable petroleum generation potential. It is safe to say that the Mancos Shale is rather heterogeneous in nature, but as a whole, has been agreed to have less carbonate influence than other shale plays in the United States (Figure 2-4). In effect, hydraulic fracturing techniques may need to be addressed due to an increase in clay content.

The Mancos Shale in the San Juan Basin is time equivalent to the Niobrara Shale, therefore making the two interchangeable. It is important to recognize this phenomenon, since operators in the industry and literature are not always consistent. For the most part, the Niobrara is usually referred to when it spans into Colorado, Wyoming, and Montana (Figure 2-5). Once thought to be a relatively homogeneous chalky limestone throughout most of the Rocky Mountain region, it is now known to vary both laterally and vertically (Longman et al., 1998). To the west, primarily in the San Juan Basin and parts of the Piceance Basin, shales, silts, and sands dilute the carbonate material more common in the eastern portion of the Western Interior Seaway.

The Mancos Shale contains a rich depositional history consisting of numerous transgressive and regressive events. The offshore marine environment in which the Mancos was deposited, has produced a number of parasequences, which include lowstand, transgressive, and highstand systems tracts. These systems tracts are identifiable by their unique log character, and have been known to display certain petrophysical characteristics (Pasley, 1993). Previous studies aimed at identifying systems tracts within depositional sequences have led to a more predictable and systematic approach towards assessing the quality of a reservoir.

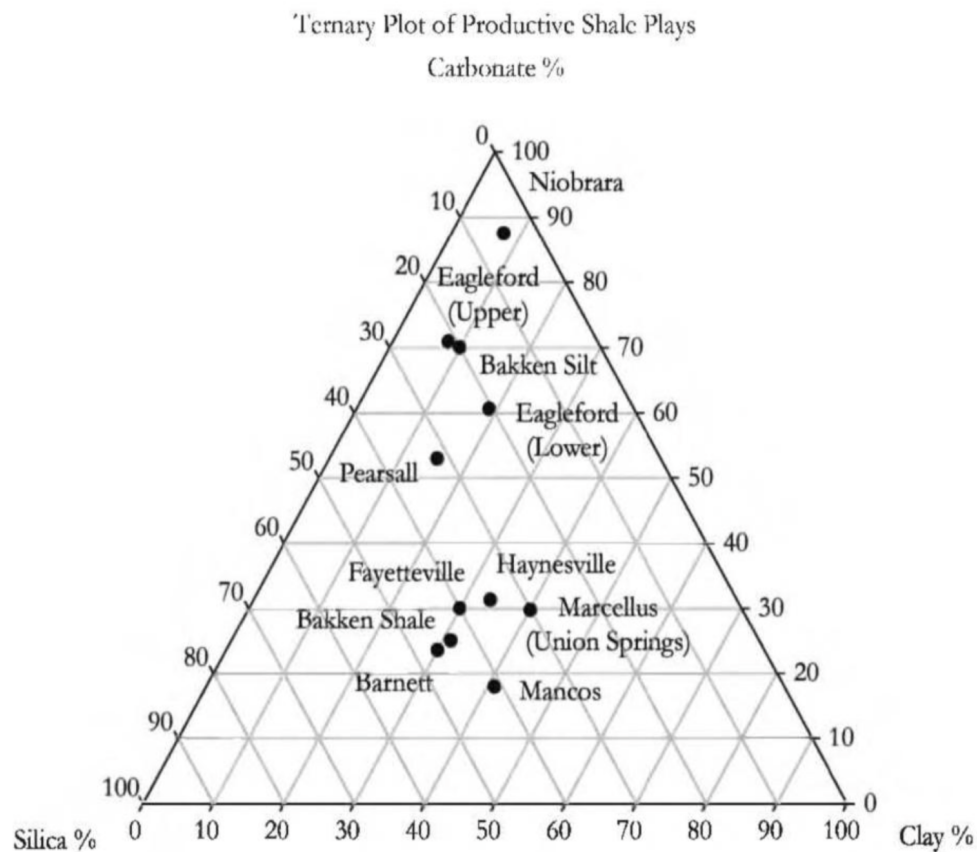


Figure 2-4 Ternary plot of lithology from shale plays in the United States (Horton, 2012).

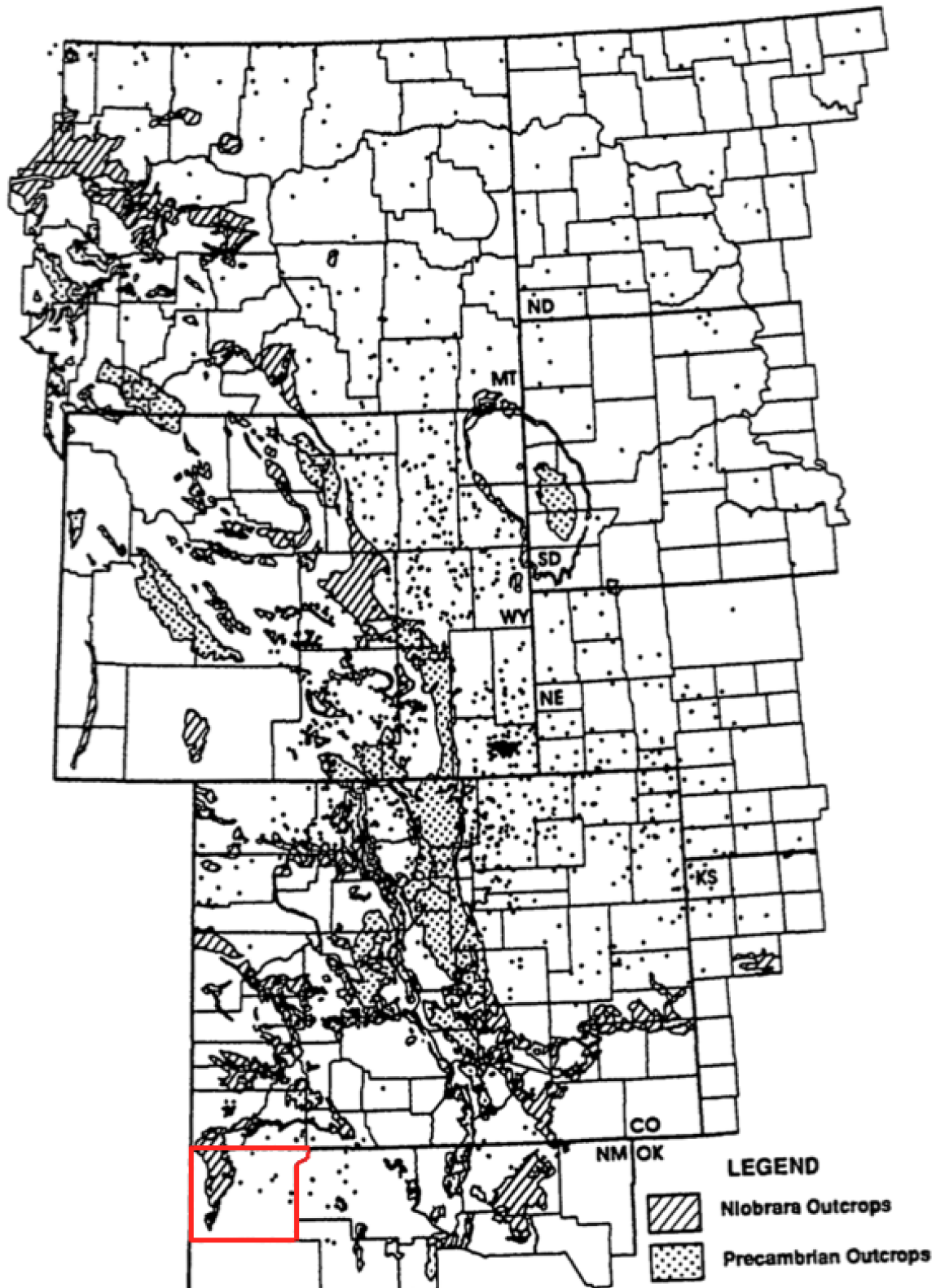


Figure 2-5 Niobrara outcrop locations in the western U.S. (modified from Longman et al., 1998).

2-3 Oil and Gas Production of the Mancos Shale

Within the Mancos Shale, it is largely accepted that three distinct plays comprise most oil and gas production in San Juan Basin. The three plays include the Tocito Marine Bar play, the Offshore Mancos Shale play, and the Naturally Fractured Mancos Shale play (Figure 2-6). For this study, core samples from the Tocito Marine Bar Play and the Offshore Mancos Shale Play were analyzed; as a result, discussions will be limited to these two plays.

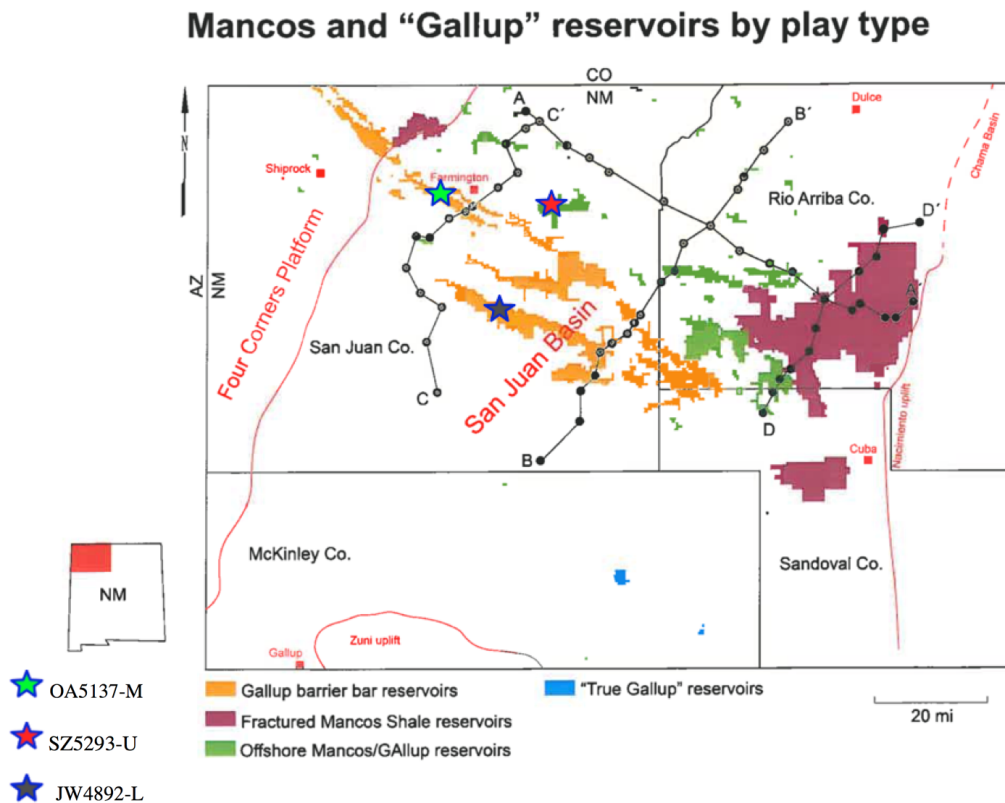


Figure 2-6 Types of plays identified within the Mancos/Gallup reservoirs in the San Juan Basin. The barrier bar play types display a NW-SE trend. Sample locations are displayed as well (Modified from Broadhead, 2013).

The Tocito marine bar play consists of NW-SE oriented lenticular barrier bar sands. The marine bars are thought to have been deposited offshore and parallel to the Cretaceous shoreline,

as displayed in Figure 5 (Broadhead, 2013). Originally thought to be “true” Gallup sands due to an unidentified unconformity, productive intervals in the play are stratigraphically recognized as the Tocito Lentil Sandstone of the Mancos Shale. The encasement of these sand bodies within the lowermost portion of the Upper Mancos Shale provide very well developed stratigraphic traps. They average a thickness of roughly 30 to 50 feet throughout the play and produce conventional oil and associated gas. The Tocito play is predominantly located in San Juan county with minor extensions into Rio Arriba and Sandoval counties. Samples in the Tocito marine bar play used for this study are located in the Bisti and Cha Cha oil fields.

In the southwest landward direction, sandstones contain a restricted marine fauna indicative of marine, lagoonal environments (Sabins, 1972). In the northeast seaward direction, sandstones contain an open marine fauna typical of submerged offshore sand buildups. These Late Cretaceous sand bodies are deposited parallel to each other and overlap in certain localities forming good hydrocarbon reservoirs. The Tocito play is comprised of lowstand, basin floor sandstones, transgressive, ridge sandstones, and incised valley fill sandstones. The lowermost bed facies are bioturbated, muddy, sandy and crossbedded. The uppermost bed facies are poorly sorted, medium grained, crossbedded and ripplebedded (Pasley, 1993).

The Offshore Mancos Shale play lies to the north and northeast of the Tocito marine bar play in the north-central region of the basin and is thought to be its own source and reservoir. Although older and more traditional vertical wells historically occupy the region, recent exploration of oil and gas is heavily focused on the implementation of horizontal drilling and fracturing techniques. Producing intervals in the offshore play consist of shale with interbedded siltstones and sandstones, most likely coming from the El Vado Sandstone of the Mancos Shale. Production is thought to be enhanced by vertical fractures produced by Laramide tilting and

folding. Samples in the Offshore Mancos Shale play used for this study are located in the Armenta oil field.

Chapter 3 Methods

3-1 Sample Acquisition and Information

I contacted the New Mexico Bureau of Geology & Mineral Resources (NMBGR) to request a list of core samples they had at their facility located in Socorro, NM. From the list, I narrowed my selection to Mancos core samples that were available and had various data sets including core reports. Based on the information at hand, I decided on three wells all located in San Juan county of New Mexico. The three wells included Sanchez 2 (API: 3004525620), Joan White 2 (API: 3004505478), and Ojo Amarillo 5 (API: 3004507924). For simplicity, I will refer to the wells based on their sample ID used throughout testing.

I then had NMBGR ship a pallet of the core samples to my house where I viewed boxes from each well to make a selection of samples to use for my study. After observing the boxes of core, I selected one sample from each of the three wells totaling three samples. NMBGR requires one half of a cored interval remain intact, so once samples were selected, whole samples were cut in half and shipped back to NMBGR. In order to keep track of the samples, each sample was assigned a unique Sample ID. Sample ID's were chosen based on an abbreviation of the well name, and the corresponding depth of the acquired sample (Table 2).

Table 2 Well name and associated Sample ID of core samples used for study.

Play	Well Name	Sample ID	Sample Depth (ft.)	Formation	Mass (g)
Bisti	Joan White 2	JW4892-L	4892	Upper Mancos	1,187
Cha Cha	Ojo Amarillo 5	OA5137-M	5137	Upper Mancos	942
Armenta	Sanchez 2	SZ5293-U	5293	Upper Mancos	381

Using type logs as well as correlated logs from previous work, I have determined that core samples retrieved from NMBGR are within the lowermost portion of the Upper Mancos Shale, although scout cards and well reports indicate otherwise (Molenaar, 1974). Broadhead (2013) recognizes this portion of the Mancos Shale as the Mancos C. SZ5293-U samples are in the uppermost portion of the Mancos C interval, OA5137-M samples are in the middle to lower-middle portion of the Mancos C interval, and JW4892-L samples are in the lower portion of the Mancos C interval. Since the lowermost portion of the Upper Mancos Shale is known to produce the most oil and gas, a deeper understanding of pore structure and fluid flow characteristics is needed to recover hydrocarbons at an economic rate.

3-2 Sample Preparation

Once samples were assigned a unique Sample ID, pictures were taken using a digital camera for whole sample pictures as well as a microscopic camera for magnified pictures (Figure 3-1). Core was then then carefully cut into 1 cm³ samples (1.0 cm × 1.0 cm × 1.0 cm) for testing. Epoxy was then applied to four continuous faces of each cube, parallel to lamination, so that two of the faces remained free and untouched. Leftover core samples were also cut into thin slabs (2 mm × 10 mm × 10 mm) for contact angle measurements. Core plugs were obtained from JW4892-L and OA5137-M in both parallel and transverse direction to lamination (Figure 3-2).

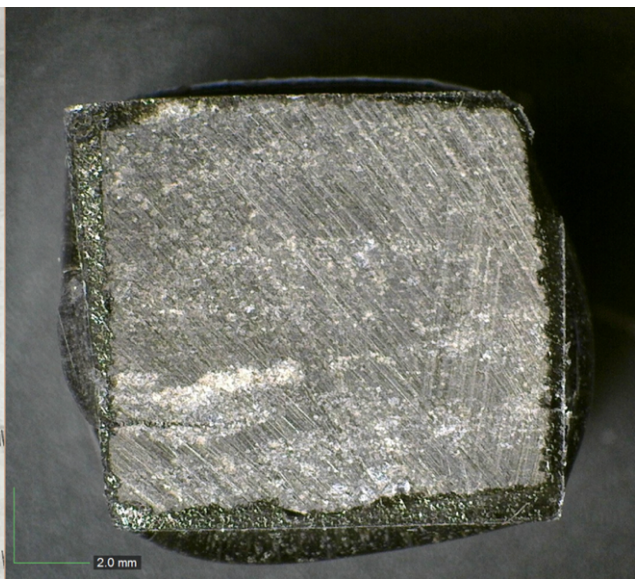
Core plugs of sample OA5137-M were difficult to obtain due to laminations or a complex fracture network. Sample mass of SZ5293-U was not sufficient enough to obtain core plugs. Once cubes, slabs, and plugs were obtained, the leftover sample mass was used to obtain GRI (Gas Research Institute) fractions of 500-851 μm .

To reduce sample size of the samples for GRI production, larger chunks of samples were broken down using a hammer and were eventually placed in a grinder once small enough to be about 1 cm in linear dimensions. From the grinder, samples were broken down even further using a pestle and mortar. The remaining samples were placed in a stacked sieve system that contained sizes #8/#12, #12/#20, #20/#35, #35/#80, #80/#200, and <#200. GRI+ samples were #8/#12 and GRI samples were #20/#35. Sample mass obtained for each sample size were measured and recorded. Core plugs, thin slabs, GRI+/GRI fraction, and powder (<#200) were taken to collaboration labs in China to run a variety of tests. Core plugs were used for helium porosity and nitrogen permeability analysis, thin slabs were used for contact angle measurements with fluids (DI water, API brine, 20% IPA in DI water, n-decane), GRI+ was used for matrix permeability and MICP tests, GRI was used for matrix permeability, MICP, and nitrogen sorption isotherm tests, and powder (<#200) was used for TOC, XRD, and pyrolysis.

JW4892-L



OA5137-M



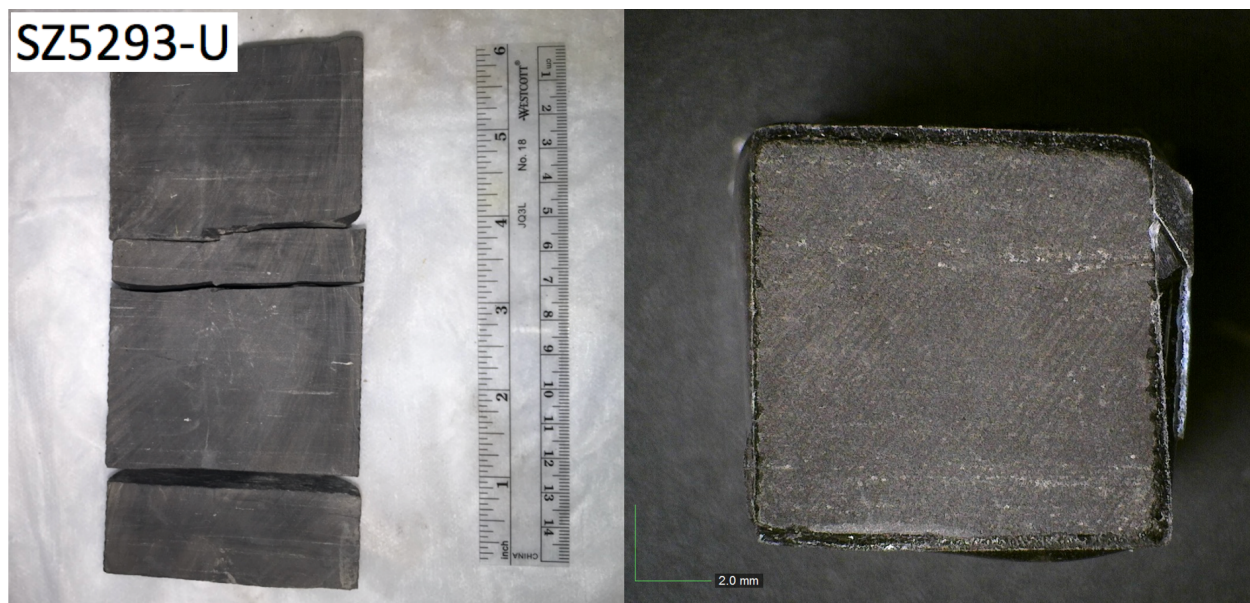


Figure 3-1 Core samples: whole sample and zoomed face of cubes.



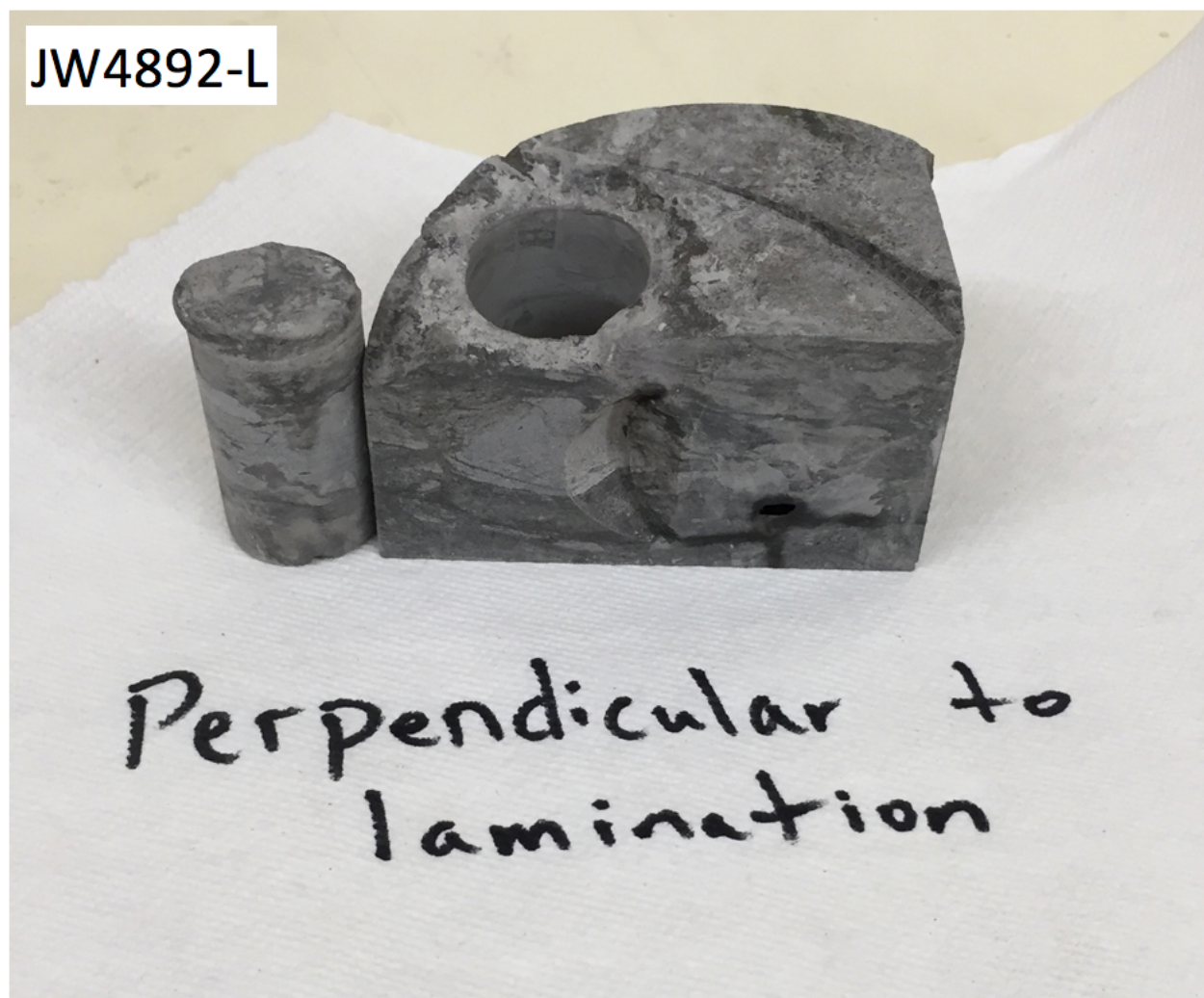


Figure 3-2 Example of core plugs taken parallel and perpendicular to lamination.

3-3 XRD

XRD (X-Ray Diffraction) was performed on all three samples in order to determine mineralogical makeup. Tests were run using the Shimadzu MAXima XRD-7000 at the Shimadzu lab located at the University of Texas at Arlington (Figure 3-3). The equipment identifies the individual minerals present in the sample as well as its corresponding weight percentage. The individual minerals are referred to as “Phase ID”. Individual minerals were then assigned to their corresponding “type”. “Types” include clay, carbonate, feldspar, mica, oxide, quartz, and sulphide. A summary of all three samples was provided in table format.

The XRD-7000 analyzes crystalline states under normal atmospheric conditions. X-rays are directed towards the sample which is located on the axis of the spectrometer. The x-rays are then diffracted by the sample. Changes in the diffracted x-ray intensities are recorded and plotted against the sample’s rotation angles. The combination of intensities and rotation angles is referred to as the x-ray diffraction pattern of the sample. Based on the diffraction pattern, lattice constant determination and/or stress determination of the sample is analyzed. XRD data on other samples from various wells was also conducted by The Mineral Lab and was provided by the New Mexico Bureau of Geology as well as the public database of the USGS Core Research Center in Denver, Colorado. Results and methods of The Mineral Lab are located in the appendix (Appendix A).



Figure 3-3: XRD instrument at Shimadzu Center at the University of Texas at Arlington.

3-4 Pyrolysis

Pyrolysis was conducted in China on each sample to determine the generative capacity of hydrocarbons. Although pyrolysis reveals important information about source rock potential, it is important to note that these tests only reflect the sample's present day characteristics. In the lab, samples are exposed to high temperatures over a short period of time. In nature, these rocks are subject to slightly lower temperatures but over much longer spans of time, sometimes even hundreds of millions of years. Hydrocarbon generation potential can also be underestimated during pyrolysis since clay minerals sometimes convert bitumen to carbonaceous residue. Under reservoir conditions, bitumen is expelled more readily (Waples, 1985).

Geochemical analysis was also performed on an assortment of Mancos samples from various wells in San Juan County by Core Lab Petroleum Services. The data was provided by the

New Mexico Bureau of Geology and was used to supplement my data. Results and methods Core Lab Petroleum Services can be found in the Appendix B.

Pyrolysis data obtained from all three samples includes S1, S2, S4, TOC, and T_{\max} values. S1 refers to the total amount of hydrocarbons (mg HC/g rock) present before pyrolysis testing begins. S2 refers to the total volume of hydrocarbons formed during pyrolysis of the sample. This value can help develop a quantifiable estimation of the remaining hydrocarbons that can be generated from the sample. S1 and S2 values can lead to some inferences regarding the petroleum system of interest. For example, when S1 is larger than S2, one can reasonably assume that hydrocarbons in the sample came from another source, therefore establishing the fact that the sample being studied is in fact the reservoir rock. T_{\max} refers to the temperature (degrees Celsius) at which hydrocarbon generation is at its maximum rate, or the S2 peak. It is important to note that from the pyrolysis data mentioned above, many other derivations can be made to help describe the maturation of the sample. Vitrinite reflectance (R_o), which represents a measure of the percentage of incident light reflected from the surface of vitrinite particles in a sedimentary rock, can be estimated. Production index can also be calculated, which describes the generation zone in which the sample lies (Waples, 1985).

3-5 Wettability/Contact Angle Methods

Successful recovery of hydrocarbons from low permeability reservoirs highly depend on the wetting characteristics of the reservoir. Different fluids behave differently when contact is made with rocks of varying composition. A wide variety of tests can be conducted on shales to describe their wettability characteristics. One test in particular is measuring the angle created by contact of a fluid and the surface of the sample. Contact angle measurements are a helpful tool, but can create issues due to contamination and roughness of the sample surface (Morrow, 1990;

Hu et al., 2014). To assess the wettability of the Mancos Shale, contact angles between fluid and sample surface were measured using the USA KINO SL200KB, a professional interface chemical measurement system. The specific angle, Θ , is the angle between tangent of gas-liquid interface and the solid-liquid interface formed at the three phases' boundary where liquid, vapor and solid intersect. The instrument used for testing distributed a drop of fluid to the sample surface while simultaneously capturing images of the events. The angle produced by the contact of the fluid and sample was measured and recorded. Fluids distributed from the instrument for contact angle measurement include DI water, API brine, 20% IPA in DI water, and n-decane. The test aims at quantitatively assessing a sample surface's wettability characteristics including the spreading behavior of various fluids. If the fluid spreads readily on the surface of the sample, it will produce a relatively low contact angle (Figure 3-4).

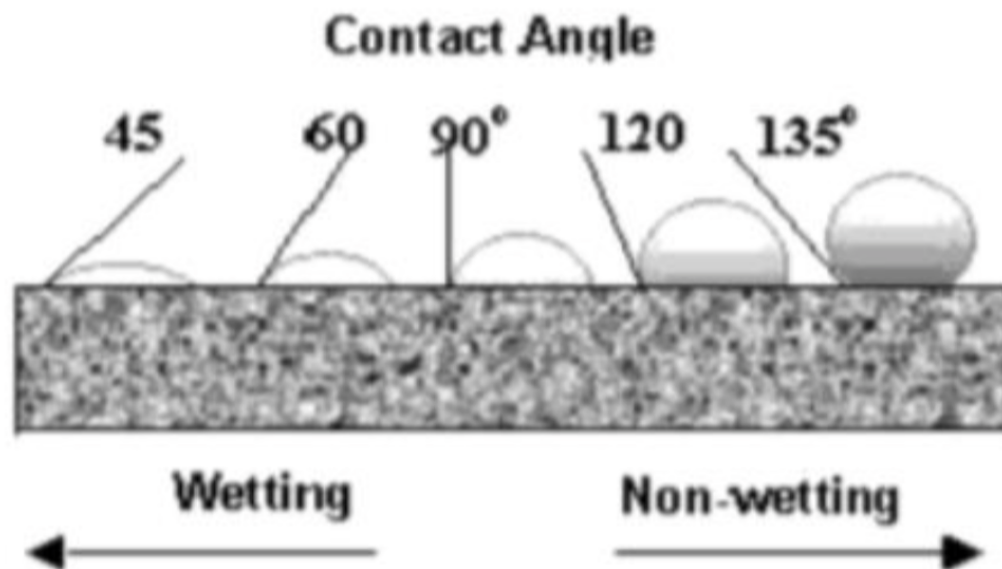


Figure 3-4 Contact angles produced by wetting and non-wetting fluids.

3-6 Imbibition

Imbibition tests are run to measure the connectivity of pores throughout the sample. By submerging the exposed face of an initially unsaturated sample in a fluid, the mass of fluid uptake is recorded over time. Fluids the core samples are exposed to include DI water and n-decane. The core sample is initially unsaturated in order to produce imbibition by capillary pressure gradient. In order to assess pore connectivity, slopes from imbibition data retrieved from testing are evaluated. If samples display low imbibition slope values, according to percolation theory, porous media is not well connected (Sahimi, 1994; Stauffer and Aharoney, 1994; Hunt et al., 2014; Hu et al., 2014). This is witnessed by a slope of roughly 0.25. A relatively well connected pore network would display a slope of about 0.5. Cumulative imbibition can be expressed over time by the following equation:

$$I(t)=St^{0.5}$$

Where:

$I(t)$ = Cumulative Imbibition (mm)

S = Sorptivity (m)

T = Time (s)

Sorptivity is another parameter commonly used to measure imbibition behavior. Assuming that the gravitational force is negligible, cumulative imbibition is related to the square-root-of-time (Philip, 1957; Kao and Hunt, 1996; Hu et al., 2001, Tokunaga and Wan, 2001). Accordingly, the effective wetted distance (L_d) is equal to the cumulative imbibition divided by the step change in volumetric fluid content ($\Delta\theta$). The step change in volumetric fluid content is usually less than or equal to the porosity of the porous media.

$$L_d = H/\Delta\theta$$

Combining the cumulative imbibition and effective wetted distance equation, the effective wetting front distance can be conveyed as (Tokonaga and Wan, 2001):

$$L_d = \frac{S}{\Delta\theta} \sqrt{t}$$

Kao and Hunt (1996) determined that when the porous medium has a contact angle of zero (perfect wettability) towards a fluid, a one-fourth power relationship exists between the permeability and effective wetted distance (Kao and Hunt, 1996; Tokunaga and Wan, 2001).

With this in mind, we use the following equation assuming imbibition behavior in one-dimensional medium, and a porous medium with good connectivity:

$$L_d = B \sqrt{\sigma/\mu} k_{imb}^{1/4} \sqrt{t}$$

Where

B = geometry of porous medium

σ = liquid-gas surface tension (mN/m)

μ = fluid viscosity (mPa·s)

k_{imb} = permeability of porous media (m^2)

t = time (s)

Combining the two equations results in a relationship between a fourth-power of sorptivity and permeability (k_{imb}) that can be obtained from imbibition tests. The following equation expresses this relationship (Kao and Hunt, 1996; Tokonaga and Wan, 2001):

$$k_{imb} \sim \left(\frac{\mu}{\sigma}\right)^2 \left(\frac{S}{B\Delta\theta}\right)^4$$

Sample cubes are initially oven-dried at 60°C to eliminate any fluids that may be present in the connected pore spaces. Once a constant weight is achieved, the sample is placed in a desiccator before testing to cool down for 30 minutes. A variety of weights are measured and recorded using the Shimadzu AUW220WD balance before and after testing. Weight measurements include: the dry sample alone, sample holder only, sample and holder together, and petri dish and liquid (DI water, n-decane) together. The sample is then immersed in the solution parallel to lamination until the solution reaches approximately 1 mm of the sample (Figure 3-5). Tests range in time depending on the solution being used. DI water conducts a 24-hour long test and n-decane conducts an 8-hour long test.

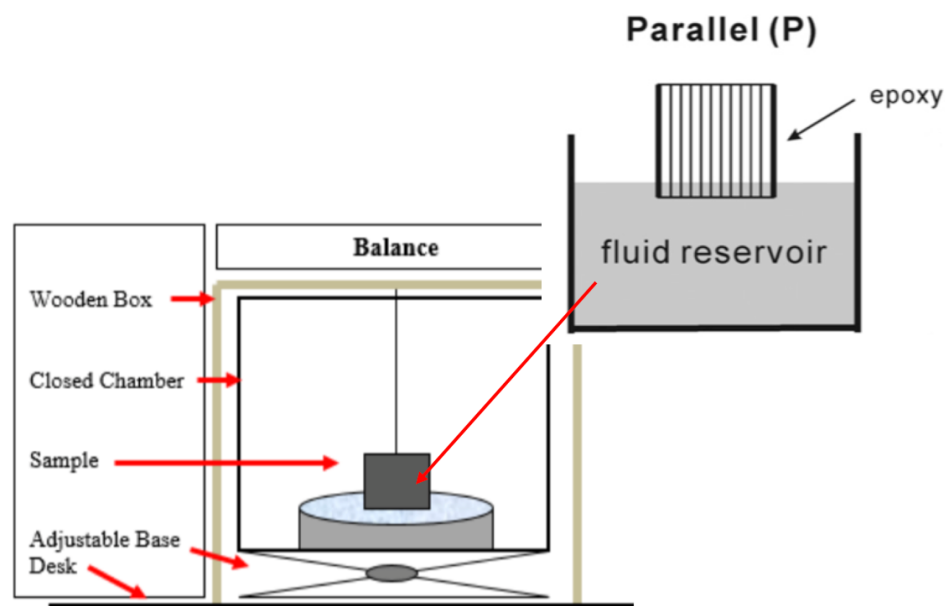


Figure 3-5: Model of apparatus used for imbibition tests (modified from Hu et al., 2014).

Imbibition tests were conducted using an apparatus similar to one shown in Figure 3-5. The 1 cm cube was placed in a holder and attached to a thin metal wire inside a closed chamber. The metal wire was connected to the Shimadzu AUW220WD balance where measurements were recorded

on a computer at predetermined time intervals. For the first 2 minutes, a measurement was recorded every second. For the next hour, measurements were recorded every 30 seconds. The remaining duration of the test recorded measurements every 5 minutes. It is important to note that for the first few seconds of each imbibition test, weights fluctuated since the sample had not yet settled into the fluid. Once the sample had settled, weights recorded by the balance began to steadily increase.

Depending on which fluid was used (DI water or n-decane) during testing, two vials of the respective fluid were placed in the chamber along with a petri dish containing the fluid of choice. In order for the sample to come into contact with the fluid in the petri dish, the closed chamber was raised or lowered accordingly using the adjustable base of the apparatus. Once testing was completed, the sample was raised from contact with the fluid and petri dish by lowering the adjustable base. Excess fluid located on the face of the sample that was exposed to the fluid during testing was wiped dry with a pre-moistened Kimwipe. The Kimwipe was weighed twice to determine the weight of the excess fluid. The difference in weights between the dry Kimwipe and the Kimwipe with excess fluid was measured to determine the weight of the excess fluid from the sample's face. As previously mentioned, weights were recorded of the sample, the sample holder, etc. Sample and sample holder were weighed again to check if any condensed fluid was still on the holder and to perform a correction of buoyancy effects on balance weights (Hu et al., 2014). The petri dish and fluid were weighed to cross examine the cumulative imbibition recorded by the computer and to see if any evaporation of fluid occurred.

3-7 Low-Pressure Gas Physisorption

The low-pressure gas physisorption test was performed using the Quantachrome Autosorb iQ3-MP at China University of Geosciences (CUG) (Figure 3-6). The purpose of the

study is to measure the surface area and pore structure of a porous sample. By using nitrogen gas adsorption procedures, an instrument analyzes the surface area of the sample as well as its pore structure. This process is achieved by administering nitrogen gas to the sample surface at varying pressures. The amount of nitrogen gas adsorbed by the sample is recorded at their respective pressures, resulting in gas adsorption/desorption isotherms. Both DFT (Density Functional Theory) and BJH (Barrett-Joyner-Halenda) models are used for pore size distribution. The DFT model measures pore throat widths in the micropore to mesopore range. The BJH model measures pore throat widths in the mesopore range, with the ability to detect a small fraction of macropores. In conjunction, both models give a better description of the pore size distribution of a sample. Results provide the percentage of pore throat diameters of varying sizes.



Figure 3-6 Quantachrome Autosorb iQ3-MP gas sorption instrument used at CUG.

3-8 MICP

Mercury Intrusion Capillary Pressure (MICP) can obtain a variety of pore structure properties including bulk density, particle density, pore surface area, porosity, pore-throat size distribution, permeability, and tortuosity. The analysis is performed using the Micrometrics Autopore IV 9510 (Norcross GA) apparatus at NJU (Nanjing University). The apparatus forces mercury, a non-wetting fluid, into the pore throats of a sample at incremental pressures up to 54,000 psia. At this maximum pressure, pore throat diameters were measured to be roughly 3.4 nm using the Washburn equation. In order to invade the pore throat, a large enough force must be applied to exceed the capillary pressure. Since a large amount of unconventional plays contain nanopores with pore throats of this small size, MICP is a popular method to use in the characterization of unconventional reservoirs.

The Washburn equation assumes that all pores have a cylindrical shape (Hu et al., 2015). The equation demonstrates that the intruded pore throat has an inverse relationship with the externally applied pressure (Washburn, 1921; Gao and Hu, 2012)

$$\Delta P = - \frac{2\gamma \cos \theta}{R}$$

Where:

ΔP = External pressure (psia)

γ = Surface tension of mercury (mN/m)

θ =Contact angle formed by mercury and pore wall (degree)

R = Radius of pore throat (μm)

Since contact angles are recently found to exponentially increase as pore throat diameters decrease, while the Washburn equation assumes a constant contact angle and surface tension, we use a modified Washburn equation (Wang et al., 2016). The equation is as follows:

$$\Delta P = - \frac{2\gamma_{Hg}(R) \cos \theta_{Hg}(R)}{R}$$

Katz and Thompson (1986) found that permeability can be indirectly obtained through MICP. The equation is as follows:

$$k = \left(\frac{1}{89}\right) (L_{max})^2 \left(\frac{L_{max}}{L_c}\right) \phi S(L_{max})$$

Where:

k = Permeability of air (m^2)

L_{max} = Diameter of pore throat at maximum hydraulic conductance (μm)

L_c = Diameter of pore throat at specific inflection point (μm)

Φ = Porosity (fraction)

S = Mercury saturation at L_{max} (fraction)

3-9 Production Data

Dr. Hu's research group at the University of Texas at Arlington has access to a complimentary subscription to DrillingInfo. Data provided by DrillingInfo was used to analyze oil and gas production from wells containing samples in the study. Production data from the wells of interest consists only of cumulative oil and gas volumes and well status.

Chapter 4 Results

4-1 XRD

XRD results show a total of 13 different identified minerals, with various similarities and differences among the three Mancos C samples. Sample SZ5293-U displays the most mineralogic diversity, containing 10 out of the 13 identified minerals, while sample JW4892-L contains 9 out of 13 and OA5137-M contains 8 out of 13 (Figure 4-1). Samples JW4892-L and OA5137-M show very similar mineralogical components with high volumes of quartz compared to sample SZ5293-U. Sample SZ5293-U does not show the large amount of quartz that samples JW4892-L and OA5137-M contain, but does display a much larger quantity of carbonate material. Within the carbonate “type”, samples JW4892-L and OA5137-M show almost identical amounts of calcite and dolomite. Sample SZ5293-U contains almost identical amounts of dolomite as the other samples, but contains a carbonate mineral not present in the other samples, Ankerite.

All three samples show clay contents ranging from 17.6 to 27.7%. Samples SZ5293-U and OA5137-M only contain illite, palygorskite, and muscovite respectively. Sample JW4892-L contains illite, palygorskite, muscovite, and kaolinite. Although Figure 4-1 separates muscovite from clay content, it is lumped together for purposes of this paper, since illite converts to muscovite due to an increase in temperature during burial. According to most documented literature, the Mancos typically contains around 20% clay content. Discrepancy in clay content between samples can be explained by location within the basin as well as the lithological heterogeneity of the formation, both vertically and laterally.

Sample		NMSZ5293		
Phase ID	Type	Wt. %	±	Chemical Formula
Ankerite	Carbonate	8.6	0.9	Ca(Fe+2,Mg,Mn)(CO ₃) ₂
Dolomite	Carbonate	13	1.1	CaMg(CO ₃) ₂
Calcite	Carbonate	29.9	0.8	CaCO ₃
Albite	Feldspar	0.8	0.3	NaAlSi ₃ O ₈
Illite-1M	Clays	2.7	0.3	(K,H ₃ O)Al ₂ (Si ₃ Al)O ₁₀ (H ₂ O,OH) ₂
Muscovite 3T	Mica	14.9	1.3	K(Al _{1.91} Fe _{.09})(Si ₃ Al)O ₁₀ (OH) ₂
Hematite	Oxide	1.2	0.2	Fe ₂ O ₃
Franklinite	Oxide	6.8	0.7	(Zn,Mn+2,Fe+2)(Fe+3,Mn+3)O ₄
Quartz	Quartz	20.2	0.6	SiO ₂
Pyrite	Sulphide	2	0.2	FeS ₂

Sample		NMOA5137		
Phase ID	Type	Wt. %	±	Chemical Formula
Calcite	Carbonate	9.3	0.3	CaCO ₃
Dolomite	Carbonate	12.5	0.5	MgCa(CO ₃) ₂
Palygorskite	Clay	1.7	0.3	(Mg,Al) ₂ Si ₄ O ₁₀ (OH) ₄ H ₂ O
Albite	Feldspar	5.2	0.6	NaAlSi ₃ O ₈
Muscovite 3T	Mica	26	1.4	K(Al _{1.91} Fe _{.09})(Si ₃ Al)O ₁₀ (OH) ₂
Ulvospinel	Oxide	1.3	0.2	Fe ₂ (TiO ₄)
Quartz	Quartz	41.8	0.9	SiO ₂
Pyrite	Sulphide	2.1	0.1	FeS ₂

Sample		NMJW4892		
Phase ID	Type	Wt. %	±	Chemical Formula
Calcite	Carbonate	8.2	0.2	CaCO ₃
Dolomite	Carbonate	14.1	0.3	MgCa(CO ₃) ₂
Illite-2M2	Clay	0.2	0.1	(K,H ₃ O)Al ₂ (Si ₃ Al)O ₁₀ (H ₂ O,OH) ₂
Palygorskite	Clay	1.5	0.2	(Mg,Al) ₂ Si ₄ O ₁₀ (OH) ₄ H ₂ O
Kaolinite	Clay	2.3	0.2	Al ₂ Si ₂ O ₅ (OH) ₄
Albite	Feldspar	5.9	0.5	NaAlSi ₃ O ₈
Muscovite 3T	Mica	18.2	0.9	K(Al _{1.91} Fe _{.09})(Si ₃ Al)O ₁₀ (OH) ₂
Quartz	Quartz	48.7	0.7	SiO ₂
Pyrite	Sulphide	0.9	0.1	FeS ₂

Summary of Results

	JW4892-L			OA5137-M			SZ5293-U	
	Wt. %	+/-		Wt. %	+/-		Wt. %	+/-
Carbonate	22.3	0.5		21.8	0.8		51.5	2.8
Clay	4	0.5		1.7	0.3		2.7	0.3
Feldspar	5.9	0.5		5.2	0.6		0.8	0.3
Mica	18.2	0.9		26	1.4		14.9	1.3
Oxide	-	-		1.3	0.2		8	0.7
Quartz	48.7	0.7		41.8	0.9		20.2	0.6
Sulphide	0.9	0.1		2.1	0.1		0.2	0.2

Figure 4-1 XRD results showing numerical weight percentage of individual minerals as well as minerals grouped by “type”.

Mineralogy of samples from other wells located in the Tocito Marine Bar play and Offshore Mancos play were also looked at to determine if any correlations existed (Appendix C). From data acquired by Mineral Lab, samples located in the Tocito Marine Bar contain more quartz than samples in the Offshore Mancos play. This corresponds directly with XRD results of sample JW4892-L acquired at the Shimadzu lab. Offshore Mancos play samples also contain slightly more carbonate material than Tocito Marine Bar samples, which directly corresponds with results obtained from the Shimadzu lab. To simplify the quantitative assessment of mineral percentages of samples within the different plays, averages of QFM (quartz, feldspar, additional minerals), Clay, and Carbonate content from each well were taken (Table 3). It is important to note that mineralogic components from each well identified by Mineral Lab cover a multitude of depths within the Upper Mancos Shale, but as a whole, can help explain the discrepancies that exist between the two play types. Overall, Tocito Marine Bar Play samples consist of mixed mudstones and mixed siliceous mudstones (Figure 4-2), while Offshore Mancos samples consist of mixed mudstones, mixed siliceous mudstones, and carbonate/siliceous mudstones (Figure 4-3).

Table 3: Table displaying an average of mineralogic data obtained by Mineral Lab. Tocito Marine Bar (yellow) and Offshore Mancos (blue).

Play Name	QFM (%)	Clay (%)	Carbonate (%)
Tocito Marine Bar Play	50.7	23.9	25.4
Offshore Mancos Play	43.3	26.3	30.4

Tocito Marine Bar Play

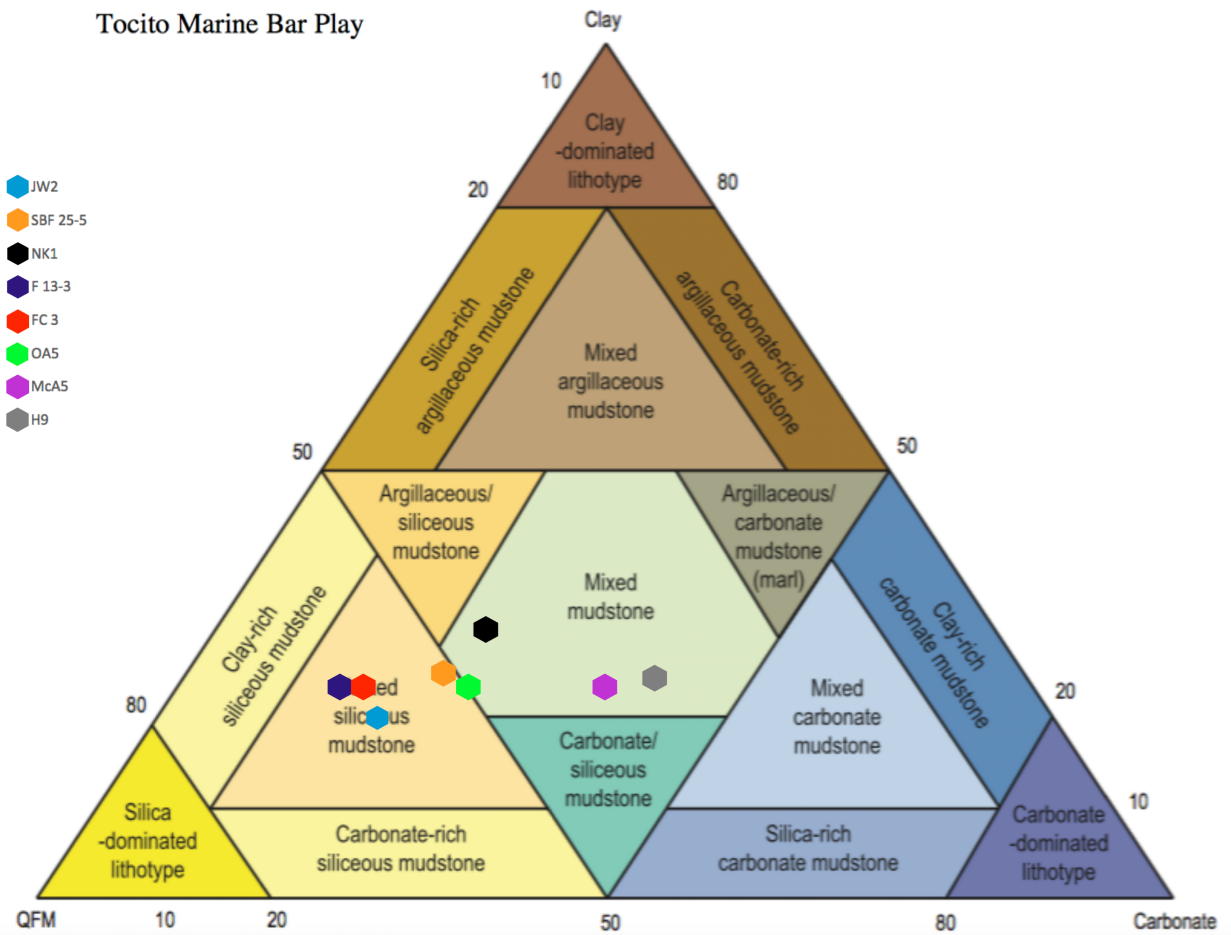


Figure 4-2 Mineralogy averages from samples located in Tocito Marine Bar Play plotted on Schlumberger's sCore classification ternary diagram. Well "JW2" includes sample JW4892-L and well "OA5" represents sample OA5137-M.

Offshore Mancos Play

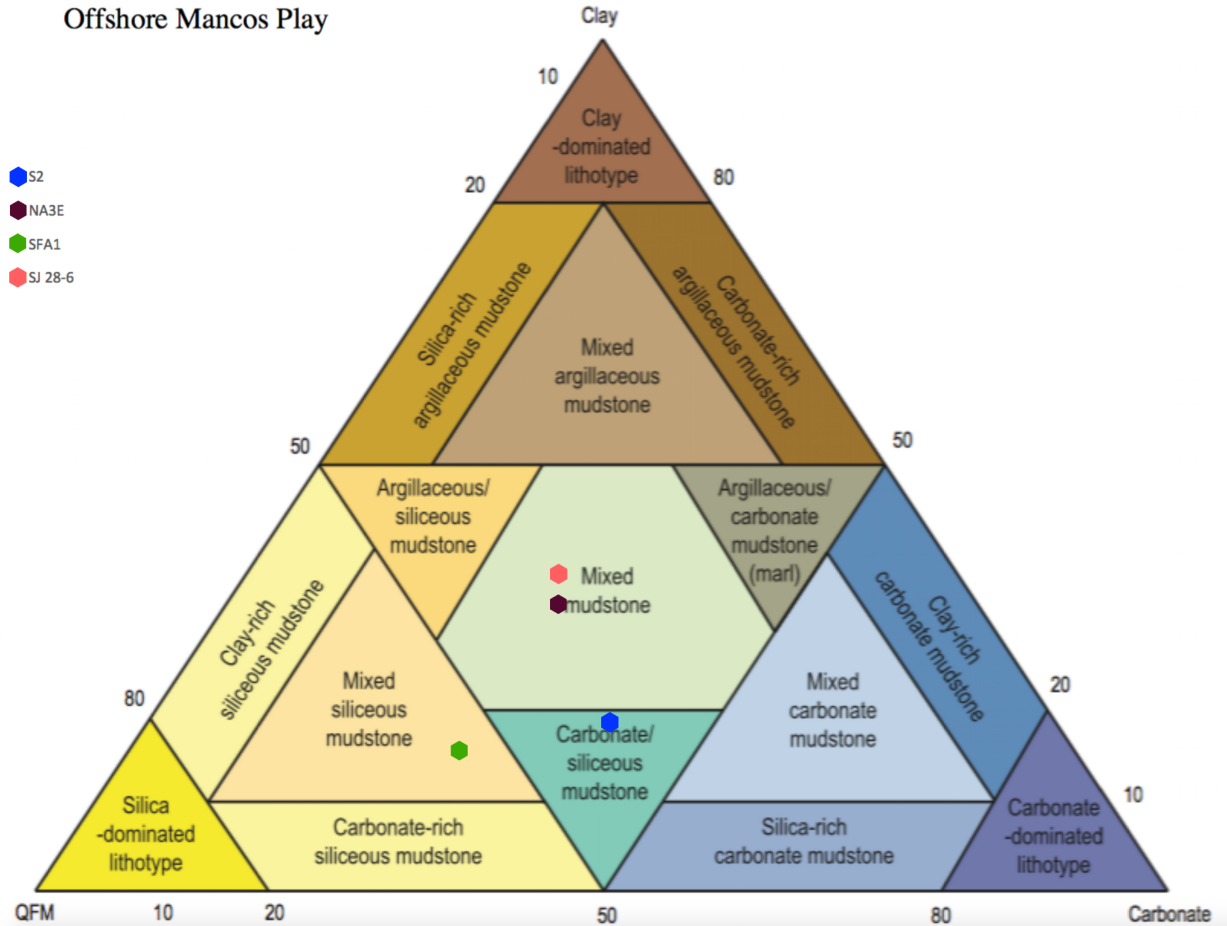


Figure 4-3 Mineralogy averages from samples located in Offshore Mancos Play plotted on Schlumberger's sCore classification ternary diagram. Well "S2" includes sample SZ5293-U.

4-2 Pyrolysis

Pyrolysis data obtained from powder sample size is shown Table 4 below. Values not obtained by pyrolysis of samples include S3, and therefore hydrogen index (HI) as well as oxygen index (OI). Vitrinite reflectance (Ro) was calculated using the equation found below (Jarvie et al., 2001). Ro values ranged from 0.63- 0.81, indicating relatively mature samples (Table 4). Production index (PI) is another tool to measure the maturity of a sample, and can be found by using the following equation:

$$Ro = (0.018)(T_{max} - 7.16)$$

$$PI = S1/(S1 + S2)$$

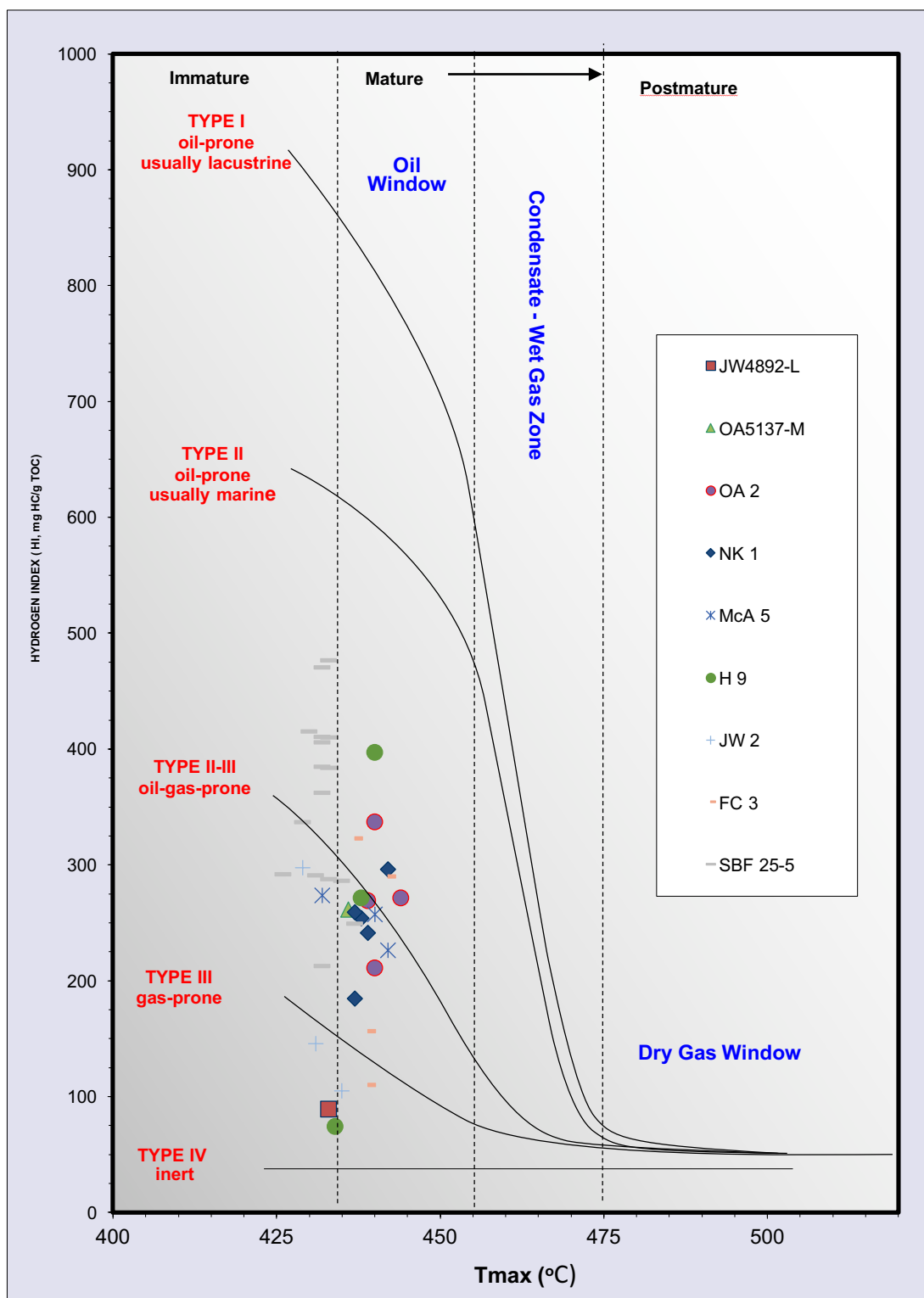
Production indexes <0.10 correlate with immature samples. Production indexes ranging from 0.10-0.30 correlate with the “oil generation” zone, Finally, production indexes >0.30 correlate with the “gas generation/oil cracking” generation zone. Based on this criterion, samples are not immature, and fall within the “Oil Generation” and “Gas Generation/Oil Cracking” zones of maturity. Data obtained from samples coincide with previous studies on the Mancos Shale, which found TOC values to average roughly 1-2%, and have maturities of about 0.65-1.5 (Broadhead, 2013).

Table 4 Pyrolysis data obtained by UTA. Tocito Marine Bar (yellow) and Offshore Mancos (blue).

Sample	JW4892-L	OA5137-M	SZ5293-U
S1 (mg Hc/g)	0.38	1.61	2.13
S2 (mg Hc/g)	0.87	6.62	3.79
S4 (mg CO ₂ /g rock)	8.79	18.43	22.98
TOC (%)	0.98	2.53	2.79
T _{max} (degrees)	433	436	450
Ro	0.63	0.69	0.94
PI	0.30	0.20	0.36

To further supplement data obtained from pyrolysis, data from Weatherford labs is provided in Appendix C. Samples from both Tocito Marine Bar Play and the Offshore Mancos Play show similar characteristics. Samples are shown to be immature to mature, containing type II, type II-III, and type III kerogens (Figure 4-4). As a whole, the majority of samples are type II

to type II-II kerogen, coinciding with results obtained by Broadhead (2013). In the western and more shallow region of the San Juan Basin, samples within the Tocito Marine Bar Play are primarily in the oil window. As one would expect, samples located within the Offshore Mancos in the more eastern and deeper region of the basin are more mature, thus having the potential to produce gas. Compared to T_{\max} values shown in Table 4, T_{\max} values from Weatherford labs show strikingly similar results, therefore validating results obtained by CUG. T_{\max} values obtained by CUG of Tocito Marine Bar samples (OA5137-M and JW4892-L) show 436 and 433 degrees Celsius, respectively. Of the 9 wells containing Tocito Marine Bar samples examined by Weatherford Labs, the average T_{\max} is 435 degrees Celsius. T_{\max} values acquired by CUG of Offshore Mancos samples (SZ5293-U) show 444 degrees Celsius. Of the 4 wells containing Offshore Mancos samples, the average T_{\max} is 448 degrees Celsius.



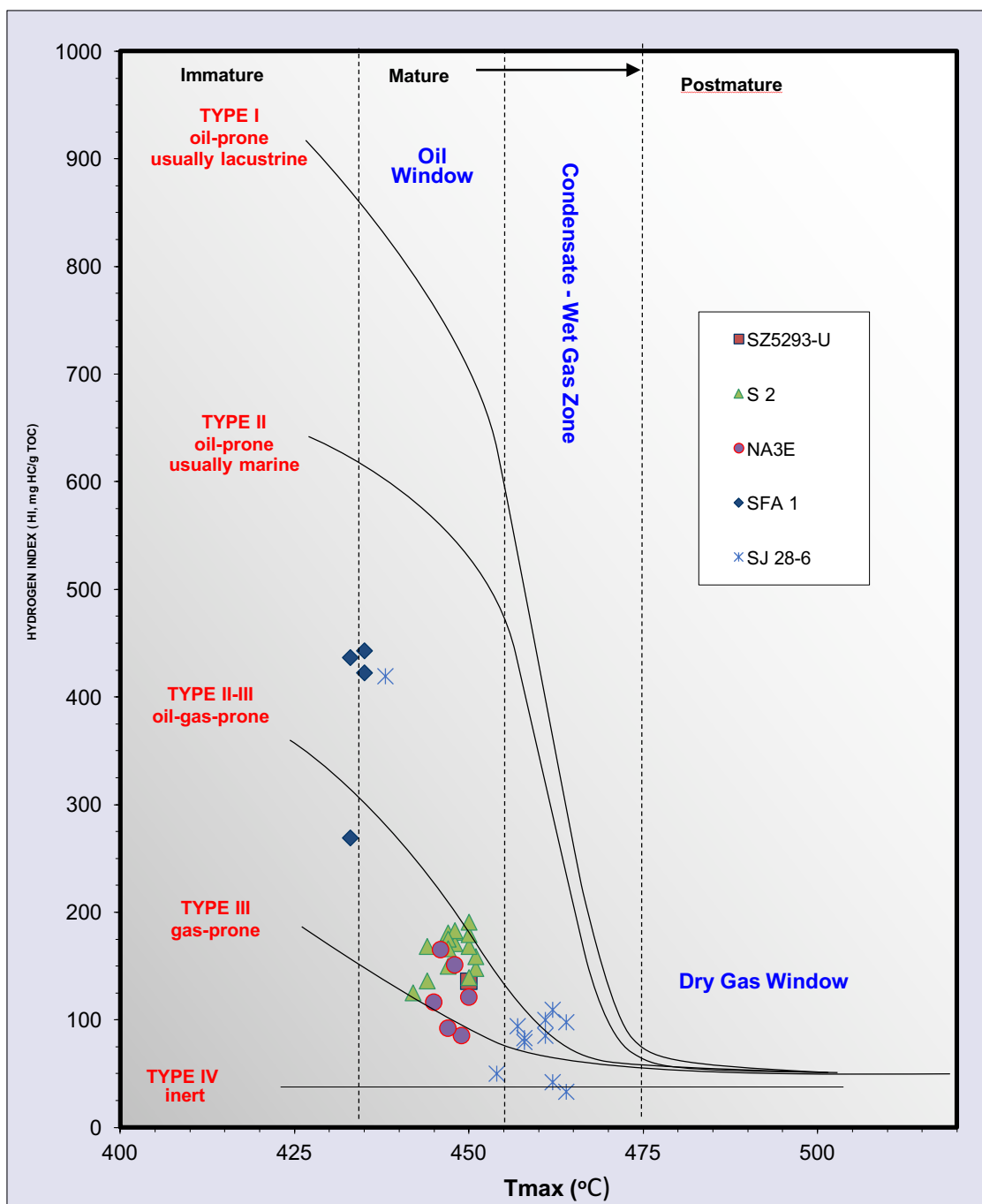


Figure 4-4 T_{max} vs. HI displays kerogen type of Tocito Marine Bar and Offshore Mancos plays.

4-3 Core Plug

Measured at Chengdu University of Technology (CDUT), helium porosity and permeability results were obtained using core plugs from samples OA5137-M and JW4892-L, both in the parallel and transverse directions to lamination (Table 5). Supplemental measurements were obtained in the process such as bulk volume and particle density. With respect to permeability testing, both Klinkenberg and air permeability methods were used, since results differ based on whether air or liquid is used as the flowing fluid. Klinkenberg permeability takes into account a liquid as the flowing fluid, instead of gas, like air permeability does. When air was used as the flowing fluid, permeability was found to be higher than when liquid was used due to slippage. To rectify the discrepancy in results, Klinkenberg developed a method that corrected gas permeability to an equivalent liquid permeability. Parallel to lamination, sample OA5137-M resulted in an air permeability of 3000 nD and a Klinkenberg permeability of 1000 nD. Transverse to lamination, air permeability was found to be 10,000 nD and Klinkenberg permeability was 5000 nD. Porosities from sample OA5137-M in the parallel and transverse directions were roughly similar, 1.96 and 1.77 respectively.

Table 5 Table displays helium porosity and permeability results of core samples.

Sample	Bulk volume (cm ³)	Weight (g)	Particle density (g/cm ³)	Pore volume (cm ³)	Porosity (Φ)	K air (nD)	k klink (nD)	Slip (psi/cm ²)
JW4892-L Parallel	12.51	31.31	2.50	0.89	7.14	5000	2000	84.01
JW4892-L Transverse	15.78	40.52	2.57	0.72	4.54	4000	2000	86.97
OA5137-M Parallel	5.73	14.57	2.54	0.11	1.96	3000	1000	94.13
OA5137-M Transverse	13.11	33.28	2.54	0.23	1.77	10000	5000	55.79

4-4 Wettability/Contact Angle

As mentioned in the methods section, all three samples were subject to contact angle tests. Contact angle measurements were recorded over time and results are graphically displayed in Figures 4-5, 4-6, and 4-7 respectively. Table 6 numerically displays contact angles obtained after 30 seconds. The detection limit of the instrument is 3 degrees. For n-decane, samples JW4892-L, OA5137-M, and SZ5293-U displayed very low contact angles ranging from less than 3 degrees to no more than 8 degrees. Low contact angles show that n-decane spread readily onto the surface of the sample. It is also important to note the relatively short amount of time needed for n-decane to spread onto the surface. For all three samples, it took no longer than 3 seconds for contact angles between the fluid and sample to fall below the detection limit of the instrument. For each individual sample, non n-decane fluids (API brine, 20% IPA, and DI water) displayed relatively similar results and form a cluster of data points, with one exception occurring with sample JW4892-L and API brine.

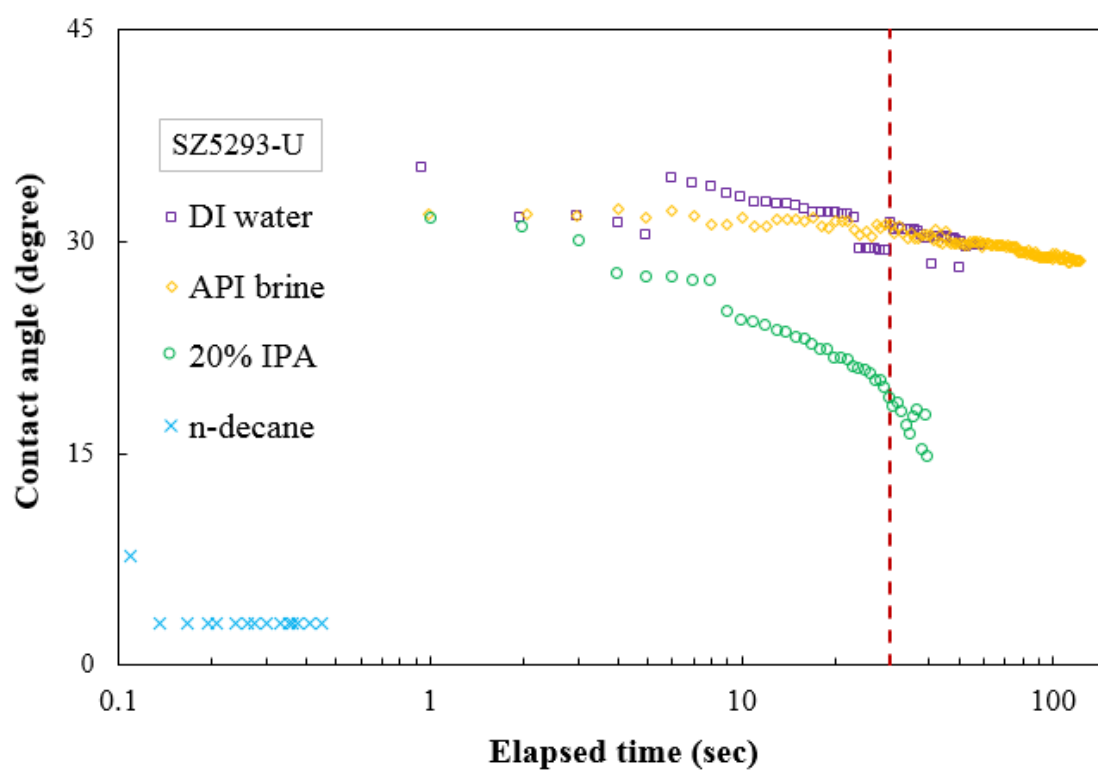


Figure 4-5 SZ5293-U contact angle results.

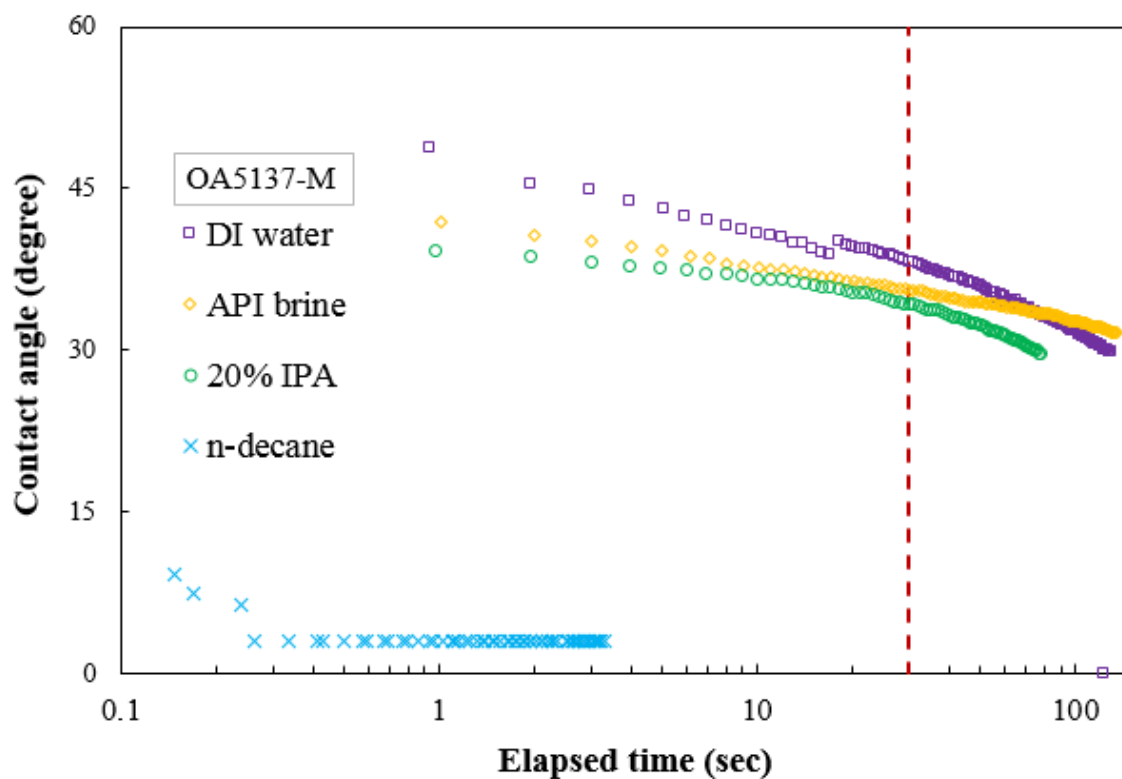


Figure 4-6 OA5137-M contact angle results.

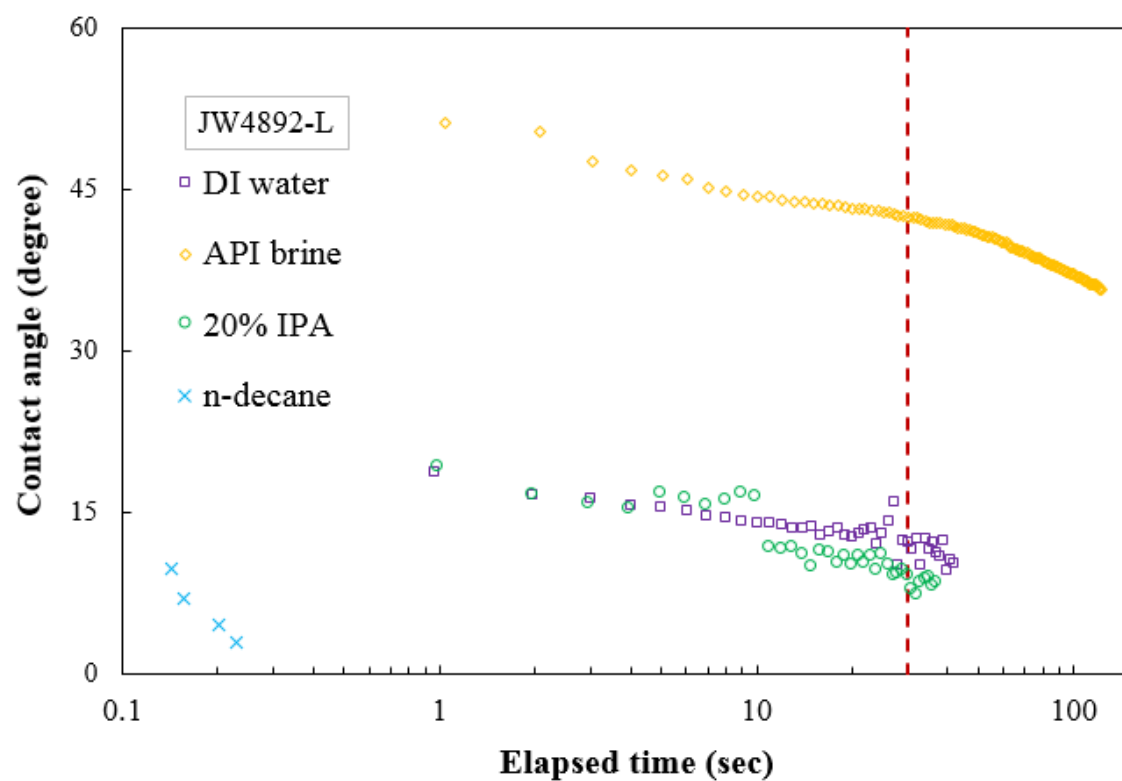


Figure 4-7 JW4892-L contact angle results.

Table 6 Contact angle data at 30 seconds for DI Water, API brine, and 20% IPA. At 30 seconds, n-decane contact angles fall below the detection limit of instrument.

Sample <i>ID</i>	DI Water	API brine	20% IPA	n-Decane
JW4892-L	12.20	42.40	9.13	-
OA5137-M	38.10	35.59	34.34	-
SZ5293-U	31.38	31.21	19.53	-
Average	27.23	36.40	21.0	-

4-5 Imbibition

Imbibition tests were run on all three samples using DI water and n-decane as wetting fluids to better understand pore connectivity to a fluid. Tests using DI water were run for approximately 24 hours and tests using n-decane were run for approximately 8 hours. To reduce errors associated with surface tension from modestly wetting characteristics of shale towards water, DI water tests were run multiple times per sample. Sample JW4892-L was run 3 times, while samples SZ5293-U and OA5137-M were run twice. Data was then plotted on graphs that show cumulative imbibition (mm; logarithmic) over time (sec; logarithmic) and slopes were identified to determine any trends in the data. Most shales typically display two to three slopes, indicating different stages of fluid imbibition. At times, a third stage is present, and represents the fluid reaching the top of the sample (Hu et al, 2001). This slope is very low, usually ranging from 0 to 0.1. These stages are referred to as Stage I, Stage II, and Stage III.

Stage I occurs when the sample comes into contact with the wetting fluid, usually lasting the first few seconds to a minute of the test. Stage I slopes are usually the highest of all the stages, since edge accessible pores or microfractures are invaded first. This can also be explained by the imbibing fluid entering the sample from more than one face, even though samples are epoxied to promote directional flow (Kiepsch et al., 2016). These pore throats usually do not communicate well with the pore networks of the inner rock matrix, thus decreasing rapidly after Stage I. Stage II commences after Stage I and usually displays a relatively linear and uniform slope. This stage qualitatively represents the connectivity of the sample's inner pore network. For purposes of this paper, Stage II is further examined. Stage III lasts the remainder of the test and usually represents the fluid reaching the top of the sample.

Results obtained from imbibition tests identify slopes for all three stages previously discussed. However, due to the complex nature of pore networks within each sample, some samples do not display all of the slopes. Some samples show a very small slope 2, and a larger slope 3. For purposes of this paper, and in an effort to characterize the connectivity of pore networks within the samples, we will focus on Stage II slopes, or connectivity slopes. These slopes are summarized in Table 7. Slopes closest to $\frac{1}{4}$ and $\frac{1}{2}$ are considered. All samples display initial Stage I slopes, ranging from 0.666 to 1.598. DI water Stage II slopes are present for all samples at least once during their respective runs, ranging from 0.178 to 0.361. Stage II slope averages for samples JW4892-L, OA5137-M, SZ5293-U are 0.231, 0.188, and 0.212 respectively. Examples of DI water imbibition results for JW4892-L, OA5137-M, SZ5293-U and are displayed in Figures 4-8, 4-9, 4-10, respectively.

Imbibition tests using n-decane as the imbibing fluid over an 8 hour span produced viable results. Two slopes were identified in JW4892-L and OA5137-M, and SZ5293-U. Stage I slopes

were not observed in all three samples. Stage II slopes ranged from 0.402 to 0.698. Out of all n-decane tests, the imbibing fluid only reached the top of the sample once. This occurred in sample JW4892-L, and is represented by a very low slope, approximately 0.028. Results for JW4892-L, OA5137-M, SZ5293-U and are displayed in Figures 4-11, 4-12, 4-13, respectively. As mentioned previously in the methods section, a predicted permeability was calculated for n-decane runs since connectivity slopes were near or around 0.5 (Table 7). The predicted values were found to be 144,317 nD, 389 nD, and 10.1 nD for samples JW4892-L, OA5137-M, and SZ5293-U, respectively. As n-decane connectivity slopes increased, predicted permeability decreased.

Table 7 Connectivity slopes obtained from imbibition tests of DI water and n-decane.

Sample ID	Fluid	Sample Dimensions (cm)	Connectivity Slope	Predicted k (nD)
JW4892-L	DI water	1.190 L × 1.110 W × 1.140 H	0.361	-
	n-decane	1.010 L × 1.150 W × 1.070 H	0.402	144,317
OA5137-M	DI water	1.15 L × 1.10 W × 1.10 H	0.178	-
	n-decane	1.146 L × 1.099 W × 1.105 H	0.698, 0.475	389
SZ5293-U	DI water	1.120 L × 0.995 W × 1.010 H	0.224	-
	n-decane	1.220 L × 1.230 W × 0.980 H	0.482	10.1

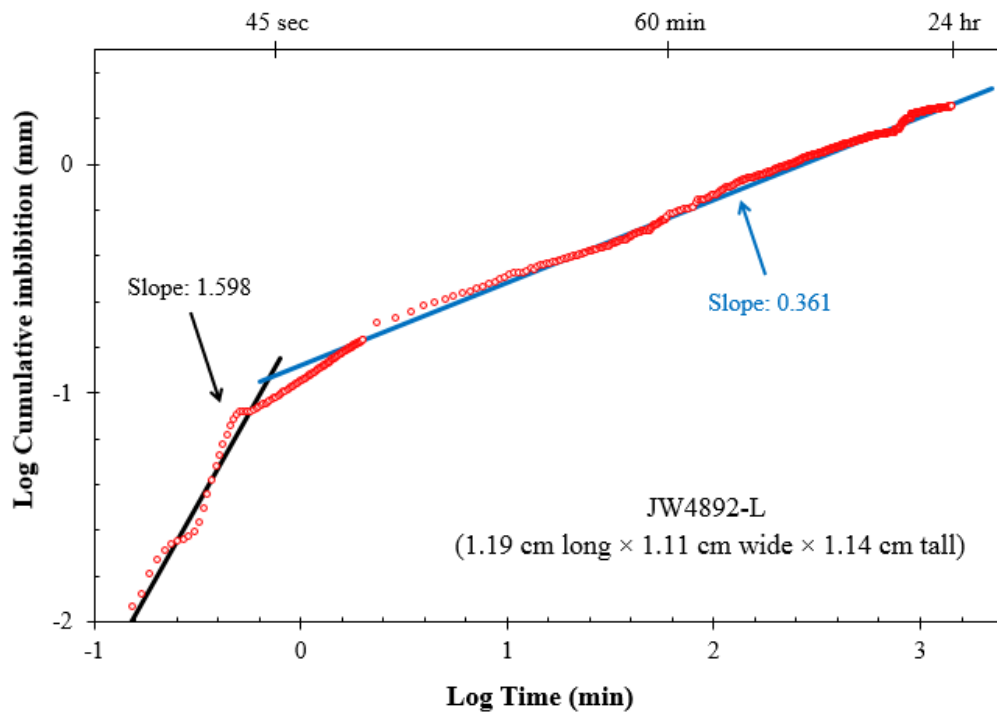


Figure 4-8 JW4892-L DI water imbibition results.

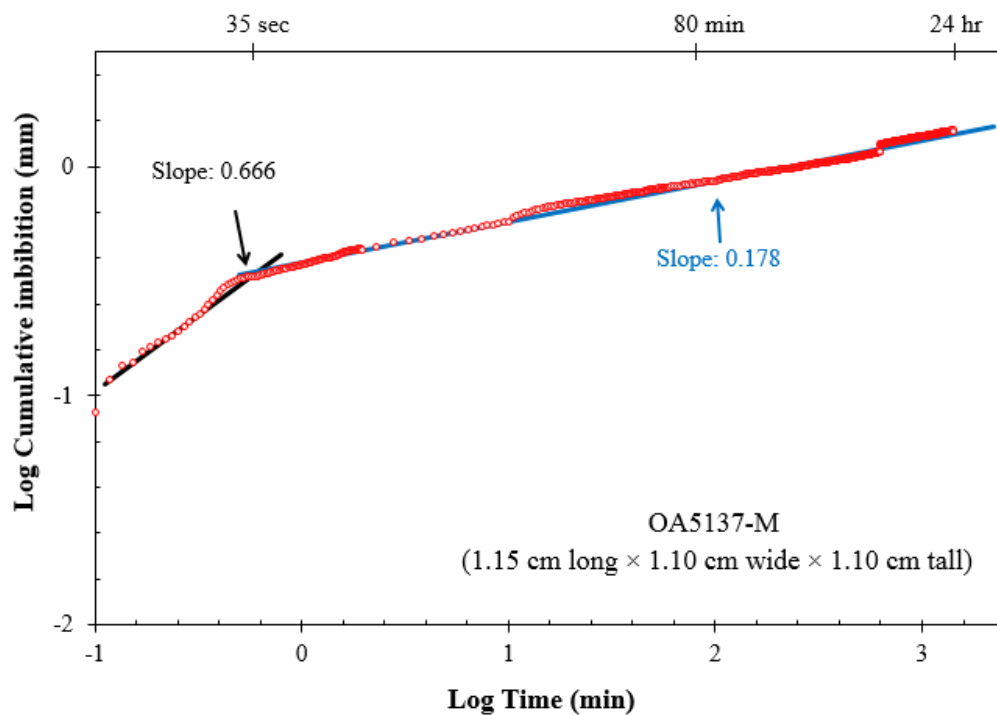


Figure 4-9 OA5137-M DI water imbibition results.

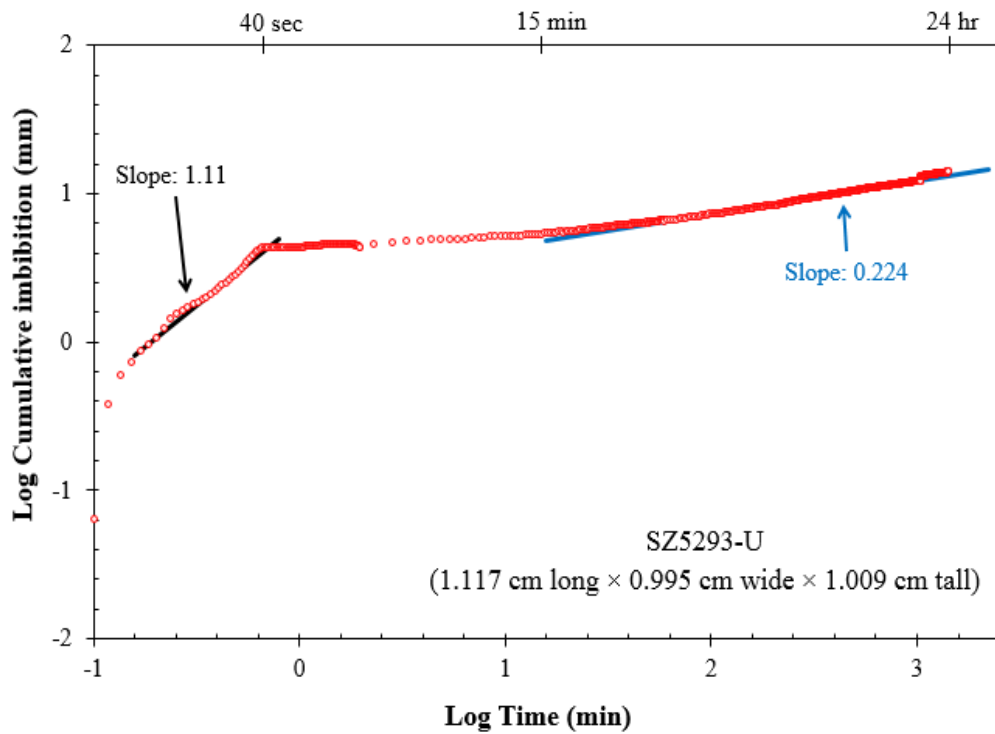


Figure 4-10 SZ5293-U DI water imbibition results.

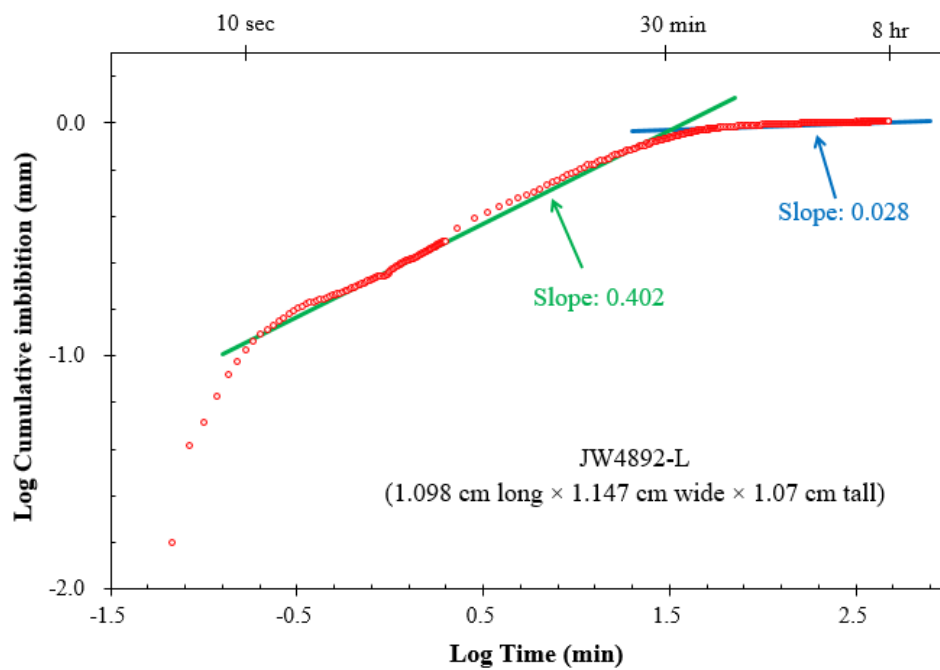


Figure 4-11 JW4892-L n-decane imbibition results.

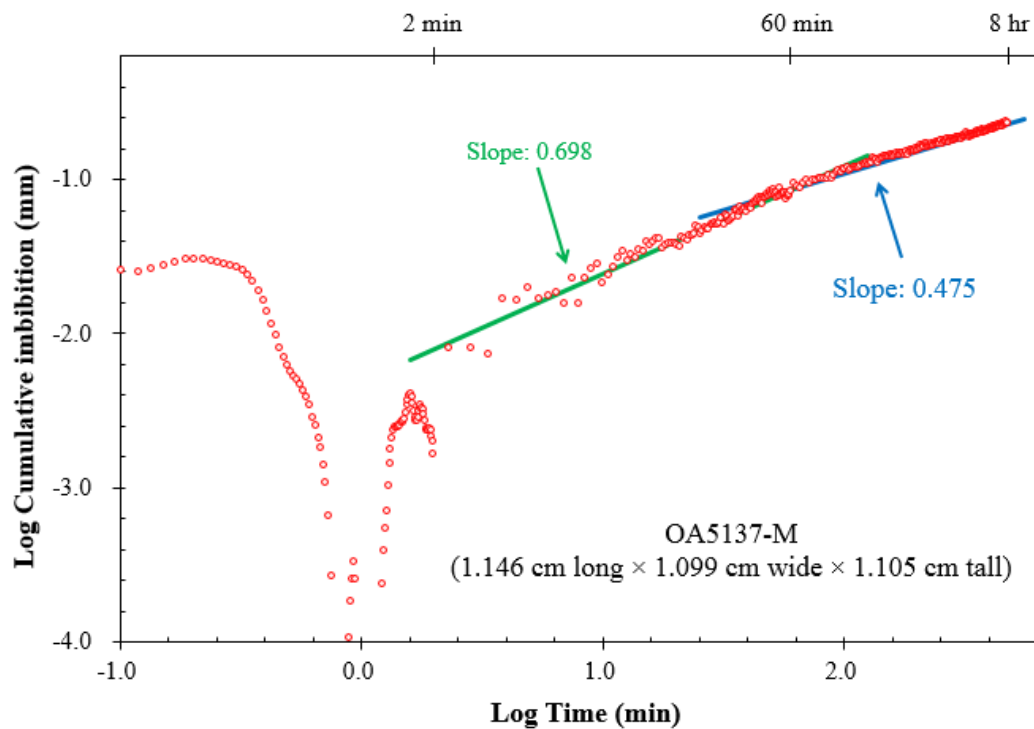


Figure 4-12 OA5137-M n-decane imbibition results.

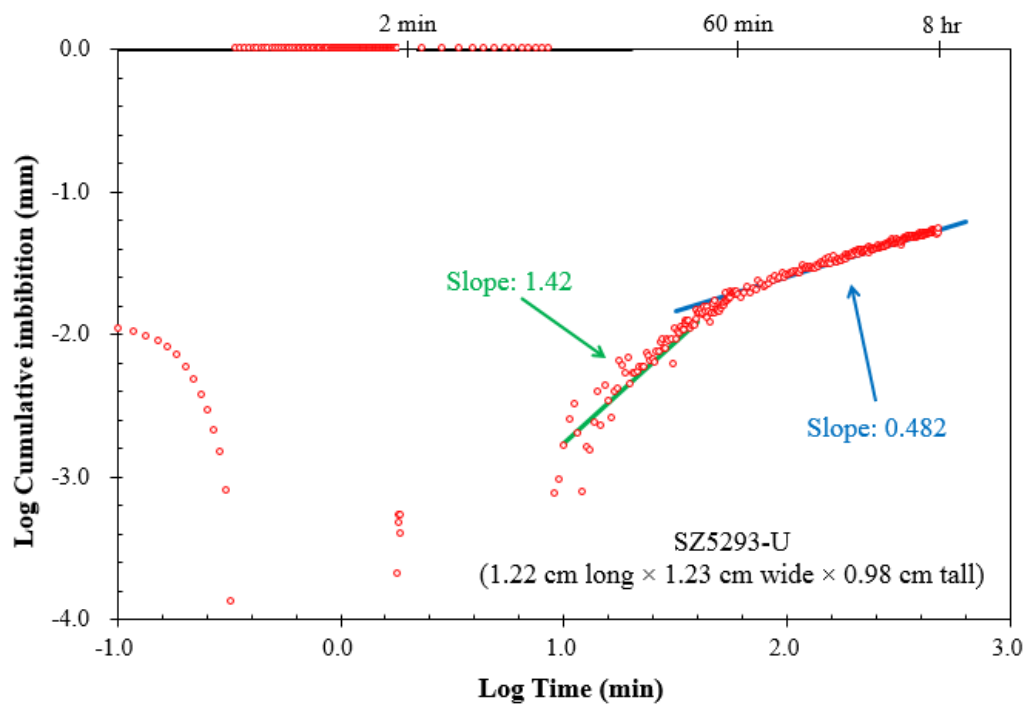


Figure 4-13 SZ5293-U n-decane imbibition results.

4-6 Low Pressure Gas Physisorption Results

All three Mancos samples were subjected to low-pressure gas physisorption tests. From these tests, isotherm profiles were developed. In 1985, IUPAC developed a system characterizing the common pore sizes associated with particular adsorption and desorption curve shapes. From this scientifically accepted method, tested samples display adsorption curves resembling Type II isotherms (Figures 4-14, 4-15, 4-16). Type II isotherms usually correspond to non-porous or macroporous samples (Sing, 1985). Macroporous materials refer to pore throats greater than 50 nm. However, the desorption curves obtained from tested samples resemble a type H3 hysteresis loop. This curve is associated with slit-shaped, or mesopore sized pores usually ranging from 2-50 nm (Sing, 1985). Rouquerol (1998) refers to this phenomena as a Type IIB isotherm profile. Therefore, Mancos Shale samples were found to contain both mesopores and macropores.

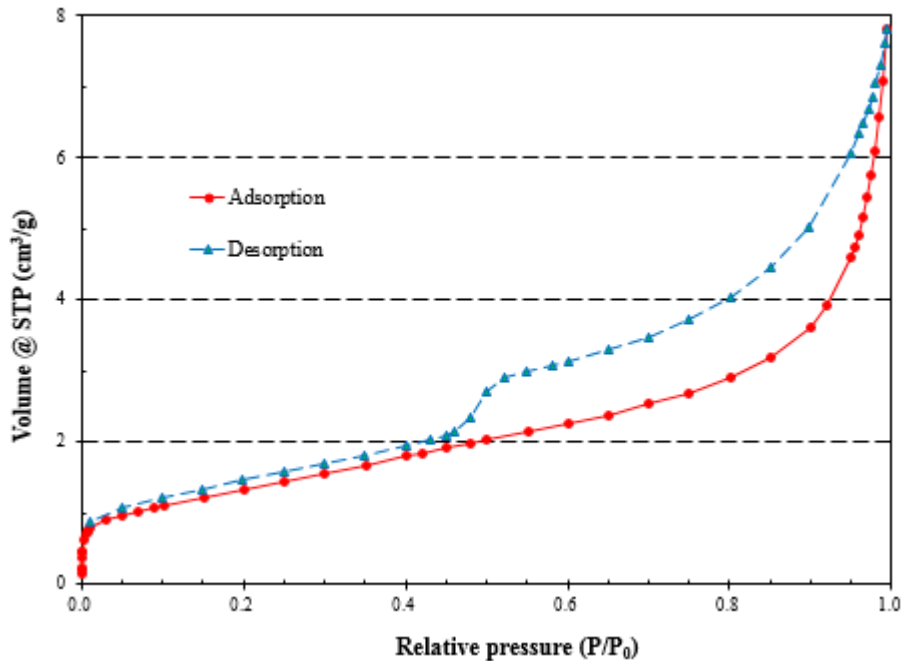


Figure 4-14 Nitrogen Sorption Isotherm of JW4892-L.

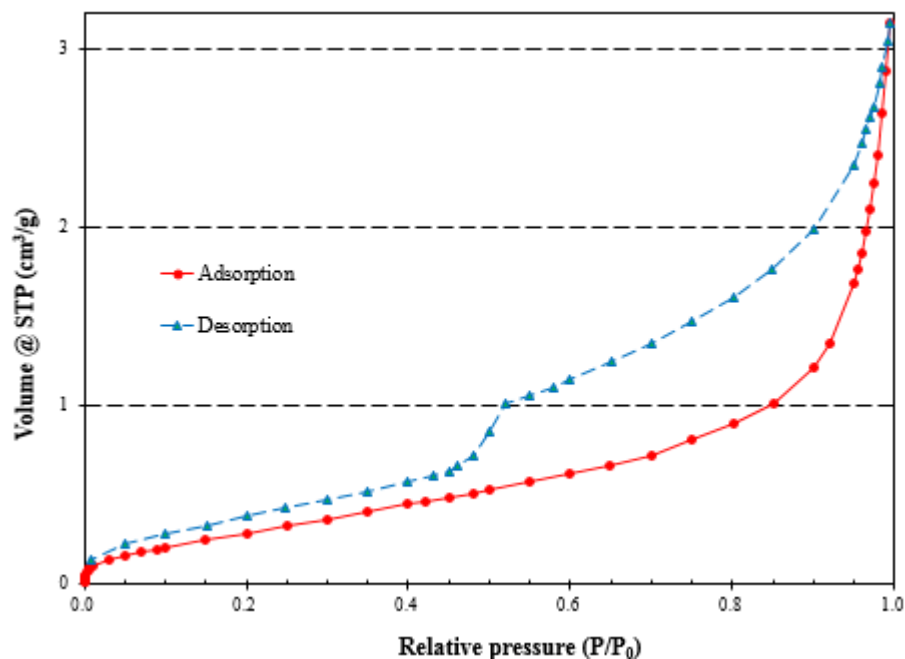


Figure 4-15 Nitrogen Sorption Isotherm of OA5137-M.

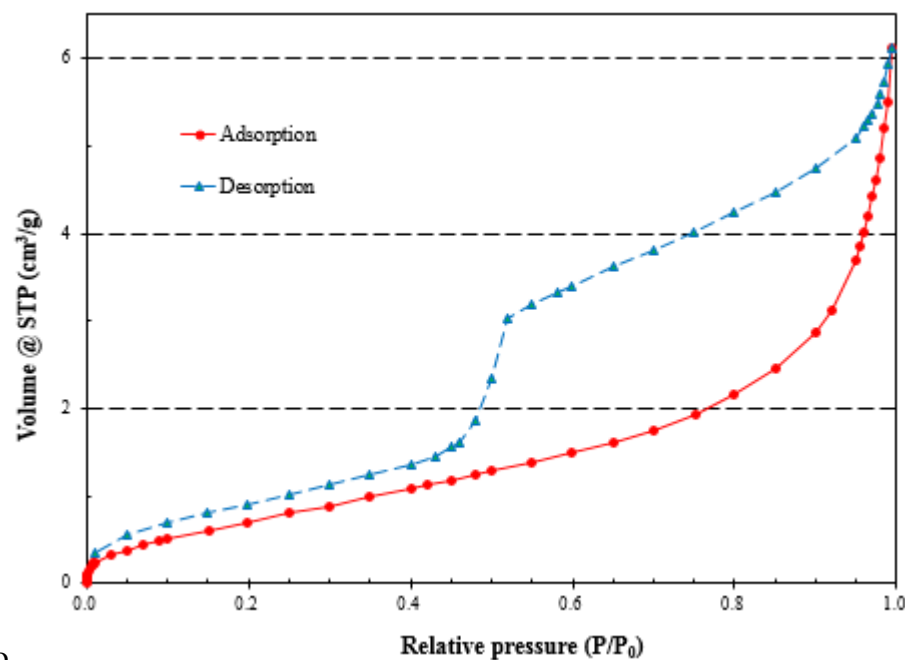


Figure 4-16 Nitrogen Sorption Isotherm of SZ5293-U.

Low-pressure gas physisorption tests using the DFT method were performed on all three samples and measures pore sizes up to roughly 35 nm. To simplify the quantitative assessment of pore size distribution, pore throats are divided into specific width ranges, as displayed in Table 8.

Both Tocito samples, JW4892-L and OA5137-M, show very similar results with the largest difference in any of the pore widths being 6.86% in the 5-10 nm pore width range. JW4892-L was the only sample containing micropores (<2 nm). The Offshore Mancos sample, SZ5293-U, contains a substantial amount of pores in the 10-36 nm range, compared to Tocito samples. Results are graphically displayed in Figure 4-17.

Table 8 Pore size distribution (%) using DFT method.

Sample	Pore Size (nm)			
	0.5-2	2-5	5-10	10-36
JW4892-L	6.73	32.07	22.17	39.03
OA5137-M	0.00	33.92	29.03	37.05
SZ5293-U	0.00	56.22	24.61	19.17

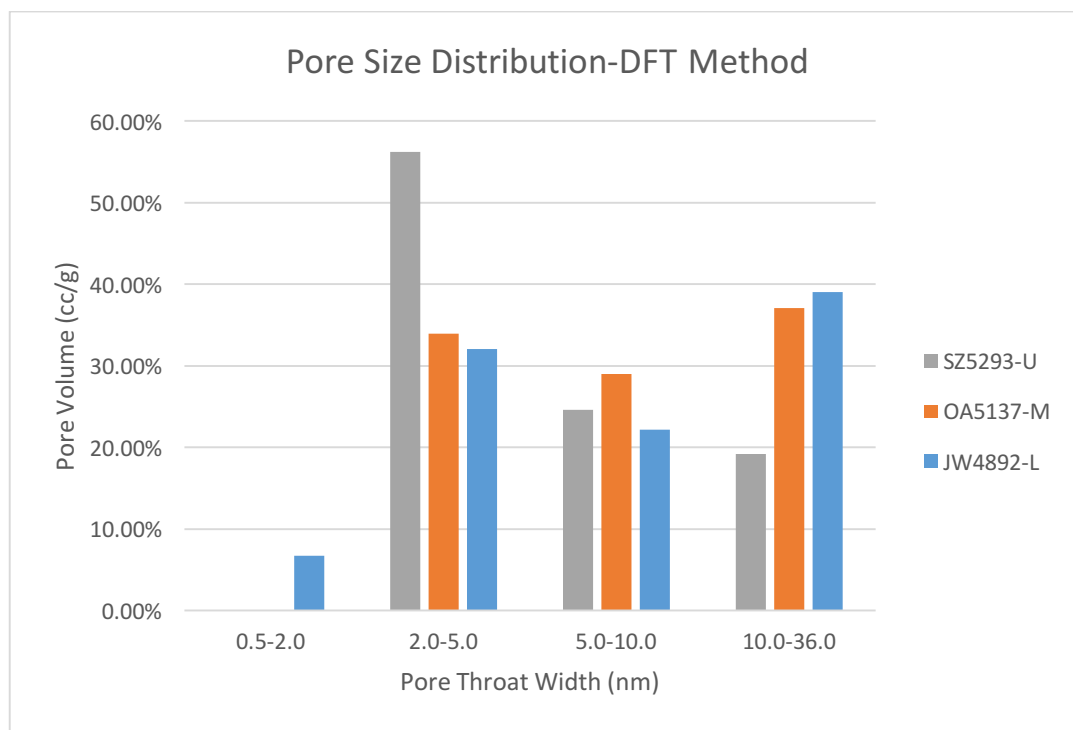


Figure 4-17 Graphical representation of pore size distribution obtained from nitrogen physisorption tests using DFT method.

The BJH method was also used to quantify pore size distribution, and has the ability to detect larger pore throats. The largest pore throats detected during testing of all samples was roughly 288 nm. Results are displayed in Table 9. Adsorption and desorption data show relatively similar results between samples, with the largest discrepancies coming from sample SZ5293-U in the 5-10 nm range and sample JW4892-L in the 0.5-2 nm range. Sample JW4892-L displays the largest amount of micropores out of the three samples, similar to results obtained from the DFT method.

Table 9 Pore size distribution (%) of pore widths (nm) obtained from nitrogen gas physisorption using BJH method on adsorption and desorption results.

Test	Sample	0.5-2 nm	2-5 nm	5-10 nm	10-50 nm	50-100 nm	100-300 nm
BJH Adsorption	JW4892-L	12.64	17.52	9.78	22.37	19.55	18.14
	OA5137-M	1.60	10.38	8.29	26.55	26.74	26.44
	SZ5293-U	2.02	12.36	9.49	27.62	25.23	23.28
BJH Desorption	JW4892-L	0.17	12.54	14.78	21.55	27.62	23.34
	OA5137-M	0.05	9.96	15.98	22.26	27.96	23.79
	SZ5293-U	0.00	12.46	20.87	22.13	24.58	19.97

Figures 4-18, 4-19, and 4-20 graphically display cumulative (V) and incremental (dV) pore volumes associated with their respective pore throat sizes. Spikes in incremental pore volume represent the most dominant pore widths. Accordingly, in sample JW4892-L, the largest amount of pore widths range from 1.3-1.7 nm and 3.0-5.0 nm (Figure 4-18). Pore widths larger than 5 nm are relatively evenly distributed, as is witnessed by a shallow decrease in incremental pore volume. Sample OA5137-M display very similar results as those found in JW4892-L, with the dominant pore widths ranging from 3.0-5.0 nm and dispersing evenly after that (Figure 4-19). Sample SZ5293-U only contains one incremental pore volume spike, in the 3.0-5.0 range (Figure

4-20). However, unlike the Tocito samples, the incremental pore volume decreases sharply following pore widths larger than 5 nm. This phenomena indicates that a very large majority of pores widths lie within the 3.0-5.0 range. This is supported by the data displayed in Table 9.

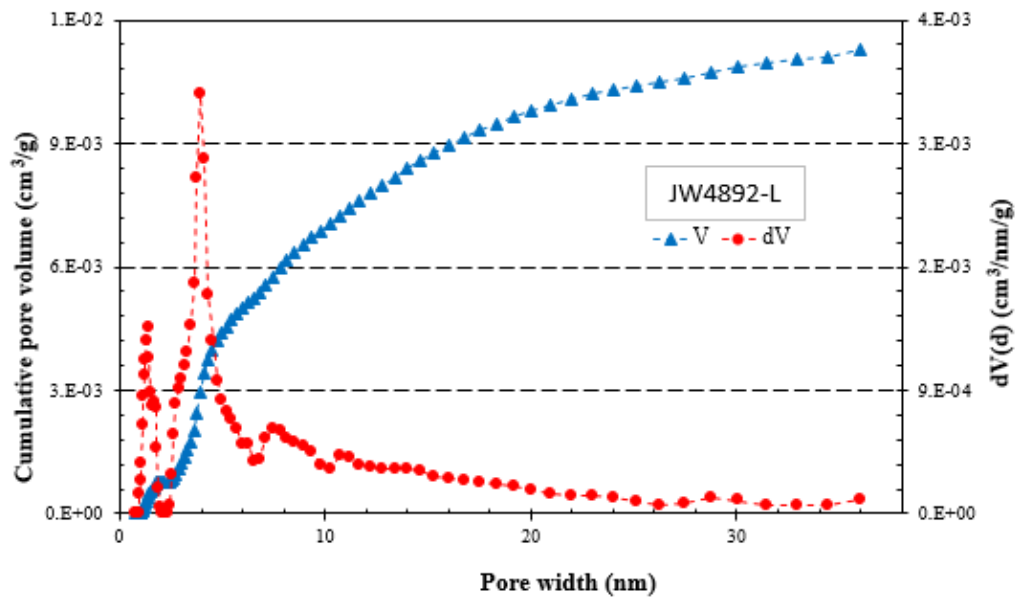


Figure 4-18 Cumulative and incremental pore volume of JW4892-L displayed.

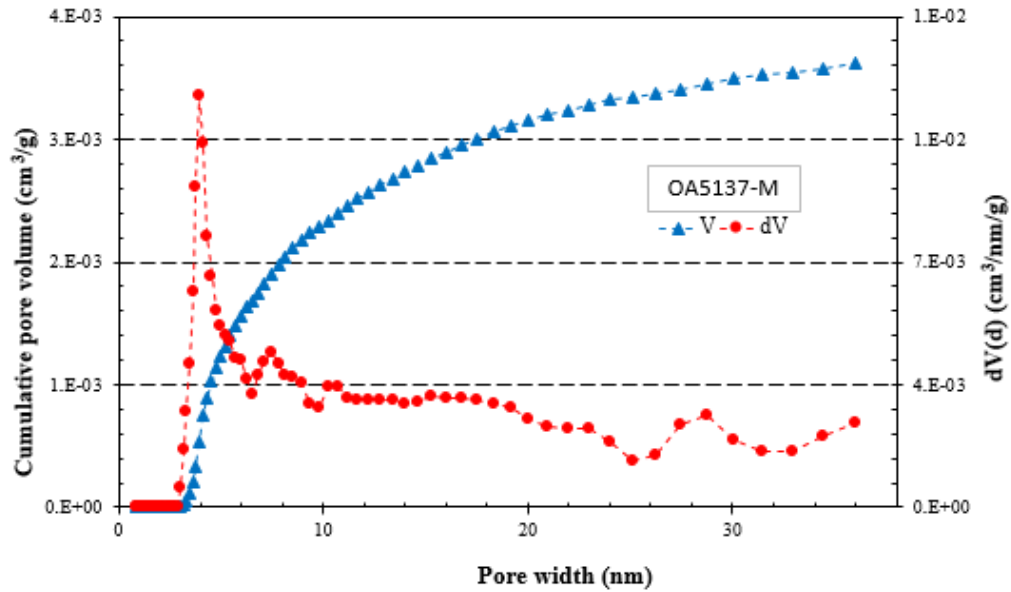


Figure 4-19 Cumulative and incremental pore volume of OA5137-M displayed.

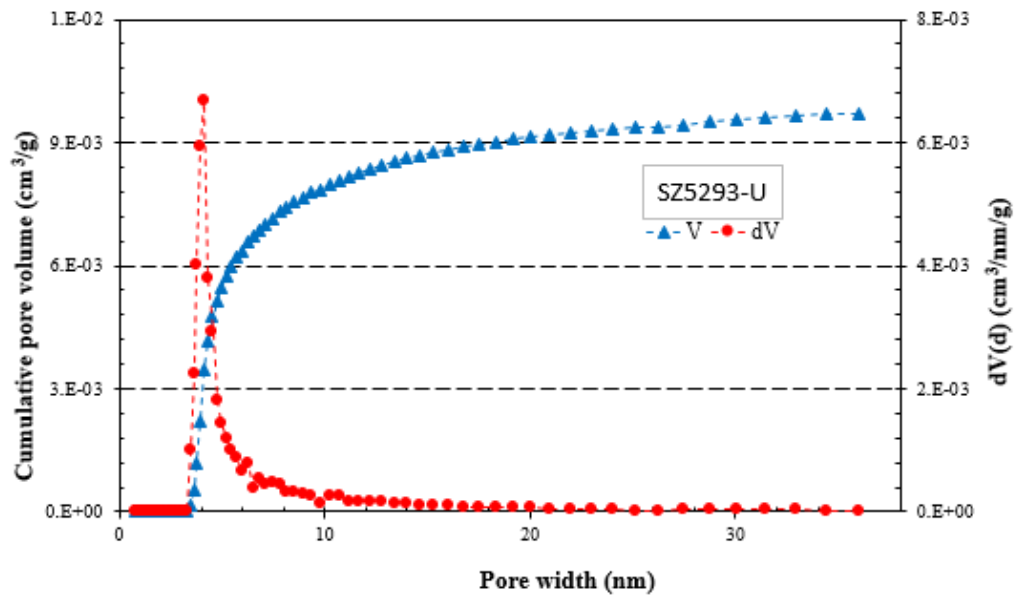


Figure 4-20 Cumulative and incremental pore volume of SZ5293-U displayed.

4-7 MICP

MICP was run on samples JW4892-L and OA5137-M and provides a diverse amount of data both directly and indirectly. MICP directly provides porosity and pore-throat size

distribution and indirectly measures permeability and tortuosity, among others. In order to determine pore-throat size distribution, Gao and Hu (2013) express the need to pick inflection points. Inflection points represent the point at which mercury intruding the pore throat has exceeded the capillary pressure of a specific connected pore network. Figure 4-21 displays an example of inflection points picked for one of the samples. Main inflection points are then used to determine permeability and tortuosity. JW4892-L exhibits the largest permeability, with 50.97 nD and OA5137-M with 8.01 nD (Table 10). Permeability is represented as a harmonic mean of values obtained from each observed inflection point. Porosity obtained from MICP has JW4892-L to be 5.55%, and OA5137-M 2.15%. With respect to helium porosity obtained from core plugs, results are relatively similar to that of MICP. Bulk density of samples range from 2.49-2.53 g/cm³. Guodong et al. (2015) performed helium porosity on core plugs perpendicular to bedding as well and can be found in Table 11.

Table 10 Results obtained through MICP of Tocito samples, JW4892-L and OA5137-M.

	JW4892-L	OA5137-M	SZ5293-U
Bulk Density (g/cm³)	2.49	2.53	2.44
Skeletal density (g/cm³)	2.64	2.58	2.47
Porosity (%)	5.55	2.15	1.15
Total pore area (m²/g)	5.38	3.35	4.87
Total pore volume (mm³/g)	0.022	0.009	0.005
Median pore-throat diameter (nm) Volume	30.8	12.1	4.6
Median pore-throat diameter (nm) Area	7.2	5.5	4.5
Median pore-throat diameter (nm) 4V/A	16.6	10.1	3.9
Permeability (nD)	51.0	8.01	N/A
Tortuosity	3.83	4.24	N/A
Mercury Entrapment (%)	48.07	40.20	N/A

Table 11 Porosity results obtained from various methods including MICP and helium pycnometry, as well as helium porosity conducted by Guodong et al. (2015).

Sample	Method	Porosity
JW4892-L	Helium Porosity- Parallel	7.14
JW4892-L	Helium Porosity- Transverse	4.54
JW4892-L	MICP	5.55
OA5137-M	Helium Porosity- Parallel	1.96
OA5137-M	Helium Porosity- Transverse	1.77
OA5137-M	MICP	2.15
SZ5293-U	MICP	1.15
MN1H	Helium Porosity- Transverse	4.56
MN1H a	Helium Porosity- Transverse	5.69
MN1H a1	Helium Porosity- Transverse	6.27

In order to better understand the pore size distribution of tested samples, pore throats were divided into ranges similar to nitrogen physisorption tests, except MICP has the ability to measure larger pore throat widths up to 50 μm . Pore throat width ranges and their associated numerical percentages are displayed in Table 12.

Pore throat types and associated predominant pore types:

- 2.8-5 nm: Inter-clay platelet pore space
- 5-10 nm: Organic pores
- 10-50 nm: Intragranular pore space
- 0.05-1 μm : Intergranular pore space
- 1-50 μm : Micro-fractures or lamination

Sample JW4892-L displays a bimodal distribution of pore throat sizes, with the largest percentage of pores falling in the intragranular pore throat range (Figure 4-22). Intergranular

pores account for approximately 36%, while remaining pore types are distributed relatively evenly. The largest percentage of pores in sample OA5137-M were found to be organic to intragranular, accounting for roughly 29% and 33%, respectively. Both samples exhibit relatively low amounts of pores in the 2.8-5 nm and micro-fracture range. As a whole, OA5137-M tends to display a larger amount of smaller pore throat widths (inter-clay platelet and OM-hosted pores) compared to JW4892-L. Conversely, JW4892-L contains a larger amount of larger pore widths (intragranular and intergranular pores) than OA5137-M. Intrusion and extrusion curves are displayed in Figure 4-23, and show that roughly 48.1% and 40.2% of mercury remains in samples JW4892-L and OA5137, respectively.

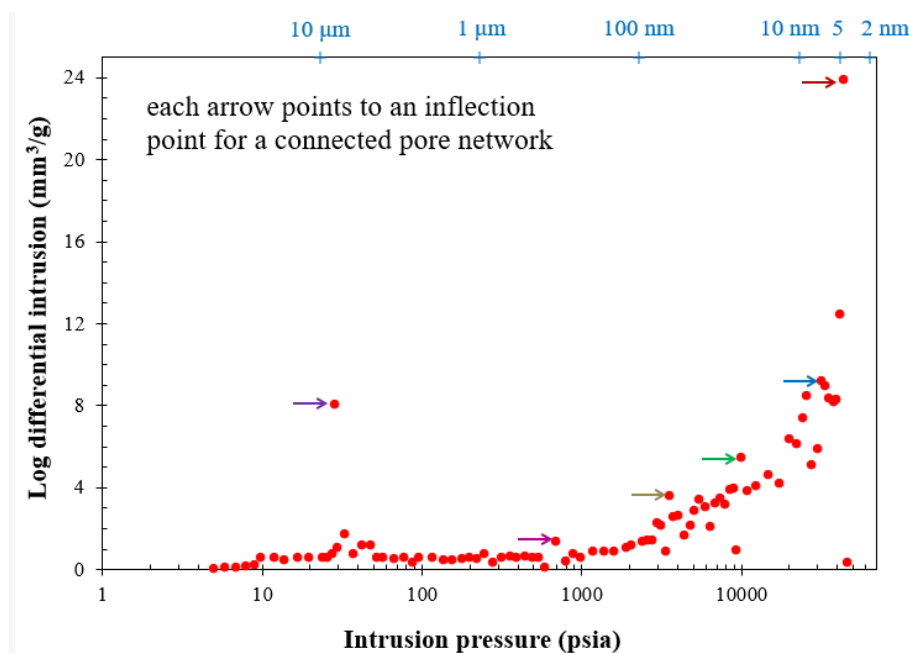


Figure 4-21 Example of inflection points picked for sample OA5137-M.

Table 12 Pore size distribution percentages by pore width ranges.

Sample ID	0.0028- 0.005 μm	0.005- 0.01 μm	0.01- 0.05 μm	0.05- 0.1 μm	0.1-1 μm	1-10 μm	10-50 μm
JW4892-L	5.798	9.70	42.322	16.580	19.128	4.288	2.183
OA5137-M	9.469	28.7	33.267	7.283	8.914	9.288	3.104

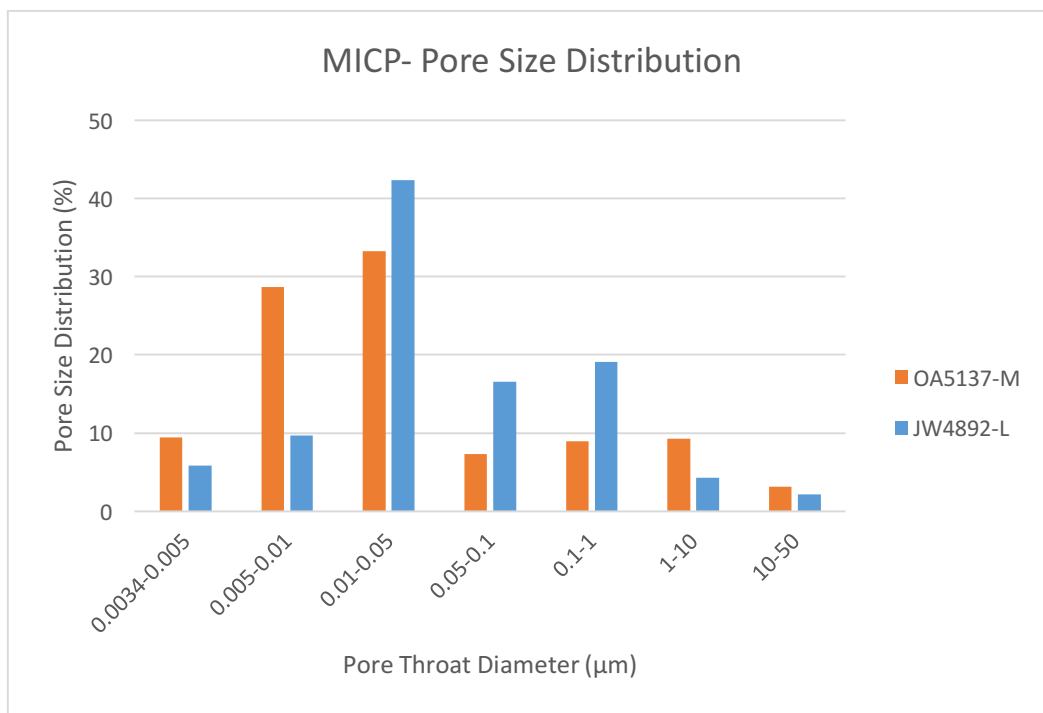


Figure 4-22 Pore size distribution obtained from MICP of Tocito samples, JW4892-L and OA5137-M.

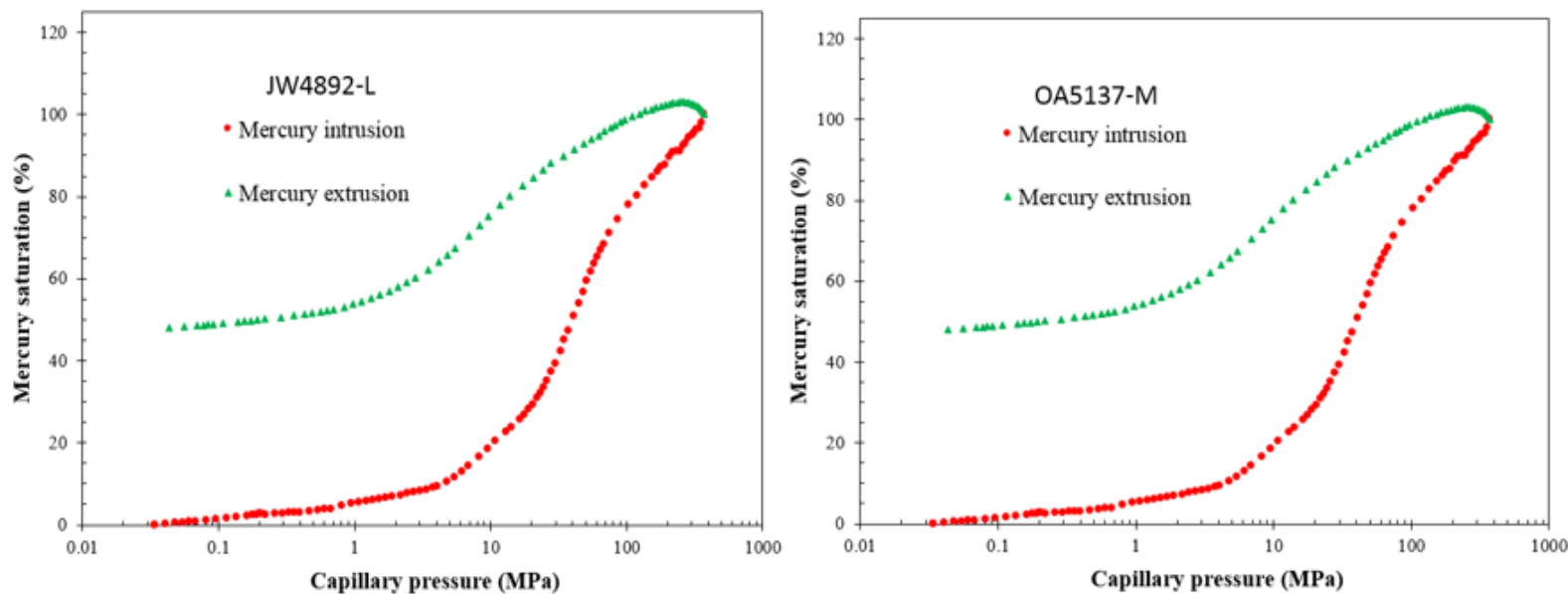


Figure 4-23 Intrusion and extrusion curves obtained from MICP tests of Tocito Marine Bar samples.

4-8 Production Data

Production data from the wells where samples were chosen from was obtained from DrillingInfo (Table 13). Scout cards indicate the wells target the “Gallup” formation. Sample JW4892-L was cored from the Joan White #2 well, located in the Tocito Marine Bar play. The well began producing on January 1, 1959 and was plugged and abandoned on September 1, 1968. The well produced approximately 76,432 barrels of oil and 208,523 cubic feet of natural gas. Sample OA5137-M was cored from the Ojo Amarillo #5 well, located in the Tocito Marine Bar play. The well began producing on January 1, 1972 and was plugged and abandoned on January 1, 1986. The well produced approximately 64,697 barrels of oil and 208,523 cubic feet of natural gas. Sample SZ5293-U was cored from the Sanchez #2 well, located in the Offshore Mancos play. The well began producing on June 1, 1984 and was plugged and abandoned on

March 1, 1986. The well produced approximately 76,432 barrels of oil and 208,523 cubic feet of natural gas.

Table 13 Production data of selected wells (Drilling Info, 2017). Blue is Offshore Mancos Play and Yellow is Tocito Marine Bar Play.

Well	County	Field	Play Name	Formation	Cum. Oil (BBL)	Cum. Gas (MCF)	Status
Sanchez 2	San Juan	Armenta	Offshore Mancos Play	Gallup	4,749	61,744	Plugged & Abandoned
Joan White 2	San Juan	Bisti	Tocito Marine Bar Play	Gallup	76,432	208,523	Plugged & Abandoned
Ojo Amarillo 5	San Juan	Cha Cha	Tocito Marine Bar Play	Gallup	64,697	3,784	Plugged & Abandoned

Chapter 5 Discussion

5-1 Mineralogy

Both JW4892-L and OA5137-M samples are located within the more sand-rich, Tocito marine bar play, and therefore display larger amounts of quartz. The main difference between Tocito and Offshore samples is calcite content. Sample SZ5293-U contains roughly 3.5x more calcite than samples JW4892-L and OA5137-M. This could be explained by its more northeastern location relative to the other samples, as carbonate content tends to increase to the northeast region of the San Juan Basin (Figure 5-1). Sandstones, or more silica-rich facies are more commonplace in the southwest region of the basin.

Along with calcite, ankerite is a common cementing mineral of sandstones and siltstones in the more eastern, Offshore Mancos play region of the basin (Emmendorfer, 1992). Ankerite is a type of dolomite that forms from tectonic fracturing. Ankerite is similar to dolomite, but magnesium is replaced by iron and manganese. Once tectonic fracturing occurs, ankerite forms due to metasomatic replacement of calcite as long as magnesium is present (Emmendorfer, 1989). These rocks are commonly referred to as tectonic dolomites, and have been linked to prolific oil production. Sulphides such as pyrite and marcasite are also commonly associated with tectonic dolomite. Where once thought that natural fractures formed after dolomitization, London (1972) determined that dolomite formed as a result of natural fracturing. Due to the close association between dolomites and natural fractures, a large presence of dolomite can potentially indicate a presence of hydrocarbons.

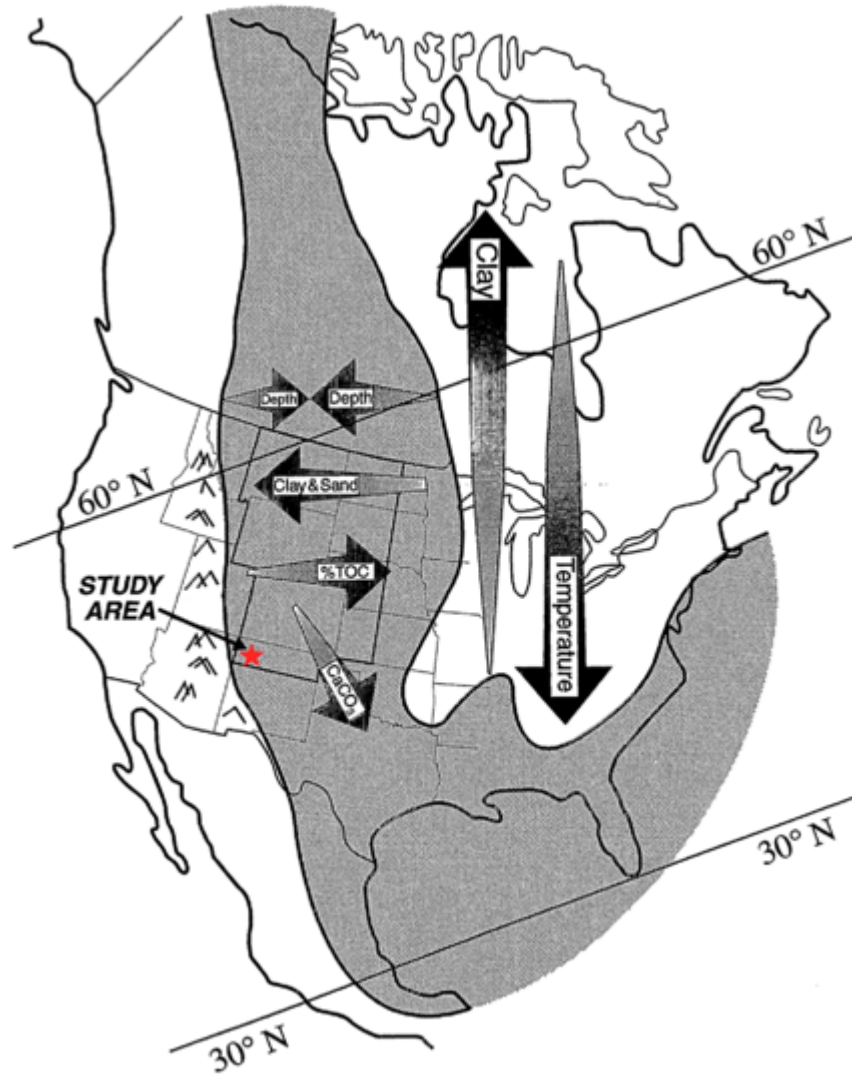


Figure 5-1 Modified from “Nature and Distribution of Niobrara Lithologies in the Cretaceous Western Interior Seaway (Longman, Luneau, Landon 1998).

5-2 Wetting Characteristics and Spontaneous Imbibition

The fluid that occupies the outside space of the pore and is in contact with the rock surface is referred to as the wetting fluid. Generally speaking, sandstone reservoirs are usually water wet. This means that oil molecules are at the center of the pores and water molecules are on the outside of the pores in contact with the sand grains. Limestones and dolomites are usually oil wet since oil coats the rock surface. As a general rule concerning wettability, fluids in the

center of the pore will flow easier than fluids on the outside of the pore being held to the rock by surface tension. Ultimately, a better understanding of the wettability characteristics of a reservoir will lead to greater hydrocarbon recovery. Issues can arise when assessing the wetting characteristics of mudrocks, since their lithologies can vary both laterally and vertically. Morsy et al. (2014) found that by altering fluids used for imbibition tests on the Mancos Shale, wetting characteristics could be manipulated, thus enhancing oil recovery.

The low n-decane contact angles obtained from samples during contact angle measurement demonstrate the sample's hydrophobic relationship with n-decane, as the fluid is readily absorbed by the rock. It is also important to note the short amount of time in which the sample absorbed n-decane. Low contact angles coupled with quick absorption rates demonstrate that sample surfaces are preferentially oil wet. However, contact angles obtained from non-decane fluids (API brine, 20% IPA, and DI water) indicate mixed wettability of the samples. Although convenient to describe a rock as having purely water or oil wet behaviors, the lithological heterogeneity of most, if not all reservoirs is expected to produce a mixed wettability of some sort.

Spontaneous imbibition can help determine if the pore network of the tested samples are well connected. With respect to DI water, Stage II slopes demonstrate a rather poorly connected pore network. Contact angle results support this conclusion. Yang et al. (2017) notes that the swelling of clays and subsequent microfracture formation can lead to larger connectivity slopes. Not including mica in total clay content of samples, larger connectivity slopes are witnessed in more clay-rich samples. With respect to n-decane, results indicate a well-connected pore network. Oil is preferably imbibed into the sample, due to the hydrophobic relationship between organic pores within the pore network and oil. Imbibition results are supported by results

obtained from contact angle tests. With respect to n-decane, the presence of very low contact angle show that oil spreads readily on the sample surface. This behavior suggests the sample's preference to oil. Overall, results demonstrate samples are oil-wet to mixed-wet, with a tendency of pore networks to imbibe oil over water.

5-3 Porosity and Permeability

Porosity is an important component of unconventional reservoirs as it plays a large role in the storage capacity of hydrocarbons. Porosity was measured on samples using a variety of methods (Table 14). Helium porosity results from core plugs of JW4892-L and OA5137-M range from 1.77 to 7.14%. No direct relationship is witnessed between measurements taken in the transverse and parallel direction. Helium porosity results conducted by Guodong et al., 2015 show a range of 4.56 to 6.27%, falling in the range of JW4892-L and OA5137-M. Porosity from MICP show similar results. JW4892-L shows the highest porosity among tested samples, further validating helium porosity results. MICP porosity of OA5137-M is slightly larger than helium porosity results, but not enough to raise concern over the validity of both tests. Porosity results from Sperandino (1983) indicate display similar results to other testing methods, with a range of 1 to 4%.

Table 14 Porosity measurement from different methods

Sample ID	Porosity				
	Core plug Helium Porosity (%) (P)	Core plug Helium Porosity (%) (T)	Core plug Helium Porosity (%) (T) (Guodong et al., 2015)	MICP porosity (%)	Porosity (%) (Sperandino, R.J., 1983)
JW4892-L	7.14	4.54	-	5.55	1-4
OA5137-M	1.96	1.77	-	2.15	
SZ5293-U	-	-	-	1.15	
MN1H	-	-	4.56	-	
MN1H a	-	-	5.69	-	
MN1H a1	-	-	6.27	-	

Permeability is another critical component of unconventional reservoirs as it plays a contributing role in the flow of hydrocarbons from the rock matrix to the wellbore. Permeability was measured on samples using a variety of methods (Table 15). As one would expect, core plug results parallel to lamination were larger than results transverse to lamination in sample JW4892-L. However, sample OA5137-M shows a different phenomena. Permeability almost triples from 3,000 to 10,000 nD. In order compare core plug results to MICP, a geometric mean of the first three inflection points from MICP are taken. This is done to account for the low confining pressures associated with core plug tests, since the first three inflection points from MICP are in relatively low pressure settings. Results show similar results among tested samples further validating both testing methods. MICP results range from 1,114 to 5,747 nD compared to core plug ranges of 3,000 to 10,000 nD. Permeability results obtained by Sperandino (1983) do not suggest any specific relationships between methods since no testing method was given, but do

encompass the values acquired from other methods. As mentioned earlier, permeability can be predicted from n-decane imbibition if there is good connectivity. Imbibition permeability results are the lowest among all methods and range from 10.1 to 144,317 nD. Differences between the different methods used to measure permeability could be due to sample size.

Table 15 Permeability measurements from different methods

Sample ID	Permeability				
	Core Plug K Air (P) (nD)	Core Plug K Air (T) (nD)	MICP Permeability (nD)	Permeability (nD) Sperandino, R.J., 1983)	Imbibition Predicted k (nD)
JW4892-L	5,000	4,000	5,747	< 400,000	144,317
OA5137-M	3,000	10,000	1,114		389
SZ5293-U	-	-	-		10.1

5-4 Pore Size Distribution

A negative correlation exists between TOC and porosity among the three samples. As porosity increases, TOC decreases (Figure 5-2). Since organic matter hosted pores are known to contribute a large amount to total porosity in organic rich shales, it is important to explain this anomaly. One explanation could be that the organic matter is not porous, or that something else has already filled the organic pores (e.g. cement or migrated bitumen). Löhr et al. (2015) found that Woodford Shale organic matter pores occurred only in immature and gas-mature samples. Organic matter pores were not found in oil-mature samples due to the infilling of bitumen. Although the Woodford has different petrophysical characteristics than the Mancos, this could explain the negative correlation between TOC and porosity since the tested Mancos samples are oil-mature. In addition, porosity can be strongly related to grain size and mineralogy.

A strong correlation exists with maturity and depth (Figure 5-3), as well as maturity and location within the basin. Maturation increases towards the eastern side of the basin, where the

Mancos is deposited at increased depths. This is supported by Broadhead's (2013) findings. In the western portion of the basin, the Mancos enters the upper portion of the oil window, including the Tocito Marine Bar play. Further east of the play, the Mancos finds itself in the more mature, lower portion of the oil window. Further east of that, the Mancos enters the thermogenic gas window, but samples were not collected in these locations.

An inverse relationship exists between porosity and depth of tested samples (Figure 5-4). As depth increases, porosity decreases. This is most likely due to the weight of the overburden rock and its associated compactional forces. Accordingly, samples containing more quartz, or more rigid grains resistant to compaction, display larger porosities. The more siliceous Tocito Marine Bar play samples JW4892-L and OA5137-M display larger porosities than sample SZ5293-U. With respect to porosity, MICP values were greater than helium porosity values transverse to lamination. Surface area of samples may play a role in the differences observed in porosity, as different factors are introduced including bedding planes and fractures. Helium porosity parallel to lamination was found to be larger than helium porosity transverse to lamination, indicating that bedding planes may enhance or play a role in porosity.

In order for OM pores to develop, Dow (1977) found that thermal maturity must reach at least 0.6%. OA5137-M is more a mature mudstone than JW4892-L, with a maturity of 0.69 compared to 0.63. Subsequently, OA5137-M contains more organic matter hosted pores as determined by MICP and low pressure nitrogen physisorption tests (BJH Desorption). BJH Adsorption results were the only results to show less organic matter hosted pores in sample OA5137-M compared to JW4892-L. Stage II imbibition slopes with respect to n-decane are larger in sample OA5137-M compared to JW4892-L, corresponding with the hydrophobic relationship between organic matter and n-decane. Since MICP was not performed on SZ5293-

U, comparisons are unable to be made with certainty between all samples. However, pore size distributions obtained from nitrogen physisorption tests help bridge the gap.

The higher thermal maturity of SZ5293-U would suggest a larger percentage of OM pores, relative to other samples. BJH Desorption results mirror this relationship, but BJH Adsorption and DFT results differ. However, the main difference between samples with respect to nitrogen physisorption tests, lies with sample SZ5293-U and DFT results. Sample SZ5293-U displayed a significantly less amount of pore throats in the 10-36 nm range compared to Tocito samples. This is most likely due to the large carbonate presence in sample SZ5293-U.

Another occurrence to note is the presence of intraparticle pores (0.1-0.05 μm). According to Loucks et al. (2012), intraparticle pores are commonly associated with pyrite framboids. Intraparticle pores account for roughly 42% and 33% of pore throat widths for samples JW4892-L and OA5137-M respectively, and all contain minor amounts of pyrite. As a whole, Tocito Marine Bar play samples are primarily controlled by OM, intraparticle and interparticle pores, with little influence from inter-clay platelet pores and microfractures or laminations. OA5137-M contains more influence from OM pores than JW4892-L, corresponding with a higher thermal maturity as well as total organic carbon content. As a whole, total porosity appears to be influenced by intraparticle pores.

Although SZ5293-U was not subject to MICP tests, nitrogen physisorption tests using the DFT method display a significantly larger amount of inter-clay platelet related pores than Tocito Marine Bar play samples. The DFT method has the ability to analyze smaller pore throats compared to other nitrogen physisorption methods, and when taking a look at inter-clay platelet pores, is the preferred method. Kuila (2012) and Villegas (2016) found that clay, specifically illite, play a large role in the distribution of inter-clay platelet pore throats. Illite was detected in

2 of the 3 samples tested, and appears to play a significant role in the formation of inter-clay platelet pores similar to the findings of Kuila and Villegas (Table 16). Porosity also displays an inverse relationship with Illite %. The larger amount of Illite, the smaller the porosity of the sample. As rocks are buried, clays have the tendency to become more ductile. The more ductile clays become, the higher the chance that intergranular pores are sealed, decreasing the porosity of the sample.

Extrusion curves (Figure 4-23) from MICP show that approximately 48.1% and 40.2% of mercury remain in samples JW4892-L and OA5137-M respectively. This illustrates the complex nature of the sample's pore networks. Mercury is unable to efficiently exit the sample without external pressure due to what Hu et al. (2017) describes as ink bottle pores, where large pore bodies are connected by smaller pore throats.

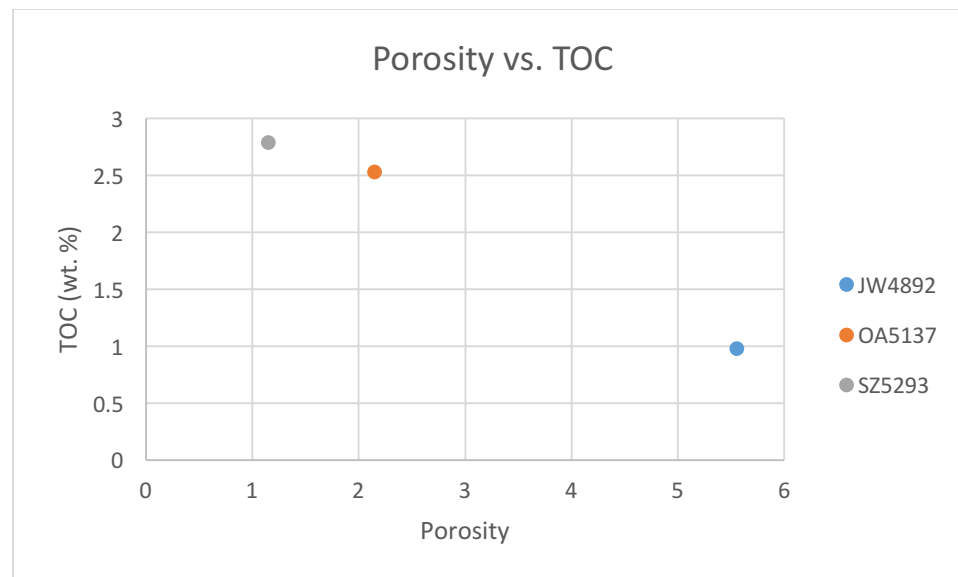


Figure 5-2 Relationship between porosity and TOC in samples.

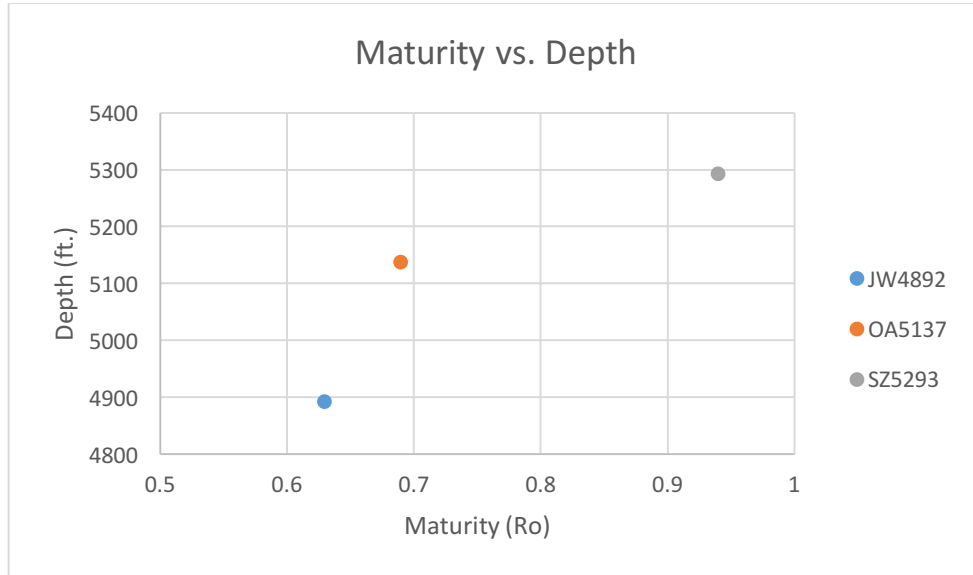


Figure 5-3 Relationship between maturity and depth of samples.

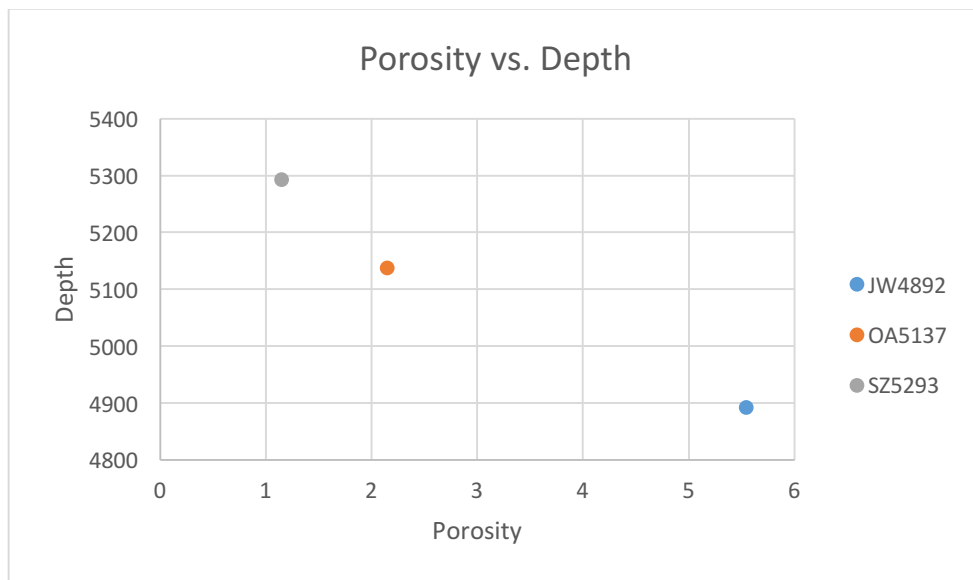


Figure 5-4 Relationship between porosity and depth of samples.

Table 16 Porosity and illite percentage compared to inter-clay platelet pore percentages for both MICP (2.8-5 nm) and nitrogen physisorption DFT method (0.5-5 nm).

Sample	Porosity	Illite (%)	DFT Method (%)	MICP (%)
JW4892-L	5.55	0.2	38.8	5.80
OA5137-M	2.15	-	33.9	9.50
SZ5293-U	1.15	2.7	56.7	

Chapter 6 Conclusion and Recommendations

6-1 Conclusions

Samples from two separate plays of the Mancos Shale in the San Juan Basin, containing different mineralogical and petrophysical characteristics, were studied to take a look at their respective pore systems. The findings from the study are summarized below:

- Tocito Marine Bar samples are more silica-rich, consisting of mixed mudstones and mixed siliceous mudstones.
- Offshore Mancos samples are more carbonate rich, consisting of mixed mudstones, mixed siliceous mudstones, and carbonate/siliceous mudstones.
- Maturity of samples increase towards deeper, more eastern region of the San Juan Basin
- From fluid imbibition in conjunction with contact angle tests, pore connectivity is low for water, and relatively good for oil simulating fluids (n-decane)
- Samples demonstrate oil-wet to mixed-wetting characteristics
- Tocito and Offshore samples consist primarily of mesopores and macropores, with minor influence of micropores
- MICP and nitrogen physisorption DFT results indicate total porosity is influenced by intraparticle pores
- Illite appears to be a controlling factor on pore size distribution, specifically concerning inter-clay platelet pores

6-2 Recommendations

In order to gain a better understanding of the mineralogical and petrophysical characteristics that control pore size distribution, more samples need to be tested in order to deduce consistent patterns or trends. There are multiple Mancos Shale plays in the San Juan Basin with enormous potential. As the economics become more favorable, a better understanding of the pore network will be needed in order to maximize the potential of the play. In addition, other techniques such as field emission-SEM, used for pore typing, should be used to compliment current methods.

Appendix

Appendix A

Methods and Procedures for Geochemical Analysis at Weatherford Laboratories

Rock Sample Preparation

Samples for Total Organic Carbon (TOC) and/or Programmed Pyrolysis may each require varying levels of sample preparation. Groups of samples are evaluated as to their respective condition as received and are handled differently depending on the various types of contaminants, lithologies, and analytical objectives. Samples are not high-graded prior to grinding unless specifically instructed by the client. When necessary and as instructed, water washing may be required to remove water-based mud. Solvent washing can be utilized to remove oil-based and/or synthetic-based mud. Additional solvent extraction of the crushed rock will be necessary to completely remove the contaminating oil-based and/or synthetic-based mud. Sample picking may also be necessary to remove lost circulation material or known cavings. Samples for TOC and Programed Pyrolysis are then ground to pass through a fine mesh sieve prior to analysis.

Total Organic Carbon

Approximately 0.10 g of crushed rock is accurately weighed and then digested with concentrated hydrochloric acid to remove all carbonates form the sample. At this point, gravimetric carbonate content can be determined if requested. Following digestion, the sample is washed through a filtering apparatus, placed in a combustion crucible and dried. After drying, the sample is analyzed with a LECO Carbon Analyzer with detection limits to 0.01 weight

percent. Standards and sample duplicates are tested regularly to assure superior instrument performance.

Programmed Pyrolysis (Rock-Eval II, Rock-Eval VI, Source Rock Analyzer)

Programmed pyrolysis (Rock-Eval and SRA) is performed to assess source rock quality and thermal maturity (e.g., Peters, 1986; Peters and Casa, 1994). In programmed pyrolysis, crushed rock samples are heated in an inert environment to determine the yield of hydrocarbons and CO₂. The sample is initially held isothermally at 300°C for 3 minutes, producing the S1 peak by vaporizing the free (unbound) hydrocarbons. High S1 values indicate either large amounts of kerogen-derived bitumen (as in an active source rock) or the presence of migrated hydrocarbons. The oven then increases in temperature by 25°C/minute to a final temperature of approximately 600°C, depending on the instrument type. During this time, hydrocarbons that evolve from the sample as a function of the pyrolytic degradation of the kerogen are measured, generating the S2 peak and is proportional to the amount of hydrogen-rich kerogen in the rock. The temperature at which the S2 peak reaches a maximum, T_{\max} is a measure of the source rock maturity. Accuracy of T_{\max} is 1-3°C, depending on the instrument, program rate and sample size, but can also vary by organic matter type. T_{\max} values for samples with S2 peaks less than 0.2 mg HC/g rock are often inaccurate and should be rejected unless a definitive kerogen peak is noted from the pyrogram. Any carbon dioxide released between 300° and 390°C is also measured, generating the S3 peak, providing an assessment of the oxygen content of the rock. In addition to the standard programmed pyrolysis method, we have several additional methods available designed to provide the client with additional useful information as it relates to the geochemical nature and potential of a rock sample including but not limited to TOC quantification, Carbonate

quantification, Reservoir Oil Quality, APIR and Kerogen Kinetic analyses. A summary of analytical results from Programmed Pyrolysis follows.

Results

S1: free oil content (mg hydrocarbons per gram of rock)

S2: remaining hydrocarbon potential (mg hydrocarbons per gram of rock)

S3: organic carbon dioxide (mg CO₂ per gram of rock)

TOC: total organic carbon content (wt. %)

T_{max}: temperature at maximum evolution of S2 hydrocarbons

Ratios: hydrogen index (HI), oxygen index (OI), production index (PI), S2/S3, and S1/TOC

Appendix B

Methods and Procedures of X-Ray Diffraction Analysis at The Mineral Lab

A representative portion of each sample was ground to approximately -400 mesh in a steel swing mill, packed into a well-type plastic holder and then scanned with the diffractometer over the range, $3-61^{\circ} 2\theta$ using Cu-K α radiation. The ground samples were also prepared as oriented mounts by mixing ground sample with distilled water, drawing the mixture onto a cellulose acetate filter and then rolling the deposited material onto a glass disk. The oriented mounts were scanned over the range $2-30^{\circ}$; treated with glycol and then re-scanned over the range $2-22^{\circ}$. Analysis of oriented mounts aids in the identification of clay minerals. Estimates of mineral concentrations were made using our XRF-determined elemental compositions and the relative peak heights/areas on the XRD scans. The detection limit for an average mineral in these samples is $\sim 1-3\%$ and the analytical reproducibility is approximately equal to the square root of the amount. "Unidentified" accounts for that portion of the XRD scan which could not be resolved and a "?" indicates doubt in both mineral identification and amount.

Appendix C

Geochemical and XRD Data of Additional Mancos Samples

Table C-1: List of wells

Well Name	Well Code	API
Ojo Amarillo 2	OA 2	30-045-07927
Sapp C	SP 1 C	30-039-05198
Newsom A 20	NA3E	30-045-25753
San Juan 28-6 Unit	SJ 28-6	30-039-26140
North Kirtland Unit 1	NK 1	30-045-09404
McAdams 5	MCA 5	30-045-06188
NM Fed. 1	SFA 1	30-039-05560
Hagood G 9	H 9	30-045-07706
?	ROJ 1	?
Jicarilla Tribal 454 A1	AJ 454	30-039-23330
Joan White 2	WJ 2	30-045-05478
Frontier C 3	FC 3	30-045-06874
?	JA 12	?
Burham 1	B 1	30-045-05885
Federal 13-3 #1	F 13-3	30-045-26647
South Blanco 5	SBF 25-5	30-045-25043
Sanchez 2	S2	30-045-25620

Client ID	Depth	TOC Wt. %	S1 mg/g	S2 mg/g	S3 mg/g	Tmax	HI	OI	S1/ TOC	PI	Ro
H 9	- 5270 FT	2.79	2.06	7.57	0.64	438	271	23	74	0.21	0.72
H 9	- 5525 FT	2.18	1.57	8.65	0.48	440	397	22	72	0.15	0.76
H 9	- 5561 FT	2.54	0.37	1.88	1.06	434	74	42	15	0.16	0.65
ROJ 1	6422 - 6426 FT	0.88	0.23	1.82	0.51	434	207	58	26	0.11	0.65
ROJ 1	6426 - 6430 FT	1.01	0.11	0.84	0.47	435	83	47	11	0.12	0.67
ROJ 1	6434 - 6437 FT	0.82	0.42	0.82	0.45	481	100	55	51	0.34	1.50
AJ 454	- 7049.5 FT	2.29	0.44	0.83	0.46	481	36	20	19	0.35	1.50
AJ 454	- 7066 FT	1.67	0.38	0.6	0.55	479	36	33	23	0.39	1.46
WJ 2	4667 - 4681 FT	1.64	0.37	4.88	0.58	429	298	35	23	0.07	0.56
WJ 2	- 4816 FT	0.82	0.6	1.2	0.46	431	146	56	73	0.33	0.60
WJ 2	4866 - 4879 FT	0.9	0.23	0.94	0.46	435	105	51	26	0.2	0.67
FC 3	- 5776 FT	2.46	1.25	7.14	0.54	442	290	22	51	0.15	0.80
FC 3	- 5788.4 FT	2.72	1.07	8.78	0.48	437	323	18	39	0.11	0.71
FC 3	- 5860.5 FT	1.09	0.25	1.2	0.41	439	110	38	23	0.17	0.74
FC 3	- 5885 FT	1.51	0.41	2.36	1	439	156	66	27	0.15	0.74
JA 12	- 7034 FT	2.09	1.08	6.03	1.06	440	289	51	52	0.15	0.76
JA 12	- 7067.5 FT	2.47	1.56	8.65	0.5	438	350	20	63	0.15	0.72
JA 12	- 7123.4 FT	2.39	1.15	7.32	0.47	441	306	20	48	0.14	0.78
JA 12	- 7168.9 FT	2.38	0.85	6.93	0.5	441	291	21	36	0.11	0.78
B 1	- 4242 FT	1.53	0.79	4.13	0.65	438	270	42	52	0.16	0.72
B 1	- 4270.5 FT	1.93	0.56	2.93	0.42	441	152	22	29	0.16	0.78
B 1	- 4338 FT	2.53	1.02	9.05	0.57	437	358	23	40	0.1	0.71
B 1	- 4419.5 FT	2.03	0.32	2.77	0.35	440	136	17	16	0.1	0.76
B 1	- 4436.5 FT	3.89	0.71	7.71	0.45	441	198	12	18	0.08	0.78
F 13-3	- 5416.5 FT	1.82	0.85	7.92	0.6	433	435	33	47	0.1	0.63
F 13-3	- 5416.5 FT	1.74	0.06	5.76	0.6	436	331	34	3	0.01	0.69
F 13-3	- 5418.8 FT	1.66	0.61	6.34	0.55	435	382	33	37	0.09	0.67
F 13-3	- 5418.8 FT	1.56	0.06	4.43	0.65	436	284	42	4	0.01	0.69
F 13-3	- 5419.5 FT	1.9	0.66	7.58	0.45	437	399	24	35	0.08	0.71
F 13-3	- 5419.5 FT	1.82	0.07	5.39	0.59	436	296	32	4	0.01	0.69
F 13-3	- 5421.5 FT	2.69	0.66	13.76	0.41	436	512	15	25	0.05	0.69
F 13-3	- 5421.5 FT	2.62	0.06	11.06	0.62	432	422	24	2	0.01	0.62
F 13-3	- 5423 FT	1.37	0.29	4.27	0.37	434	312	27	21	0.06	0.65
F 13-3	- 5424.5 FT	1.65	0.6	5.89	0.28	435	357	17	36	0.09	0.67
F 13-3	- 5424.5 FT	1.35	0.04	4.11	0.4	435	304	30	3	0.01	0.67
F 13-3	- 5430.7 FT	0.44	0.88	1.38	0.37	426	314	84	200	0.39	0.51
F 13-3	- 5435 FT	0.35	0.96	1.09	0.27	416	309	76	272	0.47	0.33
F 13-3	5440 - 5445.7 FT	0.61	1.15	2.09	0.99	423	345	163	190	0.35	0.45
F 13-3	5450 - 5455 FT	0.91	0.53	1.91	0.61	438	211	67	59	0.22	0.72

Client ID	Depth	TOC Wt. %	S1 mg/g	S2 mg/g	S3 mg/g	Tmax	HI	OI	S1/ TOC	PI	Ro
SBF 25-5	- 5312.5 FT	1.51	0.62	5.47	0.72	432	362	48	41	0.1	0.62
SBF 25-5	- 5312.5 FT	1.4	0.03	2.45	0.79	438	175	56	2	0.01	0.72
SBF 25-5	- 5317.9 FT	1.89	0.64	7.27	0.73	432	385	39	34	0.08	0.62
SBF 25-5	- 5317.9 FT	1.71	0.05	5.3	0.7	435	310	41	3	0.01	0.67
SBF 25-5	- 5321.4 FT	1.68	0.68	6.45	0.68	433	384	40	40	0.1	0.63
SBF 25-5	- 5321.4 FT	1.57	0.03	3.2	0.93	438	204	59	2	0.01	0.72
SBF 25-5	- 5323 FT	1.88	0.76	7.63	1.01	432	406	54	40	0.09	0.62
SBF 25-5	- 5323 FT	1.69	0.05	4.99	0.67	433	295	40	3	0.01	0.63
SBF 25-5	- 5325.9 FT	1.67	0.62	4.16	0.7	437	249	42	37	0.13	0.71
SBF 25-5	- 5334.5 FT	1.86	0.59	4.32	0.69	435	232	37	32	0.12	0.67
SBF 25-5	- 5339 FT	1.45	0.68	4.17	0.52	433	288	36	47	0.14	0.63
SBF 25-5	- 5339 FT	1.36	0.03	1.85	0.8	439	136	59	2	0.02	0.74
SBF 25-5	- 5353 FT	2.61	0.79	7.6	0.64	431	291	25	30	0.09	0.60
SBF 25-5	- 5353 FT	2.51	0.06	8.68	0.59	431	346	24	2	0.01	0.60
SBF 25-5	- 5362.4 FT	1.66	0.48	4.75	0.51	435	286	31	29	0.09	0.67
SBF 25-5	- 5362.4 FT	1.51	0.04	1.81	0.93	439	120	62	3	0.02	0.74
SBF 25-5	- 5371 FT	2.28	0.94	10.73	0.75	432	471	33	41	0.08	0.62
SBF 25-5	- 5371 FT	2.06	0.06	7.11	1.17	433	345	57	3	0.01	0.63
SBF 25-5	- 5446.8 FT	2.3	1.24	9.44	0.72	432	410	31	54	0.12	0.62
SBF 25-5	- 5446.8 FT	2.05	0.07	7.49	1.52	433	365	74	3	0.01	0.63
SBF 25-5	- 5450.5 FT	3.06	1.44	14.59	0.63	433	477	21	47	0.09	0.63
SBF 25-5	- 5450.5 FT	2.72	0.07	11.81	0.68	434	434	25	3	0.01	0.65
SBF 25-5	- 5452.9 FT	2.69	1.72	11.03	0.65	433	410	24	64	0.13	0.63
SBF 25-5	- 5452.9 FT	2.34	0.08	9.06	0.73	434	387	31	3	0.01	0.65
SBF 25-5	- 5461 FT	0.89	2.34	3.69	0.43	430	415	48	263	0.39	0.58
SBF 25-5	- 5525.5 FT	0.87	1.54	2.54	0.41	426	292	47	177	0.38	0.51
SBF 25-5	5535.5 - 5545.5 FT	0.86	1.3	1.82	0.46	432	213	54	152	0.42	0.62
SBF 25-5	5553.5 - 5565.5 FT	0.79	1.41	2.67	0.41	429	337	52	178	0.35	0.56

Client ID	Depth	TOC Wt. %	S1 mg/g	S2 mg/g	S3 mg/g	Tmax	HI	OI	S1/ TOC	PI	Ro
S2	- 5277 FT	1.56	0.75	2.3	0.45	451	147	29	48	0.25	0.96
S2	- 5282.5 FT	1.65	0.69	2.47	0.57	447	150	35	42	0.22	0.89
S2	- 5288.2 FT	1.57	0.7	2.49	0.56	451	159	36	45	0.22	0.96
S2	- 5291.9 FT	2.63	1.13	3.67	0.67	450	140	25	43	0.24	0.94
S2	- 5297.3 FT	2.3	1.02	2.88	1.03	442	125	45	44	0.26	0.80
S2	- 5303 FT	2.65	1.68	4.81	1.47	448	182	55	63	0.26	0.90
S2	- 5308.3 FT	2.68	1.64	4.84	0.79	447	181	29	61	0.25	0.89
S2	- 5313.5 FT	2.31	1.38	3.88	0.69	450	168	30	60	0.26	0.94
S2	- 5318.9 FT	2.28	1.36	4.09	1.45	450	179	64	60	0.25	0.94
S2	- 5324.5 FT	2.22	1.44	4.24	1.75	450	191	79	65	0.25	0.94
S2	- 5329.9 FT	2.67	1.61	4.56	0.97	448	171	36	60	0.26	0.90
S2	- 5335.5 FT	2.49	1.39	4.56	0.69	448	183	28	56	0.23	0.90
S2	- 5342.5 FT	1.93	1.09	3.38	0.79	447	175	41	56	0.24	0.89
S2	- 5347.2 FT	1.89	1.2	3.17	0.88	444	168	47	63	0.27	0.83
S2	- 5352.2 FT	2.48	1.3	4.12	0.85	447	166	34	52	0.24	0.89
S2	- 5355.9 FT	2.14	1.34	3.8	0.74	448	178	35	63	0.26	0.90
S2	- 5357.5 FT	2.03	1.17	2.9	0.77	446	143	38	58	0.29	0.87
S2	- 5362.5 FT	2.15	1.22	3.32	0.88	444	154	41	57	0.27	0.83
S2	- 5367 FT	2.13	1.35	4.16	0.96	445	195	45	63	0.25	0.85
S2	- 5372.1 FT	1.91	1.2	3.38	0.74	447	177	39	63	0.26	0.89
S2	- 5378.5 FT	1.92	1.13	3.44	0.78	445	179	41	59	0.25	0.85
S2	- 5383.5 FT	1.68	1	2.65	0.66	446	158	39	60	0.27	0.87
S2	- 5388.5 FT	1.57	0.75	2.09	0.74	450	133	47	48	0.26	0.94
S2	- 5393.5 FT	1.55	0.94	2.57	0.6	450	166	39	61	0.27	0.94
S2	- 5398.5 FT	1.42	0.77	1.93	0.72	445	136	51	54	0.29	0.85
S2	- 5402.5 FT	1.43	0.8	2.22	0.66	447	155	46	56	0.26	0.89
S2	- 5524.5 FT	2.26	1.23	3.25	1.01	443	144	45	54	0.27	0.81
S2	- 5529.5 FT	2.5	1.33	4.21	0.62	450	168	25	53	0.24	0.94
S2	- 5535.3 FT	2.13	1.37	3.69	0.57	448	173	27	64	0.27	0.90
S2	- 5540.3 FT	2.12	1.46	3.57	0.79	445	168	37	69	0.29	0.85
S2	- 5545.4 FT	1.43	0.89	2.25	0.55	444	157	38	62	0.28	0.83
S2	- 5550.8 FT	2.26	1.33	3.71	0.5	449	164	22	59	0.26	0.92
S2	- 5557.4 FT	1.97	1.13	3.02	0.68	447	153	35	57	0.27	0.89
S2	- 5562.2 FT	1.68	1.03	2.9	0.47	448	173	28	61	0.26	0.90
S2	- 5563.5 FT	2	1.19	3.66	0.66	448	183	33	60	0.25	0.90
S2	- 5567.5 FT	1.32	0.68	1.77	0.34	448	134	26	52	0.28	0.90
S2	- 5571.9 FT	2.53	1.02	3.45	0.53	453	136	21	40	0.23	0.99
S2	- 5573.5 FT	2.21	1.08	3.09	1.04	452	140	47	49	0.26	0.98
S2	- 5580.1 FT	1.9	1.16	3.75	0.57	449	197	30	61	0.24	0.92
S2	- 6585.7 FT	1.53	0.94	2.7	0.49	449	176	32	61	0.26	0.92

EnCana Oil & Gas (USA), Inc
 XRD Results for Sample, "NA3E, 6536.7 ft"
 Mean Depth Given as Sample ID

May 2, 2011
 Lab no. 211214

Mineral Name	Chemical Formula	Approx. Wt %
Quartz	SiO_2	33
Mica/illite	$(\text{K}, \text{Na}, \text{Ca})(\text{Al}, \text{Mg}, \text{Fe})_2(\text{Si}, \text{Al})_4\text{O}_{10}(\text{OH}, \text{F})_2$	22
Kaolinite	$\text{Al}_2\text{Si}_2\text{O}_5(\text{OH})_4$	7
Chlorite	$(\text{Mg}, \text{Fe}, \text{Al})_6(\text{Si}, \text{Al})_4\text{O}_{10}(\text{OH})$	—
Smectite	$(\text{Ca}, \text{Na})_x(\text{Al}, \text{Mg}, \text{Fe})_4(\text{Si}, \text{Al})_8\text{O}_{20}(\text{OH}, \text{F})_4 \cdot n\text{H}_2\text{O}$	—
Plagioclase feldspar	$(\text{Na}, \text{Ca})\text{Al}(\text{Si}, \text{Al})_3\text{O}_8$	6
K-feldspar	KAlSi_3O_8	—
Calcite	CaCO_3	20 [®]
Dolomite	$\text{Ca}(\text{Mg}, \text{Fe})(\text{CO}_3)_2$	9
Pyrite	FeS_2	<2
"Unidentified"	?	<5

Initial _____
 Date _____

Analysis performed by The Mineral Lab, Inc

Mineral Name	Chemical Formula	Approx. Wt %					
		6510.2	6611.5	6770.0	6926.0	7008.5	7208.5
Quartz	SiO ₂	34	30	21	28	34	27
Mica/illite	(K,Na,Ca)(Al,Mg,Fe) ₂ (Si,Al) ₄ O ₁₀ (OH,F) ₂	26	24	15	18	20	22
Kaolinite	Al ₂ Si ₂ O ₅ (OH) ₄	9	<5	<5	<5	—	7
Chlorite	(Mg,Fe,Al) ₆ (Si,Al) ₄ O ₁₀ (OH)	<3?	—	—	—	<3?	18
Smectite	(Ca,Na) _x (Al,Mg,Fe) ₄ (Si,Al) ₈ O ₂₀ (OH,F) ₄ •nH ₂ O	—	—	—	—	—	—
Plagioclase feldspar	(Na,Ca)Al(Si,Al) ₃ O ₈	6	5	<5	7	6	6
K-feldspar	KAlSi ₃ O ₈	—	—	—	—	—	—
Calcite	CaCO ₃	10	26	52	32	25	16
Dolomite	Ca(Mg,Fe)(CO ₃) ₂	10	8	6	9	9	<3
Pyrite	FeS ₂	<1	<2	<2	<2	<2	<3
"Unidentified"	?	<5	<5	<5	<5	<5	<5

Initial _____

Date _____

Analysis performed by The Mineral Lab, Inc

Mineral Name	Chemical Formula	Approx. Wt %				
		7232.0	7254.5	7299.7	7320.5	7344.9
Quartz	SiO ₂	27	28	28	32	40
Mica/illite	(K,Na,Ca)(Al,Mg,Fe) ₂ (Si,Al) ₄ O ₁₀ (OH,F) ₂	22	27	29	32	35
Kaolinite	Al ₂ Si ₂ O ₅ (OH) ₄	14	18	18	15	—
Chlorite	(Mg,Fe,Al) ₆ (Si,Al) ₄ O ₁₀ (OH)	15	<5	10	5	10
Smectite	(Ca,Na) _x (Al,Mg,Fe) ₄ (Si,Al) ₈ O ₂₀ (OH,F) ₄ •nH ₂ O	—	—	—	—	—
Plagioclase feldspar	(Na,Ca)Al(Si,Al) ₃ O ₈	5	6	7	8	11
K-feldspar	KAlSi ₃ O ₈	—	—	—	—	—
Calcite	CaCO ₃	12	8	—	—	—
Dolomite	Ca(Mg,Fe)(CO ₃) ₂	<3	<5	<5	<5	—
Pyrite	FeS ₂	<2	<2	<2	<2	<1
"Unidentified"	?	<5	<5	<5	<5	<5

Initial _____

Date _____

Analysis performed by The Mineral Lab, Inc

Mineral Name	Chemical Formula	Approx. Wt %	
		5105.0	5285.0
Quartz	SiO_2	30	35
Mica/illite	$(\text{K}, \text{Na}, \text{Ca})(\text{Al}, \text{Mg}, \text{Fe})_2(\text{Si}, \text{Al})_4\text{O}_{10}(\text{OH}, \text{F})_2$	23	20
Kaolinite	$\text{Al}_2\text{Si}_2\text{O}_5(\text{OH})_4$	<5	12
Chlorite	$(\text{Mg}, \text{Fe}, \text{Al})_6(\text{Si}, \text{Al})_4\text{O}_{10}(\text{OH})$	<5?	—
Smectite	$(\text{Ca}, \text{Na})_x(\text{Al}, \text{Mg}, \text{Fe})_4(\text{Si}, \text{Al})_8\text{O}_{20}(\text{OH}, \text{F})_4 \cdot n\text{H}_2\text{O}$	—	—
Plagioclase feldspar	$(\text{Na}, \text{Ca})\text{Al}(\text{Si}, \text{Al})_3\text{O}_8$	6	8
K-feldspar	KAlSi_3O_8	—	<5?
Calcite	CaCO_3	22	11
Dolomite	$\text{Ca}(\text{Mg}, \text{Fe})(\text{CO}_3)_2$	9	6
Pyrite	FeS_2	<2	<2
"Unidentified"	?	<5	<5

Initial _____

Date _____

Analysis performed by The Mineral Lab, Inc

Mineral Name	Chemical Formula	Approx. Wt %		
		6029.5	6131.5	6282.5
Quartz	SiO_2	32	27	36
Mica/illite	$(\text{K}, \text{Na}, \text{Ca})(\text{Al}, \text{Mg}, \text{Fe})_2(\text{Si}, \text{Al})_4\text{O}_{10}(\text{OH}, \text{F})_2$	25	9	20
Kaolinite	$\text{Al}_2\text{Si}_2\text{O}_5(\text{OH})_4$	<5	<5?	<3?
Chlorite	$(\text{Mg}, \text{Fe}, \text{Al})_6(\text{Si}, \text{Al})_4\text{O}_{10}(\text{OH})$	—	—	<3?
Smectite	$(\text{Ca}, \text{Na})_x(\text{Al}, \text{Mg}, \text{Fe})_4(\text{Si}, \text{Al})_8\text{O}_{20}(\text{OH}, \text{F})_4 \cdot n\text{H}_2\text{O}$	—	—	—
Plagioclase feldspar	$(\text{Na}, \text{Ca})\text{Al}(\text{Si}, \text{Al})_3\text{O}_8$	6	5	6
K-feldspar	KAlSi_3O_8	—	—	<3?
Calcite	CaCO_3	21	42	20
Dolomite	$\text{Ca}(\text{Mg}, \text{Fe})(\text{CO}_3)_2$	8	11	9
Pyrite	FeS_2	<2	<1	<2
"Unidentified"	?	<5	<5	<5

Initial _____

Date _____

Analysis performed by The Mineral Lab, Inc

Mineral Name	Chemical Formula	Approx. Wt %		
		5423.5	5442.5	5460.5
Quartz	SiO ₂	32	43	47
Mica/illite	(K,Na,Ca)(Al,Mg,Fe) ₂ (Si,Al) ₄ O ₁₀ (OH,F) ₂	15	5	7
Kaolinite	Al ₂ Si ₂ O ₅ (OH) ₄	—	12	6
Chlorite	(Mg,Fe,Al) ₆ (Si,Al) ₄ O ₁₀ (OH)	—	—	—
Smectite	(Ca,Na) _x (Al,Mg,Fe) ₄ (Si,Al) ₈ O ₂₀ (OH,F) ₄ •nH ₂ O	—	—	—
Plagioclase feldspar	(Na,Ca)Al(Si,Al) ₃ O ₈	10	5	10
K-feldspar	KAlSi ₃ O ₈	<3	<5	<5
Calcite	CaCO ₃	30	17	11
Dolomite	Ca(Mg,Fe)(CO ₃) ₂	9	12	14
Pyrite	FeS ₂	<2	<1	<2
"Unidentified"	?	<5	<5	<5

Initial _____

Date _____

Analysis performed by The Mineral Lab, Inc

Mineral Name	Chemical Formula	Approx. Wt %	
		5315.0	5525.0
Quartz	SiO_2	30	26
Mica/illite	$(\text{K}, \text{Na}, \text{Ca})(\text{Al}, \text{Mg}, \text{Fe})_2(\text{Si}, \text{Al})_4\text{O}_{10}(\text{OH}, \text{F})_2$	19	20
Kaolinite	$\text{Al}_2\text{Si}_2\text{O}_5(\text{OH})_4$	9	—
Chlorite	$(\text{Mg}, \text{Fe}, \text{Al})_6(\text{Si}, \text{Al})_4\text{O}_{10}(\text{OH})$	—	—
Smectite	$(\text{Ca}, \text{Na})_x(\text{Al}, \text{Mg}, \text{Fe})_4(\text{Si}, \text{Al})_8\text{O}_{20}(\text{OH}, \text{F})_4 \cdot n\text{H}_2\text{O}$	—	—
Plagioclase feldspar	$(\text{Na}, \text{Ca})\text{Al}(\text{Si}, \text{Al})_3\text{O}_8$	6	5
K-feldspar	KAlSi_3O_8	<3?	—
Calcite	CaCO_3	22	39
Dolomite	$\text{Ca}(\text{Mg}, \text{Fe})(\text{CO}_3)_2$	9	8
Pyrite	FeS_2	<2	<1
"Unidentified"	?	<5	<5

Initial _____

Date _____

Analysis performed by The Mineral Lab, Inc

EnCana Oil & Gas (USA), Inc
XRD Results for "WJ 2" Samples
Mean Depth Given as Sample ID

May 2, 2011
Lab no. 211214

Mineral Name	Chemical Formula	Approx. Wt %			
		4653.0	4674.0	4751.0	4800.0
Quartz	SiO ₂	42	30	58	48
Mica/illite	(K,Na,Ca)(Al,Mg,Fe) ₂ (Si,Al) ₄ O ₁₀ (OH,F) ₂	10	23	<5	—
Kaolinite	Al ₂ Si ₂ O ₅ (OH) ₄	20	13	5	—
Chlorite	(Mg,Fe,Al) ₆ (Si,Al) ₄ O ₁₀ (OH)	—	—	—	—
Smectite	(Ca,Na) _x (Al,Mg,Fe) ₄ (Si,Al) ₈ O ₂₀ (OH,F) ₄ •nH ₂ O	—	—	—	—
Plagioclase feldspar	(Na,Ca)Al(Si,Al) ₃ O ₈	7	7	7	5
K-feldspar	KAlSi ₃ O ₈	5	<5	14	7
Calcite	CaCO ₃	<5	10	6	28
Dolomite	Ca(Mg,Fe)(CO ₃) ₂	12	13	6	9
Pyrite	FeS ₂	<2	<2	<1	—
"Unidentified"	?	<5	<5	<5	<5

Initial_____

Date_____

Analysis performed by The Mineral Lab, Inc

EnCana Oil & Gas (USA), Inc
XRD Results for "FC 3" Samples
Mean Depth Given as Sample ID

May 2, 2011
Lab no. 211214

Mineral Name	Chemical Formula	Approx. Wt %		
		5804.5	5845.0	5876.0
Quartz	SiO ₂	53	28	70
Mica/illite	(K,Na,Ca)(Al,Mg,Fe) ₂ (Si,Al) ₄ O ₁₀ (OH,F) ₂	10	33	9
Kaolinite	Al ₂ Si ₂ O ₅ (OH) ₄	6	7	<5?
Chlorite	(Mg,Fe,Al) ₆ (Si,Al) ₄ O ₁₀ (OH)	—	—	—
Smectite	(Ca,Na) _x (Al,Mg,Fe) ₄ (Si,Al) ₈ O ₂₀ (OH,F) ₄ •nH ₂ O	—	—	—
Plagioclase feldspar	(Na,Ca)Al(Si,Al) ₃ O ₈	6	<5	8
K-feldspar	KAlSi ₃ O ₈	8	—	—
Calcite	CaCO ₃	16	20	10
Dolomite	Ca(Mg,Fe)(CO ₃) ₂	—	8	—
Pyrite	FeS ₂	<2	<1	<1
"Unidentified"	?	<5	<5	<5

Initial_____

Date_____

Analysis performed by The Mineral Lab, Inc

Mineral Name	Chemical Formula	Approx. Wt %				
		5312.5	5325.9	5328.7	5334.5	5450.5
Quartz	SiO ₂	34	30	35	26	32
Mica/illite	(K,Na,Ca)(Al,Mg,Fe) ₂ (Si,Al) ₄ O ₁₀ (OH,F) ₂	22	29	10	32	30
Kaolinite	Al ₂ Si ₂ O ₅ (OH) ₄	—	7	<5	8	<5
Chlorite	(Mg,Fe,Al) ₆ (Si,Al) ₄ O ₁₀ (OH)	—	<5	—	—	—
Smectite	(Ca,Na) _x (Al,Mg,Fe) ₄ (Si,Al) ₈ O ₂₀ (OH,F) ₄ •nH ₂ O	<5?	—	—	—	—
Plagioclase feldspar	(Na,Ca)Al(Si,Al) ₃ O ₈	9	8	<5	5	7
K-feldspar	KAlSi ₃ O ₈	<3	<5	<3?	—	—
Calcite	CaCO ₃	18	6	19	<5	14
Dolomite	Ca(Mg,Fe)(CO ₃) ₂	9	8	26*	21	9
Pyrite	FeS ₂	<2	<2	<1	<2	<2
"Unidentified"	?	<5	<5	<5	<5	<5

*Appears to be two phases - a dolomite and a minor amount of a more Fe rich phase, "ankerite or ferroan dolomite"

Initial _____

Date _____

Analysis performed by The Mineral Lab, Inc

Mineral Name	Chemical Formula	Approx. Wt %			
		5461.0	5515.2	5540.5	5559.5
Quartz	SiO ₂	77	50	41	45
Mica/illite	(K,Na,Ca)(Al,Mg,Fe) ₂ (Si,Al) ₄ O ₁₀ (OH,F) ₂	6	7	9	7
Kaolinite	Al ₂ Si ₂ O ₅ (OH) ₄	—	12	8	12
Chlorite	(Mg,Fe,Al) ₆ (Si,Al) ₄ O ₁₀ (OH)	—	—	—	—
Smectite	(Ca,Na) _x (Al,Mg,Fe) ₄ (Si,Al) ₈ O ₂₀ (OH,F) ₄ •nH ₂ O	—	—	—	—
Plagioclase feldspar	(Na,Ca)Al(Si,Al) ₃ O ₈	<5	5	5	7
K-feldspar	KAlSi ₃ O ₈	6	7	5	7
Calcite	CaCO ₃	<5	5	14	<5
Dolomite	Ca(Mg,Fe)(CO ₃) ₂	—	11	13	14
Pyrite	FeS ₂	<1	<1	<2	<2
"Unidentified"	?	<5	<5	<5	<5

Initial _____
Date _____

Analysis performed by The Mineral Lab, Inc

Mineral Name	Chemical Formula	Approx. Wt %		
		5416.5	5419.5	5430.7
Quartz	SiO_2	34	33	73
Mica/illite	$(\text{K,Na,Ca})(\text{Al,Mg,Fe})_2(\text{Si,Al})_4\text{O}_{10}(\text{OH,F})_2$	23	24	—
Kaolinite	$\text{Al}_2\text{Si}_2\text{O}_5(\text{OH})_4$	<5	7	—
Chlorite	$(\text{Mg,Fe,Al})_6(\text{Si,Al})_4\text{O}_{10}(\text{OH})$	—	—	—
Smectite	$(\text{Ca,Na})_x(\text{Al,Mg,Fe})_4(\text{Si,Al})_8\text{O}_{20}(\text{OH,F})_4 \cdot n\text{H}_2\text{O}$	<5?	—	—
Plagioclase feldspar	$(\text{Na,Ca})\text{Al}(\text{Si,Al})_3\text{O}_8$	6	6	<3
K-feldspar	KAlSi_3O_8	<5	<5	6
Calcite	CaCO_3	16	5	17
Dolomite	$\text{Ca}(\text{Mg,Fe})(\text{CO}_3)_2$	7	18	—
Pyrite	FeS_2	<2	<2	—
"Unidentified"	?	<5	<5	<5

Initial _____
Date _____

Analysis performed by The Mineral Lab, Inc

Mineral Name	Chemical Formula	Approx. Wt %		
		5435.0	5442.9	5452.5
Quartz	SiO_2	76	43	46
Mica/illite	$(\text{K,Na,Ca})(\text{Al,Mg,Fe})_2(\text{Si,Al})_4\text{O}_{10}(\text{OH,F})_2$	<5	14	14
Kaolinite	$\text{Al}_2\text{Si}_2\text{O}_5(\text{OH})_4$	—	15	6
Chlorite	$(\text{Mg,Fe,Al})_6(\text{Si,Al})_4\text{O}_{10}(\text{OH})$	—	—	—
Smectite	$(\text{Ca,Na})_x(\text{Al,Mg,Fe})_4(\text{Si,Al})_8\text{O}_{20}(\text{OH,F})_4 \cdot n\text{H}_2\text{O}$	—	—	—
Plagioclase feldspar	$(\text{Na,Ca})\text{Al}(\text{Si,Al})_3\text{O}_8$	<5	7	5
K-feldspar	KAlSi_3O_8	8	8	6
Calcite	CaCO_3	7	7	7
Dolomite	$\text{Ca}(\text{Mg,Fe})(\text{CO}_3)_2$	—	<5	12
Pyrite	FeS_2	—	<1	<2
"Unidentified"	?	<5	<5	<5

Initial _____
Date _____

Analysis performed by The Mineral Lab, Inc

Mineral Name	Chemical Formula	Approx. Wt %				
		5277.0	5297.3	5303.0	5352.2	5355.9
Quartz	SiO ₂	45	13	26	28	25
Mica/illite	(K,Na,Ca)(Al,Mg,Fe) ₂ (Si,Al) ₄ O ₁₀ (OH,F) ₂	16	5	21	23	20
Kaolinite	Al ₂ Si ₂ O ₅ (OH) ₄	5	—	<5	<5	<3?
Chlorite	(Mg,Fe,Al) ₆ (Si,Al) ₄ O ₁₀ (OH)	—	—	—	—	<3?
Smectite	(Ca,Na) _x (Al,Mg,Fe) ₄ (Si,Al) ₈ O ₂₀ (OH,F) ₄ •nH ₂ O	—	—	—	—	—
Plagioclase feldspar	(Na,Ca)Al(Si,Al) ₃ O ₈	5	<5	5	5	5
K-feldspar	KAlSi ₃ O ₈	—	—	—	—	—
Calcite	CaCO ₃	16	73	36	28	37
Dolomite	Ca(Mg,Fe)(CO ₃) ₂	10	<5	<5	8	7
Pyrite	FeS ₂	<1	<1	<2	<2	<2
"Unidentified"	?	<5	<5	<5	<5	<5

Initial _____
Date _____

Analysis performed by The Mineral Lab, Inc

Mineral Name	Chemical Formula	Approx. Wt %			
		5402.5	5524.5	5563.5	5573.5
Quartz	SiO_2	30	32	35	46
Mica/illite	$(\text{K,Na,Ca})(\text{Al,Mg,Fe})_2(\text{Si,Al})_4\text{O}_{10}(\text{OH,F})_2$	23	19	24	13
Kaolinite	$\text{Al}_2\text{Si}_2\text{O}_5(\text{OH})_4$	—	—	—	6
Chlorite	$(\text{Mg,Fe,Al})_6(\text{Si,Al})_4\text{O}_{10}(\text{OH})$	<3	—	—	—
Smectite	$(\text{Ca,Na})_x(\text{Al,Mg,Fe})_4(\text{Si,Al})_8\text{O}_{20}(\text{OH,F})_4 \cdot n\text{H}_2\text{O}$	—	—	—	—
Plagioclase feldspar	$(\text{Na,Ca})\text{Al}(\text{Si,Al})_3\text{O}_8$	5	5	7	9
K-feldspar	KAlSi_3O_8	—	—	—	—
Calcite	CaCO_3	28	33	22	11
Dolomite	$\text{Ca}(\text{Mg,Fe})(\text{CO}_3)_2$	8	7	8	10
Pyrite	FeS_2	<1	<2	<2	<2
"Unidentified"	?	<5	<5	<5	<5

Initial _____
Date _____

Analysis performed by The Mineral Lab, Inc

References

- Broadhead, R.F., 2013, “The Mancos Shale and “Gallup” zones in the San Juan Basin: geologic framework, historical production, future potential”, presented at the San Juan Basin Energy Conference, Farmington, New Mexico, March 18-19, 2013.
- Broadhead, R.F., 2015, The Upper Mancos Shale in the San Juan Basin: Three plays, conventional and unconventional: American Association of Petroleum Geologists, Search and Discovery, Document No. 10791, p. 39.
- Budd, H., 1957, Facies development of the Gallup formation, *in* Geology of Southwestern San Juan Basin, Second field conference: Four Corners Geological Society, pp. 121-127.
- Craig, S.D., 1971, Geologic framework of the San Juan structural basin of New Mexico, Colorado, Arizona, and Utah with emphasis on Triassic through Tertiary rocks, U.S. Geological Survey, Professional Paper, v. 1420, pp. 4-32.
- Dane, C.H., 1960, The boundary between rocks of Carlisle and Niobrara age in San Juan Basin, New Mexico and Colorado: American Journal of Science, v. 258A, pp. 46-56.
- Dow, W.G., 1977, Kerogen studies and geological interpretations: Journal of Geochemical Exploration, v. 7, pp. 79-99, doi: 10.1016/0375-6742(77)(90078-4.
- Fassett, J.E., Jentgen, R.W., 1978, Blanco Tocito, South, *in* Fassett, J.E. ed., Oil and Gas Fields of the Four Corners area: Four Corners Geological Society, pp. 464-471.
- Fassett, J.E., 2010, Oil and gas resources of the San Juan Basin, New Mexico and Colorado, *in* Fassett, J.E., Zeigler, J.E., Lueth, K.E., Virgil, W. [eds.], New Mexico Geological Society 61st Annual Fall Field Conference Guidebook, 246 p.
- Gao, Z., Hu, Q., 2012, Using spontaneous water imbibition to measure the effective permeability of building materials, Special Topics & Reviews in Porous Media: An International

- Journal, v. 3, pp. 209-213.
- Gao, Z., and Hu, Q., 2013, Estimating permeability using median pore-throat radius obtained from mercury intrusion porosimetry. *Journal of Geophysics and Engineering*, v. 10, p. 025014.
- Gharrabi, M.B., Velde, B., and Sagon, J.P., 1998, The transformation of illite to muscovite in pelitic rocks: Constraints from x-ray diffraction, *clay and clay minerals*, v. 46, pp. 79-88.
- Guodong, J., Perez, H.G., Al Dhamen, A.A., Ali, S.S., Nair, A., and Agrawal, G., 2015, Permeability measurement of organic-rich shale-comparison of various insteady-state methods, SPE-175105-MS, presented at the SPE Annual Technical Conference and Exhibition, Houston, TX, 28-30 September 2015.
- Emmendorfer, A.P., 1989, Structural influences in Gavilian Mancos Oil Pool: Fractures, dolomitization, mineralization: *American Association of Petroleum Geologists Bulletin*, v. 73, 1154 p.
- Horton, B., 2012, Variability of the Mancos Shale: Developing preliminary depositional and sequence stratigraphy models of a developing shale gas play, master's thesis, University of Utah, Salt Lake City, Utah, 320 p.
- Hu, Q.H., Ewing, R.P., and Rowe, H.D., 2015, Low nanopore connectivity limits gas production in Barnett formation. *Journal of Geophysical Research: Solid Earth*, v. 120, pp. 8073-8087.
- Hu, Q.H., Ewing, R.P., 2014, Integrated experimental and modeling approaches to studying the fracture-matrix interaction in gas recover from Barnett Shale, 91 p.
- Hu, Q.H., Persoff, P., and Wang, J.S.Y., 2001, Laboratory measurement of water imbibition into low-permeability welded tuff: *Journal of Hydrology*, v. 242, pp. 64-78.

- Huffman, C.A., 1987, Petroleum geology and hydrocarbon plays of the San Juan Basin petroleum system, U.S. Geological Survey Open-File Report No. 87-450B, pp. 38-46.
- Hughes, J.D., 2014, Drilling Deeper: A reality check on U.S. government forecasts for a lasting oil and shale gas boom. Post Carbon Institute.
- Jarvie, D., Claxton, B., Henk, F., Breyer, J., 2001, Oil and shale gas from the Barnett Shale, Fort Worth Basin, Texas: AAPG Annual Meeting Program, v. 10, p. A100.
- Jarvie, D. M., 2012, Shale resource systems for oil and gas: Part 2—Shale-oil resource systems, *in* J. A. Breyer, ed., Shale reservoirs—Giant resources for the 21st century: AAPG Memoir 97, pp. 89–119.
- Just, B., Lloyd, R., Anderson, R., 2013, U.S. Department of the Interior, Indian Affairs, Division of Energy and Mineral Development: Emerging Oil and Gas Development in Northwestern New Mexico, Horizontal Gallup/Mancos Play.
<https://www.bia.gov/cs/groups/xieed/documents/document/idc1-026005.pdf>. (accessed on October 30, 2017).
- Kao, C.S., and Hunt, J.R., 1996, Prediction of wetting front movement during one-dimensional infiltration into soils: Water Resources Research, v. 32, pp. 55-64.
- Katz, A.J., and Thompson, A.H., 1986, A quantitative prediction of permeability in porous rocks, American Physical Society, pp. 8179-8181.
- Kiepsch, S., and Pelster, R., 2016, Interplay of vapor adsorption and liquid imbibition in nanoporous Vycor glass, Phys. Rev. E, 043238.
- Kuila, U., Prasad, M., Derkowski, A., McCarty, D.K., 2012, Compositional controls on mudrock pore-size distribution: An example from Niobrara Formation: SPE Annual Technical Conference and Exhibition, doi: 10.2118/160141-ms.

- Löhr, S.C., Baruch, E.T., Hall, P.A., Kennedy, M.J., 2015, Is organic pore development in gas shales influenced by the primary porosity and structure of thermally immature organic matter? *Organic Geochemistry*, v. 87, pp. 119-132.
- Loucks, R.G., Reed, R.M., Ruppel, S.C., and Hammes, U., 2012, Spectrum of pore types and networks in mudrocks and a descriptive classification for matrix-related mudrock pores, *AAPG Bulletin*, v. 96, No. 6, pp. 1071-1098.
- London, W.W., 1972, Dolomite in flexure-fractured petroleum reservoirs in New Mexico and Colorado, *AAPG Bulletin*, v. 56, pp. 815-821.
- Longman, M.W., Luneau, B.A., and Landon, S.M., 1998, Nature and distribution of Niobrara lithologies in the Cretaceous Western Interior Seaway of the Rocky Mountain Region, *The Mountain Geologist*, v. 35, No. 4, pp. 137-170.
- Matheny, M.L., Matheny, P.M., 1983, Cha Cha Gallup (Oil), *in*: Oil and gas fields of the Four Corners area, Fassett, J. E.; Thomaidis, N. D.; Matheny, M. L., *ed(s)*, Four Corners Geological Society, v. III, pp. 256-259.
- Molenaar, C.M., 1974, Correlation of the Gallup Sandstone and associated formations, Upper Cretaceous, eastern San Juan and Acoma basins, New Mexico, *in* Ghost Ranch, central-northern New Mexico: New Mexico Geological Society Guidebook to 25th Field Conference, pp. 251-258.
- Molenaar, C.M., 1977, Stratigraphy and depositional history of Upper Cretaceous rocks of the San Juan Basin area, New Mexico and Colorado, with a note of economic resources: New Mexico Geological Society, Guidebook, 28th Field Conference, pp. 159-166.

- Morsey, S., Gomma, A., and Sheng, J.J., 2014, Improvement of Mancos Shale oil recovery by wettability alteration and mineral dissolution, SPE-169033-MS presented at the SPE Improved Oil Recovery Symposium, Tulsa, Oklahoma, 12-16 April 2014.
- NGI (Natural Gas Intelligence), 2017, Shale Daily: Information of the San Juan Basin.
<http://www.naturalgasintel.com/sanjuaninfo>.
- Philip, J.R., 1957, The theory of infiltration: 4. Sorptivity and algebraic infiltration equations: Soil Science, v. 84, pp.257-264.
- Ridgley, J.L., Condon, S.M., and Hatch, J.R., 2013, Geology and oil and gas assessment of the Mancos-Menefee composite total petroleum system, San Juan Basin, New Mexico and Colorado, chap. 4 of U.S. Geological Survey San Juan Basin Assessment Team, Total petroleum systems and geologic assessment of undiscovered oil and gas resources in the San Juan Basin Province, exclusive of Paleozoic rocks, New Mexico and Colorado: U.S. Geological Survey Digital Data Series 69–F, pp. 1–97.
- Robinson-Avila, K., 2013, Albuquerque Journal: Prospects good for New Mexico Oil, Gas Boom. <https://www.abqjournal.com/181599/prospects-good-for-nm-oil-gas-boom.html>.
- Rouquerol, J., Rouquerol, F., and Sing, K.S.W., 1998, Adsorption by powders and porous solids: Principles, Methodology, and Applications, Academic Press, 1999.
- Sabins, F.F., 1983, Bisti Lower Gallup (Oil), *in*: Oil and gas fields of the Four Corners area, Fassett, J. E.; Thomaidis, N. D.; Matheny, M. L., *ed(s)*, Four Corners Geological Society, v. III, pp. 213-215.
- Schieber, J., 2010, Common themes in the formation and preservation of porosity in shales and mudstones: Illustrated with examples across the Phanerozoic: Society of Petroleum

- Engineers Unconventional Gas Conference, Pittsburgh, Pennsylvania, February 23-25, 2010, SPE Paper 132370, p. 12.
- Silver, C., 1957, Relation of coastal and submarine topography to Cretaceous stratigraphy, *in* Geology of Southwestern San Juan Basin, Second field conference: Four Corners Geological Society, pp. 128-137.
- Sing, K.S.W., 1985, Reporting physisorption data for gas/solid systems with special reference to the determination of surface area and porosity: *Pure and Applied Chemistry*, 57 (4): 603-619, doi: 10.1351/pac198557040603.
- Sperandio, R. J., 1983, Armenta Gallup (oil), *in*: Oil and gas fields of the Four Corners area, Fassett, J. E.; Thomaidis, N. D.; Matheny, M. L., *ed(s)*, Four Corners Geological Society, v. III, pp. 934-935.
- Tokunaga, T.K., and Wan, J., 2001, Surface-zone flow along unsaturated rock fractures: *Water Resources Research*, v. 37, pp. 287-296.
- Villegas, R.R., 2016, Nanopetrophysics of the Niobrara Formation in Berthoud State #3 well, Unpublished master's thesis, The University of Texas at Arlington, College of Earth and Environmental Sciences, Arlington, TX.
- Wang, S., Javadpour, F., and Feng, Q., 2016, Confinement correction to mercury intrusion capillary pressure of shale nanopores, *Scientific Reports*, v. 6, p. 20160.
- Waples, D.W., 1985, Geochemistry in Petroleum Exploration, Chapter 2: Organic Facies, Source Rock Evaluation, International Human Resources Development Corporation, Denver, Colorado, 96 p.

- Washburn, W.E., 1921, Note of a method of determining the distribution of pore sizes in a porous material, Proceedings of the National Academy of Sciences of the United States of America, v. 7, pp. 115-116.
- Webb, P.A., 2001, An introduction to the physical characterization of materials by mercury intrusion porosimetry with emphasis on reduction and presentation of experimental data, Micromeritics Instrument Corp, Norcross, Georgia.
- Yang, R., Guo, X., Yi, J., Fang, Z., Hu, Q., and He, S., 2017, Spontaneous imbibition of three leading shale formations in the Middle Yangtze Platform, South China, Energy & Fuels, v. 31, pp. 6903-6916.

Biographical Information

Richard Kalteyer is from Dallas, TX and graduated from Highland Park High School. He received his Bachelors of Science Degree in Geology from Texas Christian University in 2015. His love and passion for geology led him to pursue a Masters of Science Degree in Petroleum Geology from the University of Texas at Arlington. While completing his degree, he worked at Matador Resources Company as a geology intern. Upon graduation, he plans to continue a career in the oil and gas industry as a geologist.